ISTANBUL TECHNICAL UNIVERSITY ★ GRADUATE SCHOOL OF SCIENCE ENGINEERING AND TECHNOLOGY

HIGH ENERGY MILLING AND SPRAY DRYING CHARACTERISTICS OF MoO_3, Cr_2O_3 AND WO_3 POWDERS

M.Sc. THESIS

Leila HAGHIGHI POUDEH

Department of Metallurgical and Materials Engineering

Ceramics Engineering Programme

JANUARY 2014

HIGH ENERGY MILLING AND SPRAY DRYING CHARACTERISTICS OF MoO_3, Cr_2O_3 AND WO_3 POWDERS

M.Sc. THESIS

Leila HAGHIGHI POUDEH
(506111304)

Department of Metallurgical and Materials Engineering

Ceramics Engineering Programme

Thesis Advisor: Assoc. Prof. Dr. Burak ÖZKAL

JANUARY 2014

MoO₃, Cr₂O₃ VE WO₃ TOZLARININ YÜKSEK ENERJİLİ ÖĞÜTME VE PÜSKÜRTMELİ KURUTMA KARAKTERİSTİKLERİ

YÜKSEK LİSANS TEZİ

Leila HAGHIGHI POUDEH
(506111304)

Metalurji ve Malzeme Mühendisliği Anabilim Dalı

Seramik Mühendisliği Programı

Tez Danışmanı: Doç. Dr. Burak ÖZKAL

OCAK 2014

Leila Haghighi Poudeh, a **M.Sc.** student of ITU **Graduate School of Science, Engineering and Technology** student ID **506111304**, successfully defended the **thesis/dissertation** entitled "**HIGH ENERGY MILLING AND SPRAY DRYING CHARACTERISTICS OF MoO₃, Cr₂O₃ AND WO₃ POWDERS**" which she prepared after fulfilling the requirements specified in the associated legislations, before the jury whose signatures are below.

Thesis Advisor :   **Assoc. Prof. Dr. Burak ÖZKAL**   ....
İstanbul Technical University

Jury Members :   **Prof. Dr. Lütfi ÖVEÇOĞLU**   ....
İstanbul Technical University

Assis. Prof. Dr. Selim YILDIRIM   ....
İstanbul University

Date of Submission : 16 December 2013
Date of Defense : 22 January 2014

To my parents,

FOREWORD

First and foremost, I would like to thank my supervisor Assoc. Prof. Dr. Burak Özkal for his invaluable guidance, encouragement and support during my MSc. I am especially grateful for his tireless assistance on my experiments. I would also very much like to express my sincere gratitude to Prof. Dr. Lütfi Öveçoğlu for his advice throughout my MSc.

I would also like to thank Particulate Materials Laboratory (PML), for providing all the research facilities during my study. Specific thanks to PML group members, Dr. Hasan Gökçe, Hadi Jahangiri, Didem Ovalı, Ceren İmer and Sultan Sönmez for their support and help. I would also like to express my thanks to A. Umut Söyler for helping me with SEM analysis. A special thank goes to Şeyma Duman and Emre Tekoğlu for their continuing help, advice and friendship.

I would like to express my thanks to İstanbul Development Agency (İSTKA), for providing advanced research facilities to my group under the auspices of the İSTKA/2012/BİL/28 project.

I would also like to thank my friends Faraz Shoaee, Sara Rezaei, Saman Hendessi, and Dilek Kırgöz whose understanding and support made hard days much easier.

Last but not least, I owe special thanks to my parents Mahlagha Mesgarzadeh and Bahman Haghighi Poudeh for their infinite love, support and motivation.

December 2013   Leila HAGHIGHI POUDEH

x

TABLE OF CONTENTS

ABBREVIATIONS

BPR   **:** Ball-to-Powder Ratio
MA   **:** Mechanical Alloying
PVA   **:** Polyvinyl Alcohol
PSD   **:** Partice Size Distribution
SEM   **:** Scanning Electron Microscope
XRD   **:** X-Ray Diffraction
HEM   **:** High Energy Milling
SD   **:** Spray Drying

LIST OF TABLES

LIST OF FIGURES

HIGH ENERGY MILLING AND SPRAY DRYING CHARACTERISTICS OF MoO$_3$, Cr$_2$O$_3$ AND WO$_3$

SUMMARY

Nanoparticles are quite attractive due to their unique electronic, optical, thermal and magnetic properties relying on particle dimension and high surface-to-volume ratio. On the nanoscale, materials behave very differently from those in larger scales.

Many physical, chemical and thermal methods were used to produce nanoparticles, which have different sizes and morphologies. One of these methods is high-energy milling. This method has many advantages such as the production of great amount of materials, ease of production and cheap equipment. High-energy milling is more effective than conventional milling due to the achievement of nanosized particles in lesser times.

Spray drying is a granulation process where the slurry, which is generally water or organic based suspension, is transformed to dry powder by spraying into a hot drying medium. This process is a widely used in producing granulated feed material for compaction processes. Spray drying enables the fabrication of composite powders by aggregation of any kind of small particles using an appropriate organic binder. Optimization of the type and amount of binder is a very important parameter, which determines the flowability, bulk density, and compaction behavior of spray-dried granules. All these properties also affect the sintering behavior of the system if the final usage requires bulk material.

Transition metal oxides are a fascinating class of materials due to their wide-ranging electronic, chemical and mechanical properties. The electrochromic, optochromic properties of MoO$_3$ and WO$_3$ make them usable in many applications such as smart windows, optical memories and gas sensors. On the other hand, Cr$_2$O$_3$ is a hard oxide that also exhibits low friction coefficient, high wear and corrosion resistance, and good optical and adiabatic characteristics. These properties allow it to be used as a protective coating in tribological and microelectronic applications.

According to the above concepts, the aim of this study is production, development and characterization investigations of WO$_3$, MoO$_3$, and Cr$_2$O$_3$ powders via high-energy milling and spray drying processes. The characterization methods used in this study were density measurements, particle size distributions, phase characterizations, and macrostructure and microstructure analysis.

MoO$_3$, Cr$_2$O$_3$ VE WO$_3$ TOZLARININ YÜKSEK ENERJİLİ ÖĞÜTME VE PÜSKÜRTMELİ KURUTMA KARAKTERİSTİKLERİ

ÖZET

Son yıllarda nanoteknoloji üzerine çalışmalar hızla artmakta olup farklı yöntem ve yaklaşımlardan hareketle farklı boyut aralıklarında nanopartiküllerinin üretimine yönelik çalışmaların sayısında giderek artış gözlenmektedir. Nanopartikülerin farklı yöntem ve yaklaşımlar kullanılarak gerek yukarıdan-aşağıya ve gerekse aşağıdan yukarıya prensipleriyle farklı boyut aralıklarında, farklı geometrilerde ve farklı kimyasal formlarda üretilebileceği ortaya konmuş olup özellikle boyuta bağlı olarak gösterdikleri çok farklı özellikler nedeniyle bu partiküllein doğrudan ya da katışık olarak kullanımıyla çok farklı alanlarda uygulanabilirliğine yönelik çalışmalar büyük bir hızla devam etmektedir. Nanopartiküllerin özellikle mikron üstü boyutlarda gösterdikleri elektronik, optik ve ısıl özelliklerin mikronaltı ve ultra ince boyutlara gidildikçe değişime uğradığı ve her malzeme kimyası için aynı olmamakla birlikte özellikle 100 nm altında çok farklı davranışlar gösterdiği bilinmektedir.

Nanopartikül üretiminde kullanılan ve yukarıdan-aşağı yaklaşımlarından biri olan yüksek enerjili öğütme, nispeten diğer yöntemlere nazaran fazla miktarda malzeme üretimine olanak sağlayan, nispeten kolay ve ekonomik ekipman seçenekleri ve farklı sistemlere kolay uygulanabilirliği gibi nedenlerle tercih edilen bir metottur.

Yüksek enerjili öğütmede, normal öğütmeye göre daha kısa sürelerde partikül boyutlarında küçülme sağlamakta ve nano boyutlara daha kısa proses sürelerinde inilmesine olanak tanımaktadır. Bununla birlikte mekanik kuvvetler etkisiyle gerçekleşen bir proses olması nedeniyle öğütücü ortam ile öğütülecek malzeme karakteristikleri arasındaki uyumsuzluk özellikle artan öğütme sürelerinde kirliliğe yol açabilen enerji yoğun bir süreçtir.

Öğütme mekanizması ile homojen malzeme üretiminde önemli rol oynayan bir çok etken vardır. Son ürün özellikleri öğütme koşullarına bağlı olmakla birlikte bu koşulların kontrolü sağlandığında iyi ürün eldesi gerçekleşir. Son ürünü etkileyen parametrelerden bazıları; öğütücü tipi, öğütme hızı, öğütme süresi, bilye-toz oranı, öğütme atmosferi, proses kontrol katışığı, öğütme sıcaklığı, öğütme kabı ve bilye boyutudur. Öğütücü tipleri, öğütme kapasitesine, öğütme hızına ve sıcaklık değişimiyle işlemi kontrol edebilme özelliğine göre farklılık gösterir. Genellikle Spex öğütücüler alaşımlama için kullanırken Fritsch Pulverisette gezegen değirmen veya atritörler çok miktarda toz öğütmek için uygundur. Öğütme süresi en önemli parametredir. Süreyi seçerken parçacıkların kırılması ve kaynaşması arasındaki dengenin göz önüne alınması gerekir. Öğütme süresinin artmasıyla kontaminasyon artar ve istenmeyen fazlar oluşur. Bu nedenle öğütmede yeterli sürenin dışına çıkılması istenmez.

Granülasyon, belirli toz özelliklerini geliştirmek için daha geniş kümeleşme içinde ince tozların kasıtlı aglomerasyonudur. Granülasyonun üç avantajı vardır. Bunlar; nihai tozların akışkanlık yeteneğine, yüksek bir paketleme yoğunluğuna ve güçlü presleme yeteneğine sahip olmasıdır. Granüllerin üretilmesinde çoğunlukla

püskürtmeli granülasyon ve püskürtmeli kurutma teknikleri kullanılmaktadır. Farklı sektör ve uygulama alanlarında çok farklı amaçlarla kullanılabilen püskürtmeli kurutma ekipmanı özellikle bir çok ince tozun paketlenme özelliklerinde yaşanan sorunlar nedeniyle presleme öncesinde püskürtmeli kurutucu ile granül haline getirilmeleri için kullanılmakta ve bu tarz ince tozların preslenebilirliklerinde bazı katkıların da katılmasıyla birlikte ciddi iyileştirme sağlanmaktadır**.**

Püskürtmeli kurutma, genellikle su veya organik bazlı süspansiyon olan akışkan malzemeyi sıcak hava ortamına püskürterek sıvının kademeli olarak sistemden ayrılmasıyla katı malzemenin granül formuna döndüğü bir yüzey küçültme işlemidir. Püskürtmeli kurutucu, atomizör yardımıyla kurutulacak çözeltinin sıcak gaz akışı içerisine ince damlacıklar halinde püskürtüldüğü düşey ve genellikle silindirik bir kurutma odasıdır. Sıvı besleme, kurutma odasına üstten püskürtülür. Oluşan damlacıklar sıcak hava ile karşılaşır. Başlangıçta püskürtülen çözelti ve hava karışımı spiral bir yol takip ederek, kurutucu tabanına doğru iner. Bu esnada çözücü buharlaşır, sıcak gaz, hava karışımı ile birlikte yönünü değiştirir, kurutucunun merkezinden yukarı geçerek kurutucuyu terk eder ve siklona gider. Kurutulmuş ürün konik tabanda toplanır. Siklona bir açı ile giren sıcak hava bir dönme hareketi ile hareket ederken santrifüj kuvvet katı parçacıkları merkezkaç kuvveti ile fırlatır ve katı parçacıklardan temizlenmiş hava siklonu terk eder. Kurutma odasındaki hava akışı modeli, sıvıdan ayrılan nemin tamamını ve granüllerin geçirildiği maksimum sıcaklığı kontrol eder. Püskürtmeli kurutmada sıvı-hava karışımı, hava dağıtıcı yeri ve atomizör cihazı aracılığıyla oluşmaktadır. Sıvı-hava karışımı; paralel akım, ters akım ve bunların birleşiminden oluşan karışık akım olarak sınıflandırılır. Paralel akım modelinde; atomizör cihazı, kurutmanın üst tarafında ve hava dağıtıcının yakınında bulunur. Ters Akım şartları atomizör cihazı kurutma odasının en üstüne ve hava dağıtıcının en alta yerleştirildiği zaman oluşur. Karışık akım şartları doğru ve ters hava akımının bir birleşimidir.

Püskürtmeli kurutma, uygun bir bağlayıcı kullanılması ile küçük partiküllerin ya da farklı kimyaya sahip tozların bir araya gelerek kompozit yapıların elde edilmesine de olanak sağlayan bir yöntemdir. Granülasyonun gerçekleştirileceği ilgili sistem için püskürtmeli kurutma parametrelerine bağlı olarak farklı boyutta ve şekilde granüllerin elde edilmesi suretiyle ilgili tozların akışkanlık davranışının geliştirilmesi ve bu suretle şekillendirme sırasında farklı paketlenme yoğunluklarına ulaşılması mümkündür. Özellikle sinterlemenin gerekli olduğu bir çok durumda şekillendirme sırasında sağlanan ve yaş yoğunluk olarak bilinen paketlenme davranışı, tozların sinterleme davranışını ve ilgili süreçte yoğunlaşmayı doğrudan etkilemektedir. PVA, kuru preslemede en çok kullanılan bağlayıcıdır. Suda çözünebilen bir bağlayıcı olarak PVA, akışkan malzemelerde kullanılmaktadır. Organik bağlayıcının püskürtmeli kurutulmuş granüllerde homojen olmayan dağılımı presleme sonrasında mikroyapısal hatalara neden olabilmektedir. Sinterleme sırasında bu şekilde oluşturulan gözenekleri kapatmak zordur. Bu durumda, gözenekler çatlak oluşturmakta ve sinterlenmiş bünyenin mukavemetini düşürmektedir.

Geçiş metal oksitleri, elektronik, kimyasal ve mekanik özelliklerinden dolayı oldukça ilgi çeken malzemelerdir. Bu çalışma kapsamında seçilen MoO_3 ve WO_3; elektrokromik, optokromik özelliklerinden ötürü akıllı cam, optik hafızalama ve gaz sensörleri gibi birçok alanda kullanılmaktadırlar. Diğer yandan bu çalışma kapsamında seçilen MoO_3 ve WO_3 periyodik tabloda aynı grupta yeralan Cr_2O_3, düşük sürtünme katsayısı, yüksek aşınma ve korozyon dayanımı ve iyi optik,

adyabatik karakter gösteren sert bir metal oksittir. Bu özelliklerinden dolayı, tribolojik ve mikroelektronik uygulamalarda koruyucu kaplama malzemesi olarak kullanılmaktadırlar.

Bu tez çalışmasında öncelikle başlangıçta mikronüstü boyutlarda olan WO_3, MoO_3 ve Cr_2O_3 tozlarının yüksek enerjili öğütme koşullarında boyut değişimleri ve nanoboyutlarda toz oluşum koşulları zamana bağlı olarak çalışılmıştır. Yüksek enerjili öğütme ile nanoboyutlara inen ya da bu boyutlarda belli fraksiyonları içeren tozların granülasyon davranışları incelenmiştir. püskürtmeli kurutmadan geçirilerek tozların karakterizasyonları yapılmıştır. Bu tez kapsamında çalışılan MoO_3, WO_3 ve Cr_2O_3 örneklerine ait başlangıç tozların, ve süreye bağlı olarak yüksek enerjili

öğütme neticesinde elde edilen tozların ve de püskürtmeli kurutma işleminden geçirilen tozların yoğunluk ölçümleri ve partikül boyutları gibi genel fiziksel özelliklerinin tespitine ilave olarak paketlenme ve sinterlenme davranışları incelenerek genel karakteristikleri ortaya konmuştur.

İlgili süreçte, partikül boyut ölçüm cihazı, X ışınları difraktometresi cihazı, yoğunluk ölçüm cihazı, stereo mikroskobu ve taramalı elektron mikroskobu gibi ileri karakterizasyon yöntemlerinden faydalanılmıştır.

x

1. INTRODUCTION

The importance of nanoparticles lies in their large surface-to-volume ratio relative to that of large particles (Baraton, 2003). Nanoparticles are a contact between bulk materials and atomic or molecular structures. While bulk materials have constant physical properties regardless of its size, among nanoparticles the size often dictates the physical and chemical properties. Thus, the properties of materials change as their size approaches the nanoscale and as the percentage of atoms at the surface of a material becomes significant (Url-1).

Two basic strategies are used to produce nanoparticles:"Bottom-Up" and "Top-Down". In the Bottom-Up systems, chemical processes make structures. The selection of the relative process lean on the chemical composition and the desired features specified for the nanoparticles. This method is form on physico-chemical principles of molecular or atomic self-organization. This approach produces selected, more complex structures from atoms or molecules, better controlling sizes, shapes and size ranges (Raab et al, 2011). Top-Down refers to mechanical-physical particle production processes based on principles of micro system technology. The traditional mechanical-physical crushing methods produce nanoparticles involving various milling techniques (Raab et al, 2011; Url-2). The mechanical production approach uses milling to crush micro particles. This approach is applied in producing metallic and ceramic nanomaterials. Compared to the chemo-physical production processes, using mills to crush particles yields final powders with a relatively broad particle-size range (Raab et al, 2011; Url-2). Mechanical alloying is a simple and useful processing technique that is being employed in the production of nanoparticles from all material classes. Although a variety of mechanical alloying devices exist, high-energy ball mills are typically used to produce particles in the nanoscale size range. Particle size reduction is affected over time in the high-energy ball mill, as is a reduction in crystallite grain size. Particle agglomeration, where nanoparticles stick together because of attractive forces, is a serious issue at long milling times (Baraton, 2003). Most powders in nanometric range are strongly agglomerated and have poor

flowability. To overcome these problems, nanoparticles can be spray-dried from a colloidal suspension to obtain micrometer-sized granules. Granules are an agglomeration of a large amount of nanoparticles (Cellard et al, 2006). Spray drying method has the capability of producing uniformly spherical particles from submicron to micron sizes. If the suspension consists of colloidal nanoparticles (primary particles), the resulting particles also comprise nanoparticles to form a nanostructured powder (Okuyama and Lenggoro, 2003).

Among metal oxides, transition metal oxides are the key parts for the development of many advanced functional materials and smart devices. Nanostructuring has appeared as one of the best tools to unlock their full potential (Zheng et al, 2011). Transition metal oxides constitute one of the most important classes of inorganic solids, exhibiting a wide variety of structures, properties. The unusual properties of transition metal oxides are due to the unique nature of the outer d electrons, the metal-oxygen bonding varying anywhere from nearly ionic to metallic (Rao and Raveau, 1998). These materials can have unusual and useful electronic, magnetic, chemical, and mechanical properties. Many of these properties strongly depend on materials defects like vacancies, dislocations, stacking faults and grain boundaries. These defects affect local oxygen bonding (Cox, 1992; Rao and Raveau, 1998). Among the transition metals, VIB group elements (W, Mo, and Cr) show interesting properties such as high corrosion resistance and high temperature stability which make them useful in many applications and industries. In addition, the oxides of VIB elements have electrochromism ability means they are able to change their optical properties in a reversible and persistent way under the action of a voltage pulse (Zheng et al, 2011; Ivanova et al, 2011).

Tungsten oxides, which are one of the transition metal oxides, are of great interest. With electrochromic, optochromic, and gaschromic properties, tungsten oxides have been used to construct flatpanel displays, photoelectrochromic smart windows, optical modulation devices, write-read-erase optical devices, gas sensors, humidity and temperature sensors, etc. (Zhou et al, 2005). Tungsten has several common oxidation states like +2, +3, +4, +5, and +6. Tungsten is stable, and therefore its most common valence state is +6 (Lassner and Schubert, 1999). WO_3 has a perovskite-like structure. The corner and edge sharing of WO_6 octahedra form crystals of WO_3. Such corner sharing results in the following crystal phases: monoclinic I (γ), monoclinic II

(ε), triclinic (δ), orthorhombic (β), tetragonal (α), and cubic (although cubic is not a commonly observed phase). At room temperature, γ-WO_3 is the most stable crystal phase (Zheng et al, 2011). WO_3 has a density of 7.16 g/cm^3, and its melting point is 1473 °C (Lassner and Schubert, 1999). Nanostructured WO_3 compared to the bulk material include: 1) Increased surface-to-volume ratio, which provides more surface area for both chemical and physical interactions. 2) Significantly altered surface energies that allow engineering of the material's properties, as atomic species near the surface have different bond structures than those embedded in the bulk, and 3) Quantum confinement effects, due to the inherently small size of nanostructured materials, that significantly influences charge transport, electronic band structure and optical properties (Zheng et al, 2011).

MoO_3 is used in many applications such as electrochromic display devices, optical memories, gas sensors and lithium batteries, organic solar cells and smart window technology because of its wide range of stoichiometry leading to chromogenic and catalytic properties (Walia et al, 2013; Ramana et al, 2007). The most common crystal phases of MoO_3 are the thermodynamically stable α-MoO_3 and the metastable β-MoO_3. At temperatures above 350 °C, the β phase transforms into the more stable, layered α-MoO_3 phase (Walia et al, 2013). The structural flexibility inherent in molybdenum trioxide and its hydrates makes it possible to synthesize many morphologies, such as molybdenum trioxide prisms and nanorods, nanotubes, hollow MoO_3 nanospheres and nanostructured toroids, MoO_3 fibers and nanobelts (Ortiz and Herrera, 2012). MoO_3's density is 4.69 g/cm^3 and its melting point is 795 °C (Rao et al, 2013).

Chromium oxide is another one of the transition metal oxides. There are many crystalline modifications of the chromium oxide, such as Cr_2O_3 (corundum), CrO_2 (rutile), Cr_5O_{12} (three-dimensional framework), Cr_2O_5 and CrO_3 (unconnected strings of CrO_4 tetrahedral). However, the only stable bulk oxide form is Cr_2O_3, which is a magnetic dielectric with the corundum structure (Maldonado et al, 2012). Similar to corundum, Cr_2O_3 is a hard, brittle material (Mohs hardness 8-8.5). It has a high melting point of 2435 °C and density of 5.22 g/cm^3. Because of its considerable stability, chromia is a commonly used pigment. It is used in paints, inks, and glasses. It is one of the materials that are used when polishing the edges of knives, razors, etc on a piece of leather, balsa, cloth, or other material (Udy, 1956). Chromium oxide is

the hardest oxide that also exhibits low friction coefficient, high wear and corrosion resistance, and good optical and adiabatic characteristics. These properties allow it to be used as a protective coating in tribological and microelectronic applications (Pang et al, 2007).

Keeping the above concepts in mind, the aim of this study has been to develop WO_3, MoO_3 and Cr_2O_3 powders via high-energy milling and spray drying processes and characterize their properties and sintering behavior.

2. GENERAL PRODUCTION ROUTES OF CERAMICS

A variety of powder preparation methods have been developed so far. They are classified in two groups. One is breakdown process, in which large particles are ground and divided into smaller ones, and the other is referred to as a build-up process, in which particles are produced by precipitation and deposition (Vincenzini, 1991). Many specific techniques can be used for the production advanced ceramics. A general route is described below for the powder-based production of ceramic bulk materials.

2.1 Starting Materials

Properties of most ceramic products are determined by the properties of the raw material powders, which some requirements are fine particles (<1 μm), narrow size range, no aggregation, controlled particle shape, uniformity in chemical and phase compositions, and high purity (Vincenzini, 1991).

2.2 Mixing or Blending

After selection of the materials, the next step is blending or mixing. Mixing step affects the final distribution of reinforcement particles and porosity in green compacts, which strongly has an influence on the mechanical properties of the final products (Lindroos et al, 2004). After all, there are some problems, such as segregation and clustering. The reasons of these problems include different flow characteristics between metal powder and reinforcement particles and the tendency of the agglomeration of particles to minimize their surface enerfy. The segregation behavior of different sized particles is shown in Figure 2.1 (Liu et al, 1994).
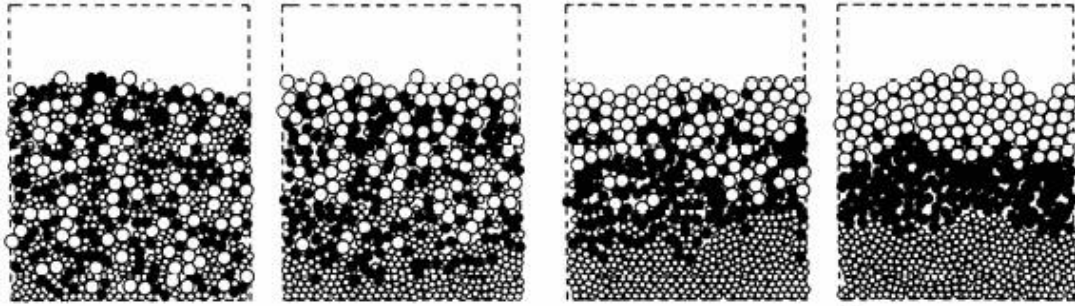
Figure 2.1: Monte Carlo simulations of shaking of a ternary mixture of particles according to number of cycles (Liu et al, 1994).

As seen in figure 2.1, the larger particles rise to top, because they are moved upwards as smaller particles filled the voids beneath the larger particles. Furthermore, the effect of different densities between particles is very important, too. The lighter particles tend to move upwards, while the heavier ones segregate at the bottom (Lindroos et al, 2004). However, these segregation and clustering problems can be overcome by milling process (Liu et al, 1994). In addition, milling is used to reduce the particle sizes. This technique will be discussed in detail in section 3.

2.3 Forming

Shape forming techniques can be divided into techniques such as dry pressing, powder injection moulding and extrusion, and wet colloidal forming techniques such as spray drying, slip casting, gelcasting, hydrolysis assisted solidification, etc. The reliability of dry pressing ceramics is limited by defects due to agglomerates. Manufacturing of ceramic components by powder pressing usually requires a granulation operation prior to pressing. The goal is to gain free flowing granules that evenly fill the pressing dye and easily disintegrate at pressing. Granulation is normally conducted by an initial mixing of the powder and appropriate pressing aids (binder, plasticiser) in a liquid. The suspension can then be dried with some remaining liquid and sieve granulated (small scale) or spray-dried (large scale) (Rak, 2000; Rundgren et al, 2003). Granulation process will be discussed in detail in section 4.

2.4 Sintering

Sintering is a processing technique used to produce density-controlled materials and components from metal or/and ceramic powders by applying thermal energy (Kang, 2005). In sintering, particles bond with one another by atomic diffusion. There are different variables, which determine sinterability and the sintered microstructure of a powder compact. All sintering equations contain a number of parameters such as diffusion coefficient, surface tension, particle size, initial pore volume. One can divide these parameters into two classes: a) intrinsic and b) extrinsic (Upadhyaya, 2001).

1. Intrinsic - these specify the intrinsic properties of the materials being sintered, such as surface tension, diffusion coefficient, vapour pressure, viscosity, etc. These properties change when the chemical composition, ambient atmosphere or temperature changes (Upadhyaya, 2001).

2. Extrinsic – these depend on the geometrical or topological details of a system. These include parameters, as average particle size, particle or pore or grain shape and size distribution, etc (Upadhyaya, 2001).

Sintering processes can be divided into two types: solid state sintering and liquid phase sintering. *Solid state sintering* occurs when the powder compact is densified wholly in solid state at the sintering temperature, while *liquid phase sintering* occurs when a liquid phase is present in the powder compact during sintering (Kang, 2005). In addition to solid state and liquid phase sintering, other types of sintering, for example, transient liquid phase sintering and viscous flow sintering can be utilized. Viscous flow sintering occurs when the volume fraction of liquid is sufficiently high, so that the full densification of the compact can be achieved by a viscous flow of grain-liquid mixture without having any grain shape change during densification. Transient liquid phase sintering is a combination of liquid phase sintering and solid state sintering. In this sintering technique, a liquid phase forms in the compact at an early stage of sintering, but the liquid disappears as sintering proceeds and densification is completed in the solid state (Figure 2.2) (Kang, 2005).
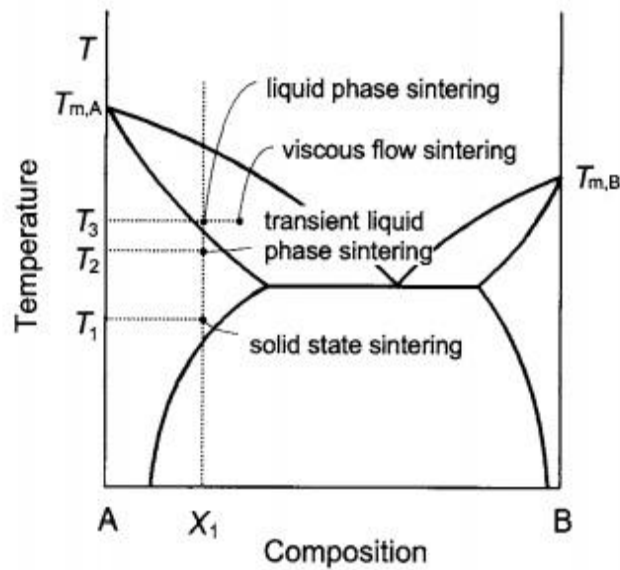
Figure 2.2: Illustration of various types of sintering (Kang, 2005).

The driving force for sintering is the minimization of the solid-vapor interface area (i.e., the total area of the powders in contact with the surrounding vapor) and elimination of the regions of sharp curvature at powder contacts. In the initial stages of sintering, small necks form and grow between contacting particles by mass transfer via atomic diffusion. Fine powders increase the driving force for sintering because of a larger surface area per unit volume, which increases the total solid-vapor interfacial energy (Asthana et al., 2006). Figure 2.3 shows different patterns of atomic motion, leads to various sintering mechanisms.
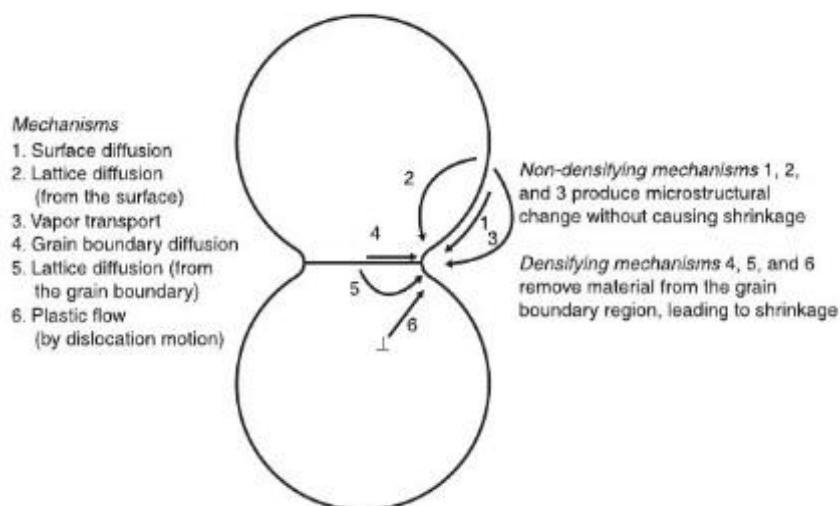
Figure 2.3: Various sintering mechanisms (Fang, 2010).

2.4.1 Solid-state sintering:

These three main steps occur while solid-state sintering:

Initial Stage: Particle surface smoothing and rounding of pores, grain boundaries form, neck formation and growth, homogenization of segregated material by diffusion, open pores and small porosity decreases <12% (Ring, 1996).

Intermediate Stage: Intersection of grain boundaries, shrinkage of open pores, porosity decreases substantially, slow grain growth and differential pore shrinkage, and grain growth in heterogeneous material (Ring, 1996).

Final Stage: Closed pores—density >92%, closed pores intersect grain boundaries, pores shrink to a limiting size or disappear and pores larger than the grains shrink very slowly (Ring, 1996).
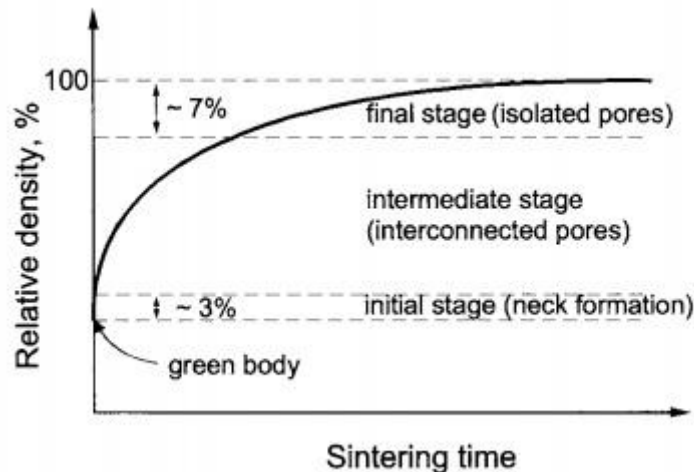
Figure 2.4: Schematic showing the densification curve of a powder compact and the three sintering stages (Kang, 2005).

Metallurgical bonds occur between the powder particles during sintering. Moreover, some desirable properties such as strength, ductility, toughness and electrical and thermal conductivities are also improved when the density increases. As a result of the density increase, initial dimensions of the compact decreases. However, the compacted part should be suitably oversized to have desired tolerances, so the porosity is not fully removed. In addition, between 5% and 25% residual porosity usually remain in the final pressed and sintered powder metallurgy products (Newkirk and Kohser, 2004).

3. HIGH ENERGY MILLING

Particle size reduction or comminution is an important step in lots of technological operations. This process contains the mechanical breakdown of solids into smaller particles without changing their state of aggregation. It can be used to create particles of a certain size and shape (including nanosize), to increase the surface area and reduce defects in solids which is needed for following operations such as chemical reactions, sorption, etc. Besides increasing the surface area of solids, milling could increase the proportion of regions of high activity in the surface (Balaz et al, 2004).

Conventionally, the term fine milling is used for size range below 100 μm and the ultrafine (or very fine) milling for particles size less than 10 μm. In mechanochemistry, the term high-energy milling is usually being used in order to stress the character of applied milling equipments (mills) (Balaz, 2008).

High-energy milling as a way for nanomaterials synthesis has been firstly developed in metallurgy as a mean to produce oxide dispersion strengthened solids. Later the application has been directed to the preparation of alloys, superconducting materials, rare permanent magnets, superplastic alloys and intermetallic compounds. In addition, this technique can be used to induce chemical reactions in powder mixtures at room temperature or at much lower temperatures than normally required to synthesize pure metals (Balaz et al, 2004).

3.1 Types of Mills

Different types of high-energy milling equipment are used to produce mechanically alloyed powders. Spex Mixer/mills, planetary ball mills, attritor mills and commercial mills are the examples of widely used equipment for this purpose. They have different capacity, efficiency of milling and additional arrangements for cooling, heating, etc (Suryanarayana, 2001; Goff, 2003). Spex Mixer/mills can mill about 10-20 g powder at a time depending on the density of starting constituents (Goff, 2003). Typical Spex mill and tungsten carbide vial set can be seen in Figure 3.1.
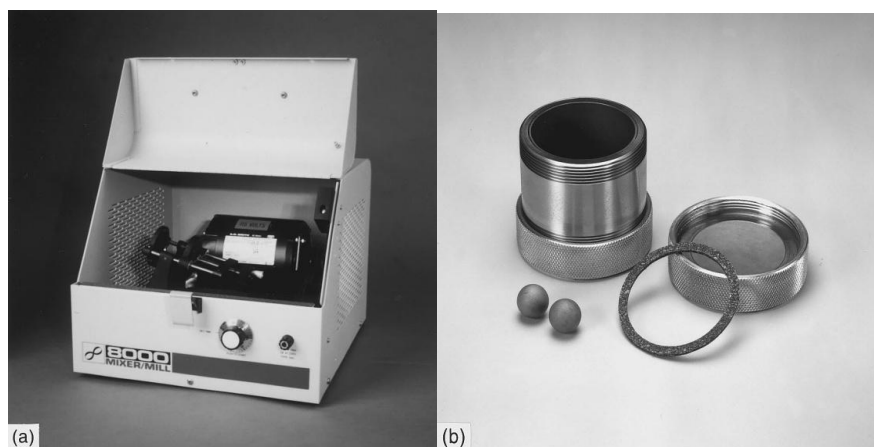
Figure 3.1: a) A typical Spex shaker mill **b)** Tungsten carbide vial set consisting of the vial, lid, gasket, and balls (Suryanarayana, 2001).

One of the popular mills for laboratory investigations is the planetary ball mills. It is called the planetary ball because of its vial's planet-like movement. The centrifugal force produced by the vials rotating around their own axes act on the vial contents, consisting of material to be ground and the grinding balls. As a result, powders are trapped between the rotating balls and the walls of the vial and refined. Even though the linear velocity of the balls in this type of mill is higher than that is in the Spex mills, the frequency of impacts is much more in the Spex mills (Suryanarayana, 2001).

Therefore, compared to Spex mills, planetary ball mills can be considered lower energy mills (Suryanarayana, 2001). In Figure 3.2, a schematic view of ball motion in a planetary ball mill can be seen.
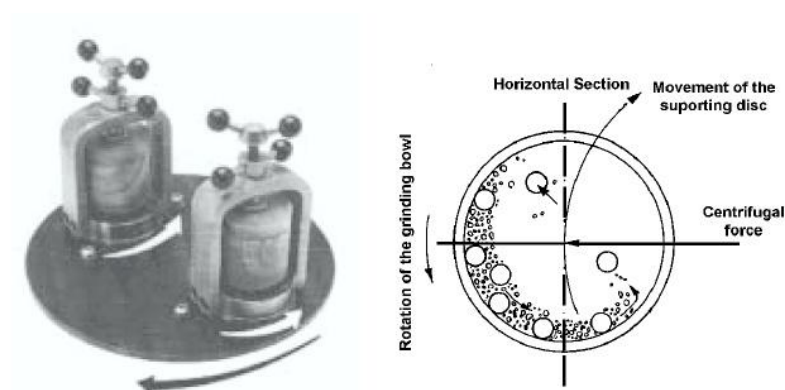
Figure 3.2: Schematic drawing of a high-energy planetary ball mill (El-Eskandarany, 2001).

Another type of mills is the attritor mill. In attritor mills, large quantities of powder (from about 0.5 to 40 kg) can be milled at a time (Suryanarayana, 2001). Schematic view of an attritor mill is given in Figure 3.3.
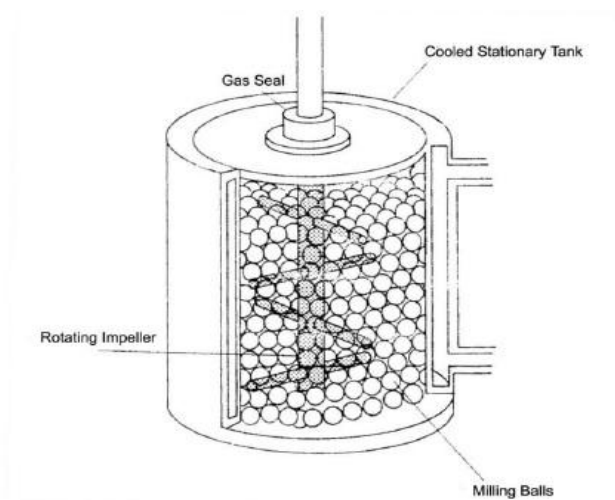
Figure 3.3: A schematic view of an attritor mill (Goff, 2003).

Finally, commercial mills are much larger than the mills described above and can grind several hundred kilograms of powders at a time. Milling for commercial production is carried out in ball mills of up to about 1250 kg capacity (Suryanarayana, 2001). A picture of commercial-size ball mills can be seen in Figure 3.4.
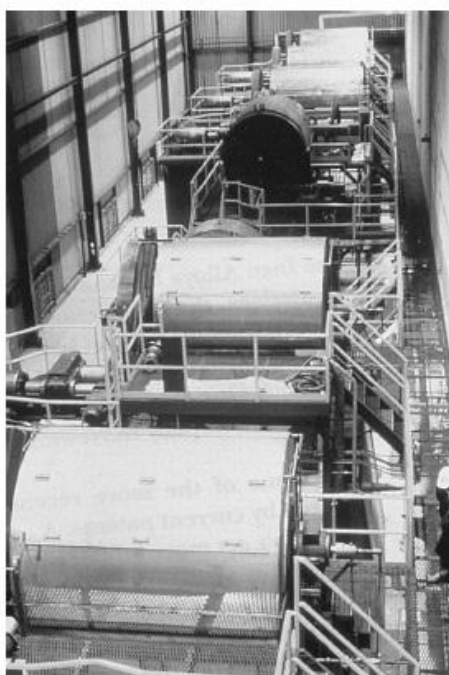
Figure 3.4: Commercial production-size ball mills (Suryanarayana, 2001).

The milling time decreases with an increase in the energy of the mill. Roughly, it can be estimated that a process that takes only a few minutes in the Spex mill may take hours in an attritor and a few days in a commercial mill (Suryanarayana, 2001).

3.2 Process Variables in Milling

Ball milling process is influenced by several factors that play very important roles in the fabrication of homogeneous materials. The properties of the milled powders of the final product, such as the particle size distribution, the degree of disorder, or amorphization, and the final stoichiometry, depend on the milling conditions and, as such, the more complete the control and monitoring of the milling conditions, the better end product is obtained (El-Eskandarany, 2001; Suryanarayana, 2001)

A summary of these chief factors that control the milling process is schematically presented in Figure 3.5.

Figure 3.5: Schematic presentation of the main factors that affect the milling process (El-Eskandarany, 2001).

The material used for the milling container (grinding vessel, vial) is important since the impact of the grinding medium on the inner walls of the container will result in tiny fractions of milling material that fracture off and disperse into the powder (El-Eskandarany, 2001; Suryanarayana, 2001). These can contaminate the powder or alter the chemistry of the powder. If the material of the grinding vessel is different from that of the powder, then the powder may be contaminated with the grinding

14

vessel material (Suryanarayana, 2001; Goff, 2003). Regardless of the type of milling process, the most appropriate type of container and milling media for the given system should be chosen. Generally, milling media that is made of a similar material as that of the material to be processed is used to reduce contamination during processing (Goff, 2003). Additionally, the density of the grinding medium should be high enough so that the balls create enough impact force on the powder (Suryanarayana, 2001).

Another important issue is the ball-to-powder ratio (BPR). The value of BPR has been varied by different investigators from a value as low as 1:1 to as high as 220:1. Generally, a ratio of 10:1 is most commonly used while milling the powder in a small capacity mill such as a Spex mill. The BPR has an important effect on the time required to achieve a particular phase in the powder being milled. The higher the BPR, the shorter is the time required (Suryanarayana, 2001).

Milling atmosphere is also an important variable for the mechanical alloying process. The major effect of the milling atmosphere is on the contamination of the powder (El-Eskandarany, 2001). The powders are milled in containers that have been either vacuumed or filled with an inert gas such as argon or helium. However, high purity argon is the most common used gas to prevent oxidation and contamination of the powder (Suryanarayana, 2001). The presence of air in the vial causes to produce oxides and nitrides in the powder, especially if the powders are reactive in nature. Thus, the loading and unloading of the powders into the vial has to be carried out inside an atmosphere-controlled glove box (Suryanarayana, 2001; Fecht, 2002). The time of milling is the most important parameter. In most of milling processes, the rate of refinement of the internal structure (particle size, crystallite size, lamellar spacing, etc.) is roughly logarithmic with processing time (Figure 3.6). In a few minutes to an hour, the lamellar spacing usually becomes small and the crystallite (or grain) size is refined to nanometer dimensions. Furthermore, the times required depend on the type of the mill used, the intensity of milling, the ball-to-powder ratio and the temperature of milling. These times have to be decided for each combination of the above parameters and for the particular powder system. However, it should be realized that the level of contamination increases and some undesirable phases form if the powder is milled for times longer than required. Therefore, the powder has to be milled just for the required duration and not any longer (Suryanarayana, 2001).
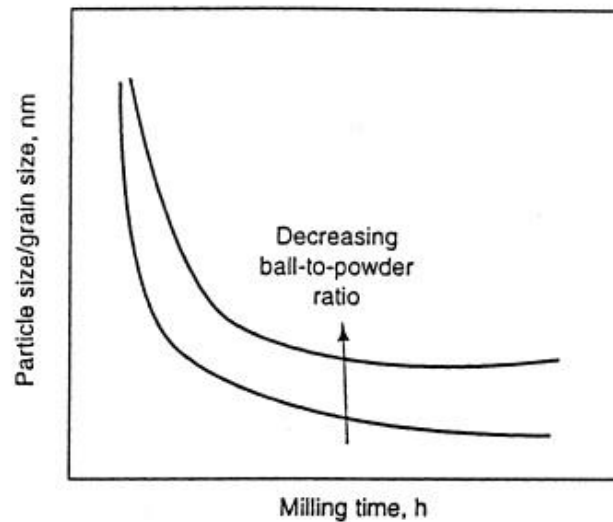
Figure 3.6: Refinement of particles and grain sizes with milling time (Suryanarayana, 2001).

The use of process control agents (PCA) is another concern in the milling process. Generally, ductile powder particles get cold-welded to each other, resulting from intense plastic deformation during milling. However, true alloying among powder particles can occur only when a balance is maintained between cold welding and fracture of particles (El-Eskandarany, 2001). In order to provide the right dynamic balance between cold welding and fracturing, a process control agent (PCA) is added to the powder mixture during milling to reduce the amount of cold welding (Öveçoğlu, 1987; Suryanarayana, 2001; Gilman and Benjamin, 1983). The PCA's can be solids, liquids, or gases. They are mostly organic compounds, which act as surface-active agents by adsorbing on the surface of the powder particles and minimizing cold welding between powder particles and thereby inhibiting the agglomeration (Suryanarayana, 2001).

3.3 Mechanism of Milling

Milling is an advanced fabrication process that can produce ultra-fine and homogenous powders. Even, nanocrystalline materials (with a grain size of few nanometers, usually<100 nm) are also produced by mechanical alloying (MA) of powder mixtures (Ryu et al., 2000).

During high-energy milling, the powder particles are repeatedly flattened, cold-welded, fractured and rewelded. When two steel balls collide, some amount of powder is trapped in between them. The force of the impact plastically deforms the powder particles leading to work hardening and fracture. Figure 3.7 is a schematic representation of the collided balls. (Suryanarayana, 2001).
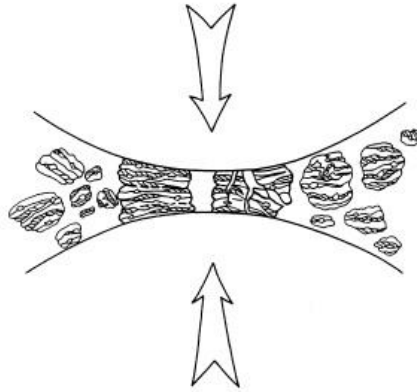
Figure 3.7: Schematic view of a ball-powder-ball collision (Suryanarayana, 2001).

It is possible to conduct mechanical alloying of three different combinations of metals and alloys:

(1) Ductile-ductile

(2) Ductile-brittle

(3) Brittle-brittle systems (Suryanarayana, 2001).

3.3.1 Ductile-ductile systems

The ideal combination of materials for mechanical alloying is the ductile-ductile systems. It is necessary to have at least 15% of a ductile component for achieving alloying. This is because true alloying occurs due to the repeated action of cold welding and fracturing of powder particles. Cold welding cannot occur if the particles are not ductile. At the first step of mechanical alloying (MA), the ductile components get flattened to platelet/pancake shapes by a micro-forging process. A small quantity of the powder, usually one or two particle thickness, also gets welded onto the ball surfaces. This coating of the powder on the grinding medium is advantageous since it prevents excessive wear of the grinding medium. In the next step, these flattened particles get cold-welded together and form a composite lamellar structure of the constituent metals. An increase in particle size is also observed at this

stage. With increasing MA time, the composite powder particles get work hardened, the hardness and brittleness increase. With further milling, the elemental lamellae of the welded layer and both the coarse and fine powders become convoluted rather than being linear. The hardness and particle sizes tend to reach a steady value at this stage. Finally, true alloying occurs at the atomic level resulting in the formation of solid solutions, intermetallics, or even amorphous phases. The layer spacing becomes so fine or disappears at this stage that it becomes invisible under an optical microscope (Suryanarayana, 2001).

3.3.2 Ductile-brittle systems

In the initial stages of milling, the ductile metal powder particles get flattened by the ball-powder-ball collisions, while the brittle oxide or intermetallic particles get fragmented. These fragmented brittle particles get trapped in the ductile particles. With further milling, the ductile powder particles get work hardened, the lamellae get convoluted, and refined. The composition of the individual particles converges toward the overall composition of the starting powder blend. With continued milling, the interlamellar spacing decreases, and the brittle particles get uniformly dispersed. The alloying process in a ductile-brittle system also depends on the solid solubility of the brittle component in the ductile matrix. If a component has a few solid solubility then, alloying is unlikely to occur, e.g., boron in iron (Suryanarayana, 2001).

3.3.3 Brittle-brittle systems

This type of alloying occurs when a consisting of two or more brittle components, because the absence of a ductile component prevents any welding from occurring, and in its absence, alloying is not expected to occur. The brittle components get fragmented during milling and their particle size gets reduced. However, at very small particle sizes, the powder particles behave in a ductile mode, and further reduction in size is not possible. During milling of brittle-brittle component systems, the harder (more brittle) component is fragmented and is embedded in the softer (less brittle) component (Suryanarayana, 2001).

Recently, MA process has become a popular method to fabricate nanocrystaline materials due to its simplicity and relatively inexpensive equipment (El-Eskandarany et al., 2000; El-Eskandarany, 2001). The advantage of using MA for the synthesis of nanocrystalline materials lies in its ability to produce bulk quantities of material in

the solid state using simple equipment and at room temperature (Suryanarayana, 2001). Grain sizes with nanometer dimensions have been observed in almost all MA'd pure metals, intermetallics, and alloys (Suryanarayana, 2001). The elemental processes leading to formation of nanostructures include three basic stages. Firstly, the deformation is localized in shear bands, which contain a high dislocation density (Fecht, 2002). Their typical width is approximately 0.5-1 μm (Suryanarayana, 2001). At a certain level of strain within the high strained regions, these dislocations annihilate and recombine to small-angle grain boundaries separating the individual grains (Fecht, 2002). This results in a decrease of the lattice strain. With the continuing process, deformation occurs in shear bands located in previously unstrained parts of the material. The grain size decreases steadily and the shear bands unite. The small angle boundaries are replaced by higher angle grain boundaries and, consequently, dislocation-free nanostructured grains are formed (Suryanarayana, 2001).

3.4 Reported Milling Investigations of WO_3, MoO_3 and Cr_2O_3 Powders

Cellard et al. investigated spherical micron-sized Cr_2O_3 granules by spray-drying method. But this technique requires stable and well-dispersed suspensions (Cellard et al, 2007). For this reason, Cr_2O_3 nanopowders dispersion was developed and optimized by a ball milling method for producing granules. According to Cellard et al., the appropriate dispersant, Darvan C, was selected with zetapotential measurements (Cellard et al, 2007). The effect of milling time, diameter of milling balls and ball-to-powder ratio was investigated. Well dispersed and stable suspension, suitable for spray-drying, is achieved at natural pH, with 1.3 wt.% of Darvan C, after 95 h of desagglomeration with milling balls diameter 0.9–1.9 mm and a weight ratio of 7 (Cellard et al, 2007).

Mestl et al. investigated the effect of the mechanical activation of MoO_3 upon particle size and morphology (Mestl et al, 1995). After 600 mins of milling, BET surface area increases from 1.3 to 32 m^2/g and the particle size decreased from 1 μm to about 50 nm. Also, they investigated decreasing primary crystallite size from about 160 nm to about 80 nm (Mestl et al, 1995). In another experiment Mestl et al. investigated the defects at the crystallite surfaces and redox behaivior of MoO_3 powders which causes by mechanical activation of MoO_3 (Mestl et al, 1996). They

demonstrated that both milled and unmilled MoO_3 have 5-fold coordinated Mo^{5+}, but milled MoO_3 has 6-fold coordinated Mo^{5+} additionally (Mestl et al, 1995; Mestl et al, 1996).

4. GRANULATION

Granulation is a size enlargement process during which primary particles are shaped into larger, physically strong agglomerates wherein the primary particles can still be identified. There are three main advantages of granulation: 1) the resulting powders have flowability, 2) a high packing density, and 3) strong compactability (Kim and Jung, 2007). Despite these advantages, the granules often lead to internal defects, which can cause a premature fracture and low reliability of the sintered parts. These problems arise from the fact that the granules with large internal pores do not collapse during compaction and remain after sintering. The formation of large donut-shaped open pores or deep craters is associated with the migration of ceramic particles from the interior of the granule onto its surface during the hot drying process (Kim and Jung, 2007; Reeds, 1997).

Granulation methods can be divided into agitation, pressure, or spray techniques as shown in Figure 4.1.
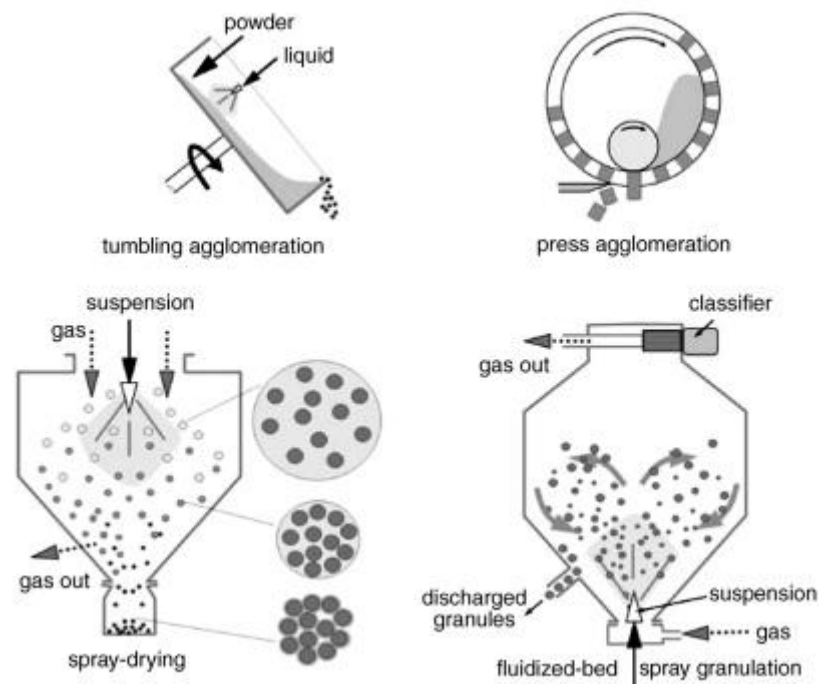
Figure 4.1: Common granulation methods (Riedel and Chen, 2012).

4.1 Granulation by Agitation

Granulation by agitation involves bringing moist particles into contact by mixing or tumbling so that bonding forces can cause agglomeration. The agitation granulation techniques, both tumbling and mixing, are typically used to prepare feedstock for calcining or melting operations. Bulky powders are granulated prior to these operations if the improvements in heat transfer, flow properties, and bulk density can be justified on either a cost or technical basis. Granules formed by agitation techniques are subjected to destructive forces, within the moving powder charge, that oppose those forces causing agglomeration. The balance between these forces determines the maximum granule size possible under given process conditions (Lukasiewicz, 1991).

4.2 Granulation by Pressure

Size enlargement by pressure granulation is accomplished by compressing a powder while it is held in a confined space. Pellets formed are usually of a regular, but non-spherical, geometry. Common techniques include roll briquetting, pelletizing, and extrusion. Granules produced by roll briquetting are commonly in the form of a "pillow" shape as the powder is pressed between matching indentations in the rolls. Pressure is applied to the rolls hydraulically. Pellet mills form cylindrical shapes by compressing and forcing moist powder through an orifice. A binder can be added to the powder to promote adhesion, increase pellet strength, and act as a lubricant. Extrusion is accomplished by forcing a plastic powder mass through either an orifice or a perforated plate. The extruder can be either the piston or the auger type. Water and binder solutions must be added to materials that are not already in a plastic condition. Pressure granulation techniques typically produce large granules and are used in the ceramic industry to form a feed material for calcining or melting operations. They can also be used to prepare the feedstock for injection-molding processes. They are not used to produce press-powders for automatic presses (Lukasiewicz, 1991).

4.3 Granulation by Spraying

Spray techniques are often used to prepare granulated powder for automatic presses because they tend to yield dust-free, highly flowable powders of constant bulk density. The most commonly used methods are spray drying and spray granulation. The feed for a spray dryer is a solid-liquid suspension. For a spray granulator, it is usually a dry or slightly moist bulky powder. Spray granulation is commonly used in the pharmaceutical industry to prepare feedstock for tablet presses. It is used less frequently in the ceramic industry for producing press-powder because many ceramic powders are wet-milled prior to granulation and would have to be dried before being spray granulated (Lukasiewicz, 1991).

4.3.1 Spray Drying

Spray drying is one of the most important granulation methods. As most ceramic powders undergo a suspension-based pre-processing step such as wet milling or mixing, the combination of drying and agglomeration processes is obvious (Riedel and Chen, 2012). This process consists of the transformation of an aqueous slurry into dry spherical powders, often called granules, by spraying the slurry, which contains ceramic powders, a dispersant, binder, plasticizer, antifoaming agents, and if necessary a lubricant, into a hot drying medium (Kim and Jung, 2007).
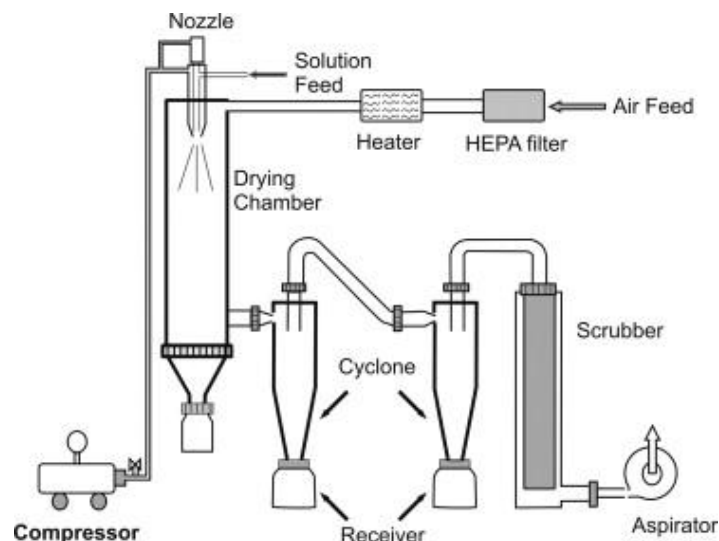
Figure 4.2: A schematic view of spray dryer (Peighambardoust et al., 2011).

In spray drying, the suspensions are atomized into small droplets and injected into a hot gas stream. In most cases, water is used as the suspension fluid and air as the

drying gas, although in special cases organic liquids such as alcohol and inert drying gases are utilized. When in contact with the gas stream, the suspension fluid evaporates from the droplets. Ideally, the spherical shape of the droplets is preserved and the pressing aids are homogeneously precipitated onto the primary particle surfaces, after which the dry granules are separated from the gas stream and collected in a chamber. Atomization ideally results in the formation of droplets with the desired size and a narrow size distribution. It is carried out using centrifugal atomizers, pressure nozzles, or two-fluid nozzles (Riedel and Chen, 2012).

Drying of the suspension droplets occurs in two characteristic stages (Figure 4.3). The droplets reach equilibrium with the drying air within several milliseconds, without any significant change in moisture content; subsequently, the drying continues at a constant rate, as long as the surface remains saturated with the liquid. The droplet diameter decreases during this stage, but the surface temperature remains constant. At the so-called critical point, the drying rate decreases, as the liquid–vapor interface recedes into the porous material and the subsurface temperature increases. This phase is extended until almost all of the liquid has evaporated. Ideally, the critical point is reached when the primary particles come into contact and form a homogeneous packing (Reeds et al., 1999).
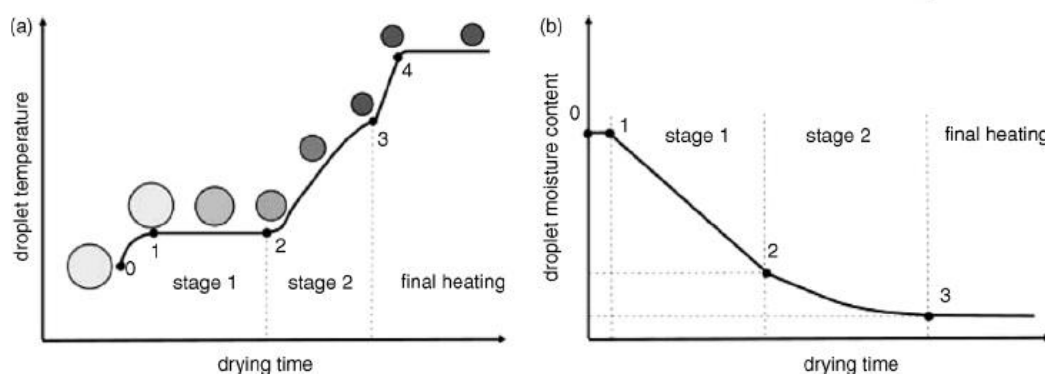
Figure 4.3: a) Droplet temperature and **b)** Droplet moisture content during the characteristic stages of the spray-drying process (Riedel and Chen, 2012).

A rapid drying and high particle mobility favor the formation of a rigid particle shell at the surface, before the particles in the interior of the droplet are exposed to each other. In this case, the drying rate is decreased as the low permeability of the shell hinders the liquid flow to the surface. Ultimately, the shell structure leads to the

formation of hollow granules that often exhibit craters or so-called blowholes formed by an inward collapse of the shell. Such collapse may be explained by the formation of a partial vacuum by the capillarity-induced movement of particles from the interior to the surface shell. Preferably, hollow granules should be avoided in ceramic pressing as they disturb the packing homogeneity and are clearly a source of pressing defects (Reeds et al., 1999).

The characteristics of spray-dried granules depend on multiple parameters. Besides the drying conditions, the particles of the base powder and the additives introduced into the suspension play an important role. As the ideal granule should be a uniform solid sphere, a too-rapid drying must be avoided as this causes the formation of a rigid surface, before the droplet has reached its stable spherical shape after atomization, and will result ultimately in a hollow granule. Hollow granules are favored by using highly deflocculated slurries and low solids loading of the suspension (Riedel and Chen, 2012). General morphology of particle preparing by spray drying method is illustrated in Figure 4.4.

Spray droplet and drying gas movement occur under co-current, counter-current, or mixed-flow conditions (Figure 4.5). A co-current flow means flow in the same direction, and is applied to coarse products, whereas the counter-current arrangement has excellent heat utilization and is applied to non-heat-sensitive materials. Both methods are integrated in the case of mixed-current flow, in which the drying chambers may have large dimensions of up to several meters, from the bottom of which the coarse granules can be discharged, with the chamber acting as a cyclone separator and the fines being separated by a second, high-efficiency cyclone separator (Riedel and Chen, 2012).
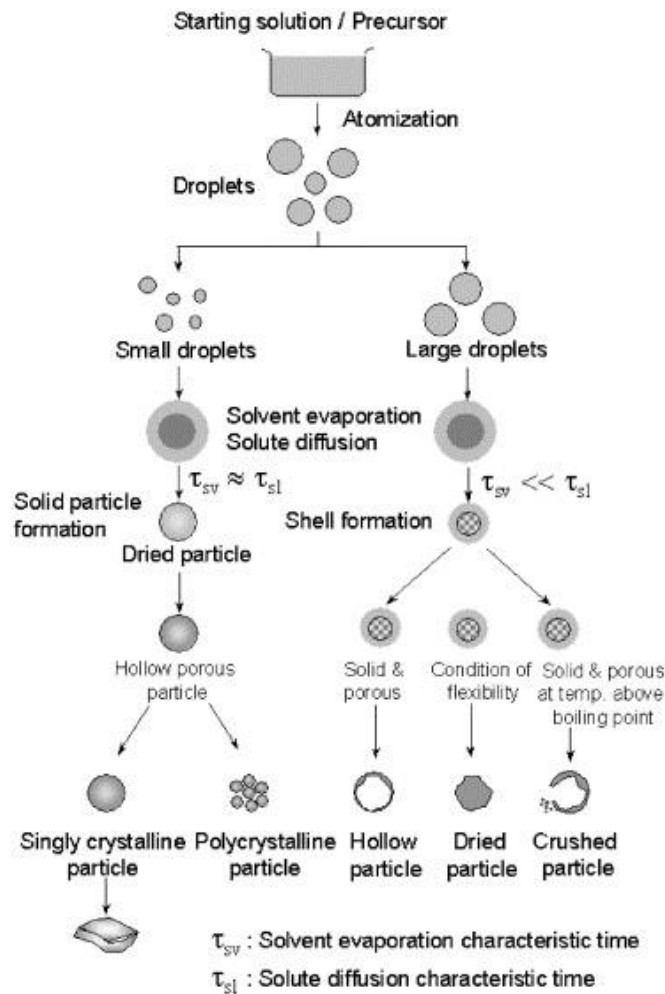
Figure 4.4: Morphology of particle preparing by spray drying (Okuyama and Lenggoro, 2003).
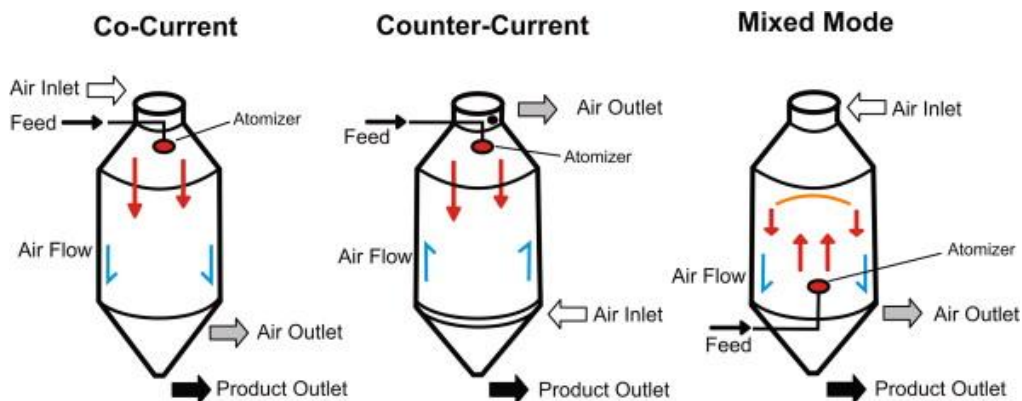
Figure 4.5: Typical product-air flow patterns in spray dryers (Peighambardoust et al., 2011).

The binder is the most important ingredient for spray drying, since the binder determines the flowability, bulk density, and compaction behavior of the granules.

An adequate binder for spray drying should confer high green strength to the compact article at the lowest possible addition. The parameters controlling binder performance are the glass transition temperature (T_g), polymer backbone structure, molecular weight, viscosity, and hygroscopicity. The binders commonly used in spray drying are water-soluble polymers such as polyvinyl alcohol (PVA), cellulose, polyethylene glycol (PEG), and polyacrylate. The selection criteria for the binder are based on its ability to form granules that readily deform during compaction, to burn out cleanly before sintering, and to give a high compact density and strength. In addition, to prevent a hard granule surface from forming, the binder should undergo minimal migration onto the granule surface while spray drying the powder (Kim and Jung, 2007). Slurries that contain binder solutions have a tendency to foam when subjected to high shear strain rates during mixing. The resulting trapped air is often incorporated in the granules and lowers their density. The addition of a defoaming agent can be helpful when foaming cannot be prevented (Lukasiewicz, 1991).

4.4 Reported Granulation Investigations of WO_3, MoO_3 and Cr_2O_3 Powders

Some works held before about the granulation method. Cellard et al. investigated spherical micron-sized granules by spray-drying method for development of wear-resistant plasma sprayed nanostructured coatings from nanopowders (Figure 4.6) (Cellard et al, 2006). According to Cellard et al., stable and well-dispersed suspension was achieved by milling process with adding 1.3% wt Darvan C as dispersant agent. This optimized colloidal suspension was spray-dried. The maximum flowability and packed density of the granulated powder was obtained with a slurry feed rate of 7.5 ml/min and a binder concentration of 2% wt (Cellard et al, 2006).
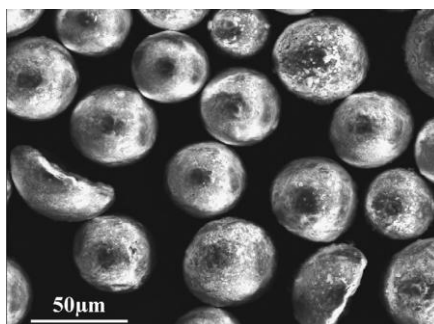
Figure 4.6: Cr_2O_3 granules obtained from optimized slip by spray-drying (Cellard et al, 2006).

In another research, Liu et al. investigated superfine WO_3 granules from NH_4OH/WO_3 solution by spray drying process. They studied the effect of centrifuge rotary speed and the ratio of NH_4OH/WO_3 on the spray-drying process. They demonstrated that the size of the precursor of tungsten powder is related to the centrifuge rotary speeds and the size of centrifuge disk, while the density of the precursor of tungsten powder is related to the ratio of NH_4OH/WO_3 and the WO_3 concentration in $(NH_4)_2WO_3$ solution (Liu et al, 2012).

Lyo et al. investigated microstructure and tribological properties of plasma-sprayed chromium oxide-molybdenum oxide composite coatings (Lyo et al, 2003). Plasma-sprayed Cr_2O_3 coatings are used in internal combustion engines because of its high wear resistance. On the other hand, molybdenum is used in plasma-sprayed piston ring and synchronizer ring coatings to enhance scuff resistance. Lyo et al. studied the effect of adding MoO_3 to Cr_2O_3 coatings on tribological properties (Lyo et al, 2003). To aim this goal, they fabricated MoO_3-Cr_2O_3 composite using a spray drying method. Lyo et al. demonstrated that using Cr_2O_3-MoO_3 composite coatings reduces the friction and wear of the counterpart material (Lyo et al, 2003).
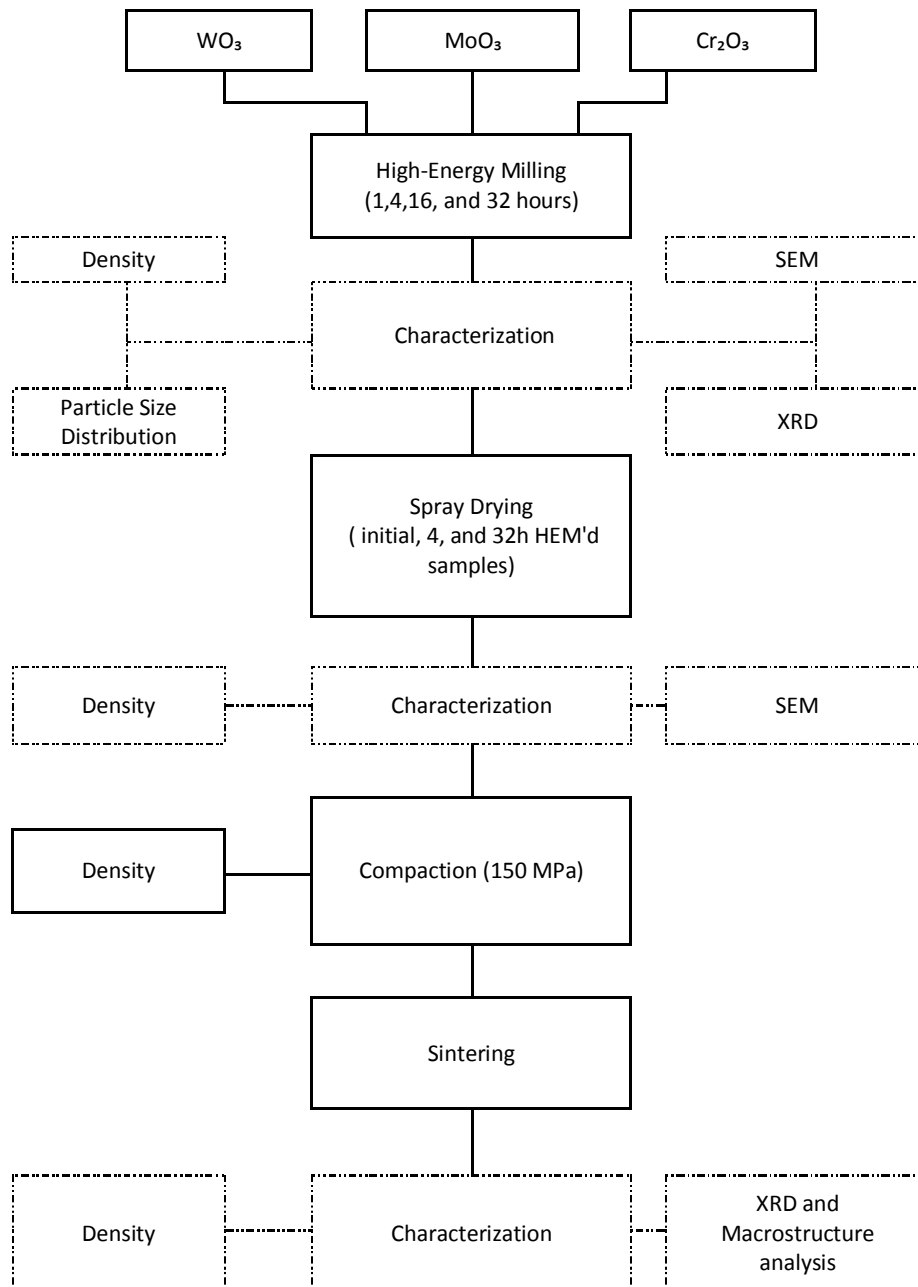
5. EXPERIMENTAL PROCEDURE

WO_3, MoO_3, and Cr_2O_3 powders were high energy milled (HEM'd) separately for 1, 4, 16, and 32 hours. The selected colloidal suspensions were then spray dried (SD'd), compacted and sintered at 750 °C, 400 °C and 1200 °C respectively. The effects of dispersant agent, high energy milling duration on the microstructure properties, effect of spray drying on compaction process and final product were investigated. Microstructural and phase characterizations were performed via particle size, XRD, and SEM analyses. Furthermore, density measurements of HEM'd samples, SD'd samples and sintered samples were carried out. The experimental procedure of the study is summarized in the flowchart presented in Figure 5.1.

5.1 Preparation of Samples

5.1.1 High energy ball milling

In this study, WO_3 (99.8% purity, Alfa Aesar™), MoO_3 (99.5% purity, Alfa Aesar™) and, Cr_2O_3 (99% purity, Alfa Aesar™) powders were used. Colloidal suspensions with solid contents of 30 %wt WO_3, MoO_3 and Cr_2O_3 were prepared separately. Darvan® C-N (Ammonium Polymethacrylate, Vanderbilt Minerals) was used as the dispersant agent. Milling experiments were carried out using a Fritsch™ Pulverisette 5 Planetary ball mill (Figure 5.2) with a speed of 1200 rpm in a polymer vial with zirconia balls having a diameter of 5 mm. The balls-to-powder weight ratio (BPR) was 7:1. Each oxide was milled separately with different milling times of 1, 4, 16 and 32 hours. All milling experiments of the mixtures were conducted in wet conditions in distilled water.

Figure 5.1: The flowchart of the experimental procedure.

Figure 5.2: Fritsch™ Pulverisette 5 Planetary mill.

5.1.2 Spray drying

The initial powders and the WO_3, MoO_3 and Cr_2O_3 powder samples HEM'd for 4 and 32 hours were selected and then SD'd separately. 2 %wt PVA used as the binder during SD process. The Büchi ™ Mini Spray Dryer (B-290) was used during SD experiments. Büchi ™ Mini Spray Dryer (B-290) and Dehumidifier™ (B-296) are shown in Figure 5.3.

Figure 5.3: a) Büchi ™ Mini Spray Dryer (B-290) and **b)** Dehumidifier™ (B-296).

The parameters, which were used in spray drying process, are given in Table 5.1.

Table 5.1: Spray drying parameters used for samples.

	Inlet Temperature (°C)	Outlet Temperature (°C)	Pump	Aspirator %	Flow
MoO₃	200	93±1	10	100	5
WO₃	200	95±1	10	100	4
Cr₂O₃	200	99±1	10	100	5

5.1.3 Compaction

The HEM'd and SD'd powders were compacted by cold pressing in a tool-steel die at a pressure of 150 MPa into cylinder shaped green compacts with a diameter of $\approx$12.7 mm for 30 seconds by using a 10 tons MSE™ uni-action hydraulic press. Figure 5.4 shows the picture of the MSE™ hydraulic press. Zinc stearate was applied onto the walls of the die in order to take the samples out of the die easily.

Figure 5.4: MSE™ uni-action hydraulic press.

5.1.4 Sintering

As shown in figure 5.5, sintering was performed in Protherm™ Standard Chamber furnaces, which are used to heat a material up to 1700 °C, to provide uniform sintering process by heating elements on the two sides of the furnace. Compacted HEM'd and SD'd MoO_3, WO_3, and Cr_2O_3 were sintered in air at 400 °C, 750 °C, and 1200 °C respectively for 30 minutes. Sintering regime involved a heating/cooling rate of 2 °C/min.

Figure 5.5: Protherm™ Standard Chamber furnaces.

5.2 Characterization of Powder Mixtures and Sintered Samples

5.2.1 Particle size distribution

Particle size of initial powders was measured by using a Malvern Instruments^{TM} Mastersizer 2000 (Figure 5.6a). Particle size of HEM'd samples were analyzed by using a Microtrac™ NANO-flex particle size analyzer (Figure 5.6b). Particle size analysis of SD'd samples could not be done because of the solubility of the dispersant agent in aqueous systems and disintegrating the granules. Particle size distributions were carried out by using distilled water. Before analyzing particle sizes, samples were held in a Bandelin™ Sonopuls for approximately 30 seconds to inhibit agglomeration and homogenize the suspension (Figure 5.7).

(a)   (b)

Figure 5.6: a) Malvern Instruments^{TM} Mastersizer 2000 and **b)** Microtrac™ Nano-flex particle size analyzer.

Figure 5.7: Bandelin™ Sonopuls HD 2200.

5.2.2 Phase characterizations

Initial powders, HEM'd, and sintered samples were characterized by X-ray diffraction (XRD) analysis. Phase characterizations of these samples were carried out using 40 kV and 40 mA Cu Kα conditions on a Bruker™ D8 Advance type X-ray diffractometer (Figure 5.8).

Figure 5.8: Bruker™ D8 Advanced type X-ray diffractometer.

5.2.3 Density measurements

5.2.3.1 Density measurements of the initial, HEM'd, and SD'd samples

Apparent density of initial powders, HEM'd, and SD'd samples were measured using Arnold apparent density meter (Figure 5.9) and true density of these samples were carried out using a Micromeritics™ AccuPyc® II 1340 Pycnometer (Figure 5.10).

Figure 5.9: Arnold apparent density meter.

Figure 5.10: Micromeritics™ AccuPyc® II 1340 Pycnometer.

5.2.3.2 Density measurements of the sintered samples

Densities of green compacts were calculated geometrically, which is ratio of mass to volume of specimens. Density measurements of sintered samples were carried out using Archimedes' method based on liquid displacement. In this method, the sample is firstly weighed in air and then in a liquid. The weights in air and in liquid were measured by using a Precisa™ XB220A Precision Balance (Figure 5.11). After that, the mass in air was divided to the difference of these results and then multiplied with the density of the liquid. Distilled water and ethanol were used as the liquid media.

Figure 5.11: Precisa™ XB220A Precision Balance.

5.2.4 Microstructural Characterization

Microstructural characterization investigations of initial powders, HEM'd, and SD'd samples were conducted using a JEOL™ Neoscope JSM 6000 scanning electron microscope (SEM) in a Secondary Electron Imaging (SEI) mode. JEOL™ Neoscope JSM 6000 scanning electron microscope is shown in figure 5.12.

5.2.5. Macrostructural characterization

The macrostructures of sintered samples were analyzed using a Zeiss™ Stereomicroscope (Figure 5.13).

Figure 5.12: JEOL™ Neoscope JSM 6000 scanning electron microscope (SEM).

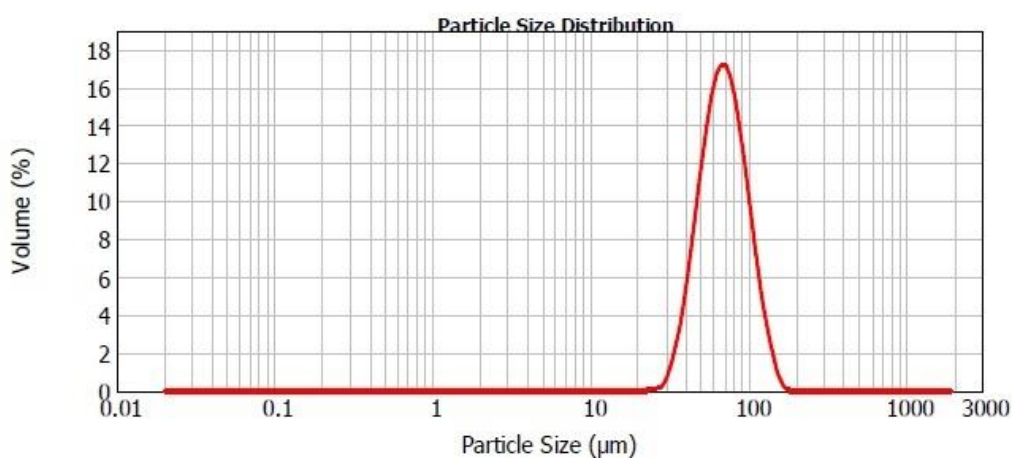**Figure 5.13:** Zeiss™ StereoMicroscope.

6. RESULTS AND DISCUSSION

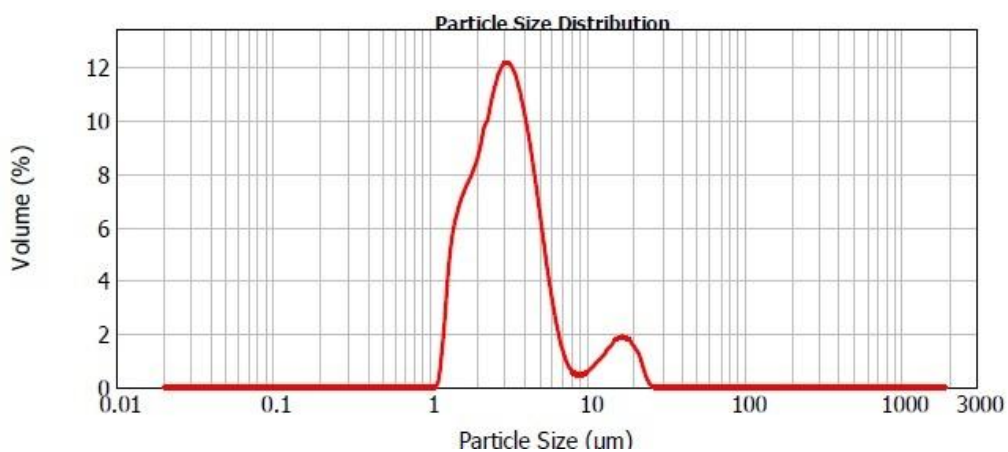## 6.1 Characterization of Initial and HEM'd Samples

6.1.1 Particle size distribution

Figure 6.1 and Table 6.1 show the respective particle sizes analysis of initial MoO_3, Cr_2O_3 and WO_3 powders, which have an average diameter of 73.3 µm, 4.2 µm and 71.5 µm, respectively.
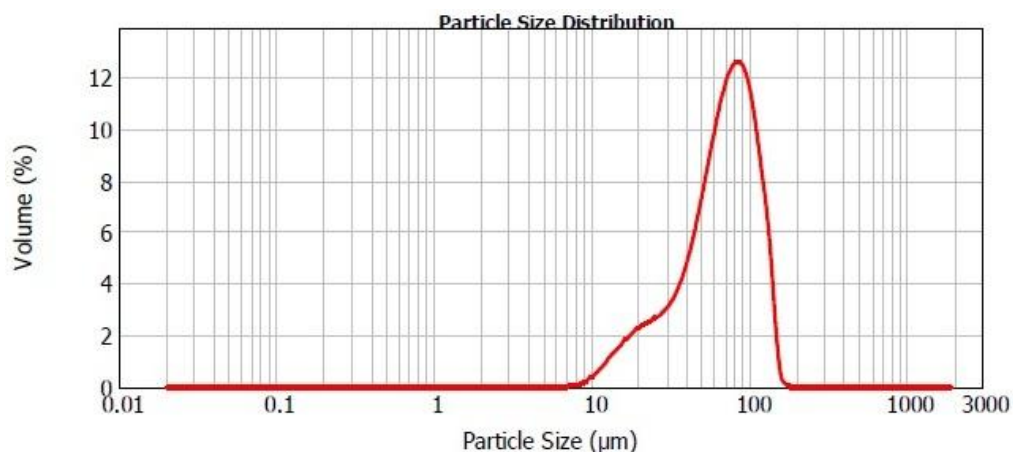

(a)

(b)

Figure 6.1: Particle size distributions of initial powders: a) MoO_3, b) Cr_2O_3 and c) WO_3.

(c)
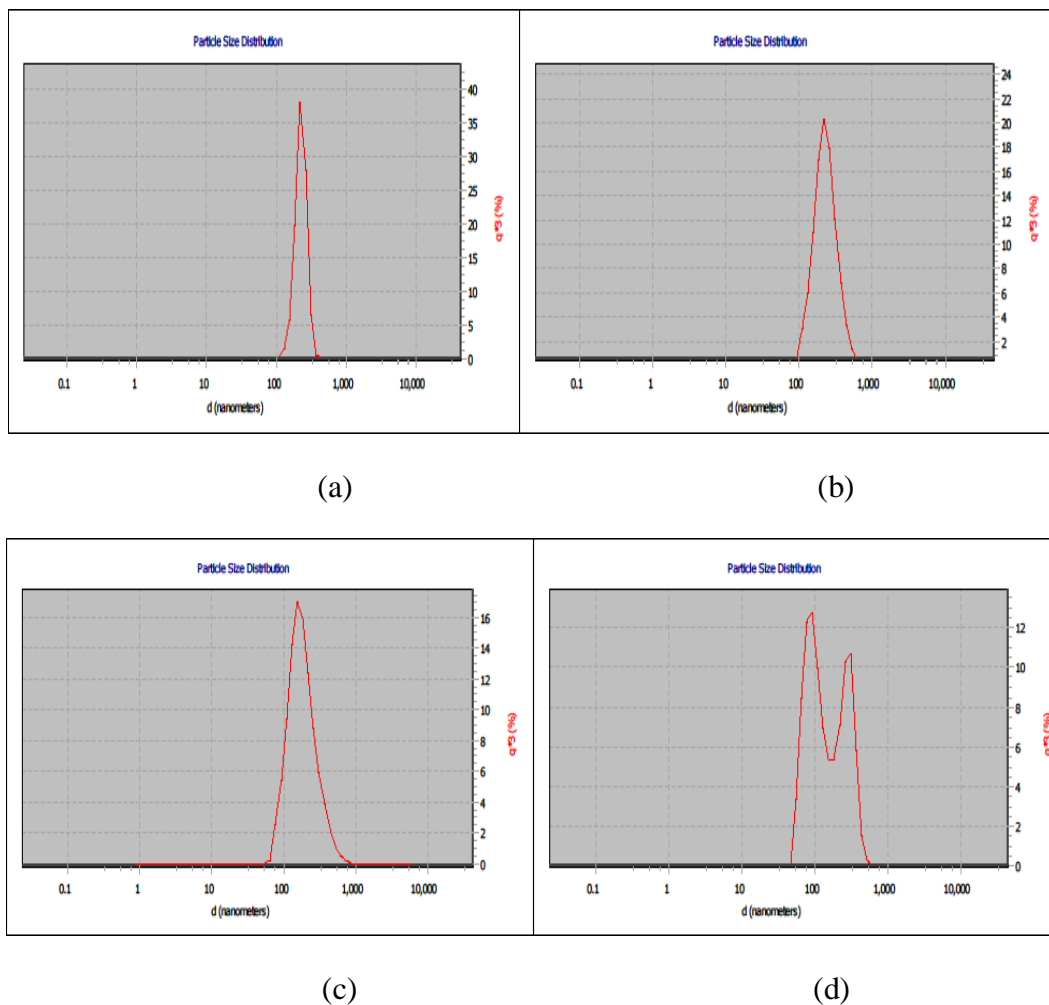
Figure 6.1 (Continued): Particle size distributions of initial powders: a) MoO_3, b) Cr_2O_3 and c) WO_3.

Table 6.1: Particle size data of the initial powders.

	MoO₃	*Cr₂O₃*	*WO₃*
D_{10} (µm)	44.7	1.6	25.3
D_{50} (µm)	69.3	3.1	70.2
D_{90} (µm)	107.6	6.4	118.1
Average (µm)	73.3	4.2	71.5

Figure 6.2 shows the particle size distribution of HEM'd MoO_3 samples subjected to different milling times of 1, 4, 16, and 32 hours in distilled water and without any dispersant agent.

Figure 6.2 a-d and Table 6.2 show the evaluation of particle size distributions of MoO_3 samples during high-energy milling. As seen in Figure 6.2, the average particle size of MoO_3 powders decreased with increasing milling times. After milling for 32h, the average particle size decreased from 73.3 µm to 174 nm.

38

(a)   (b)

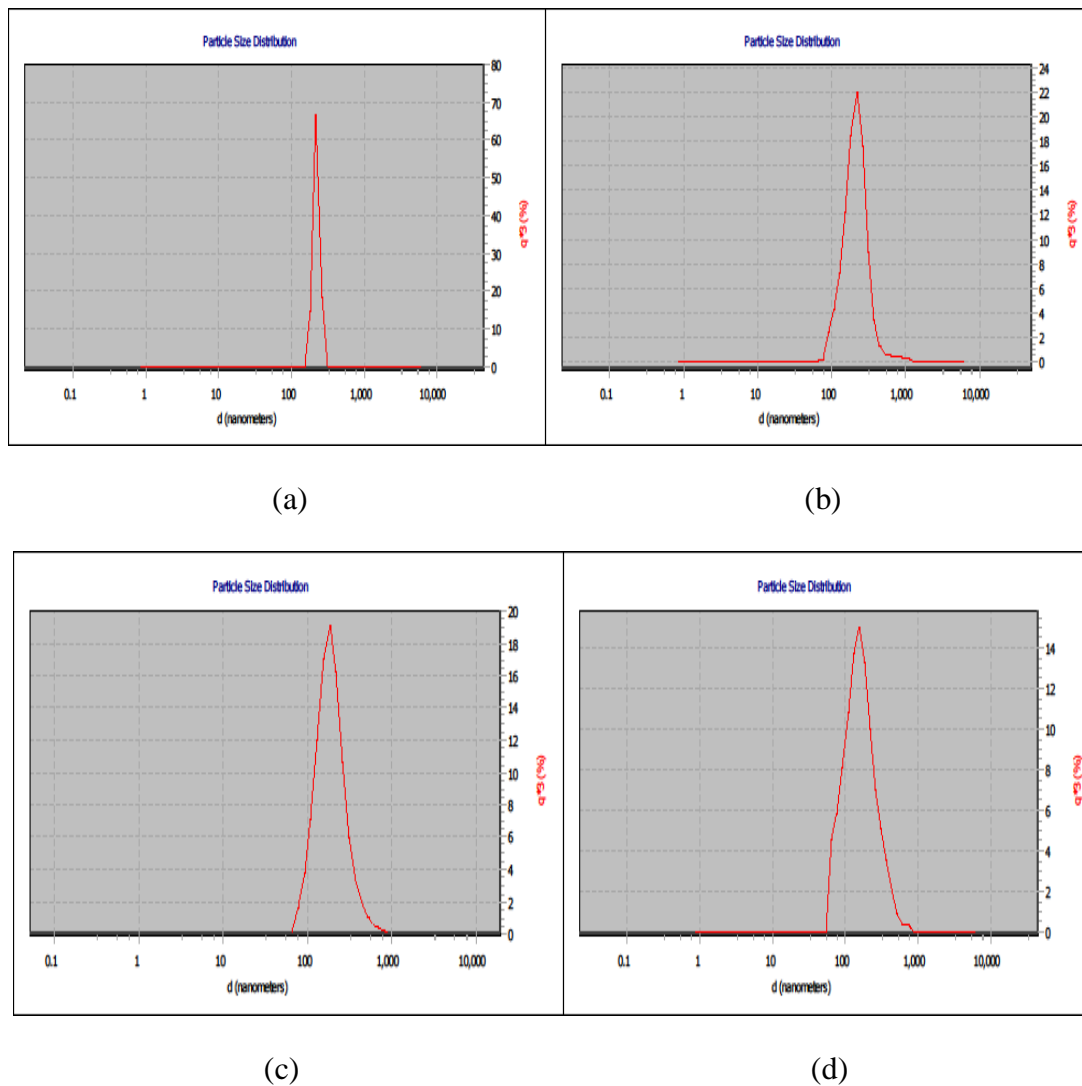(c)   (d)

Figure 6.2: Particle size distributions of HEM'd MoO$_3$ powders with different milling times of: a) 1 hour, b) 4 hours, c) 16 hours, and d) 32 hours.

Table 6.2: Particle size data of HEM'd MoO$_3$.

	1 hour	*4 hours*	*16 hours*	*32 hours*
D$_{10}$ (nm)	178.2	145.0	106.3	70.1
D$_{50}$ (nm)	227.5	227.2	173.9	130.8
D$_{90}$ (nm)	281.5	359	322.0	328.0
Average (nm)	229.0	242.8	198.3	174.0

1.5% wt Darvan C-N was used to study the effect of adding dispersant on particle size distribution. Figure 6.3 shows the particle size distributions of HEM'd MoO$_3$ samples with 1.5% wt Darvan C-N.

(a)　　　　　　　　　　　　　　　　(b)

(c)　　　　　　　　　　　　　　　　(d)

Figure 6.3: Particle size distributions of HEM'd MoO_3+Darvan C samples with different milling times of: a) 1 hour, b) 4 hours, c) 16 hours and, d) 32 hours.

As shown in the Table 6.3, After 32 hours of milling the average particle size of MoO_3+Darvan C powders decreased from 225.3 nm to 180.9 nm.

Table 6.3: Particle size data of HEM'd MoO_3+Darvan C.

	1 hour	*4 hours*	*16 hours*	*32 hours*
D_{10} (nm)	199.1	132.9	115.5	85.1
D_{50} (nm)	224.1	213.2	185.7	157.1
D_{90} (nm)	253.3	317.0	308.0	309.0
Average (nm)	225.3	227.7	203.6	180.9

As seen in the Figure 6.4 and Figure 6.5, with the addition of 1.5 %wt Darvan C to MoO₃, the agglomeration behavior of 32 hours HEM'd powder seems to be reduced.
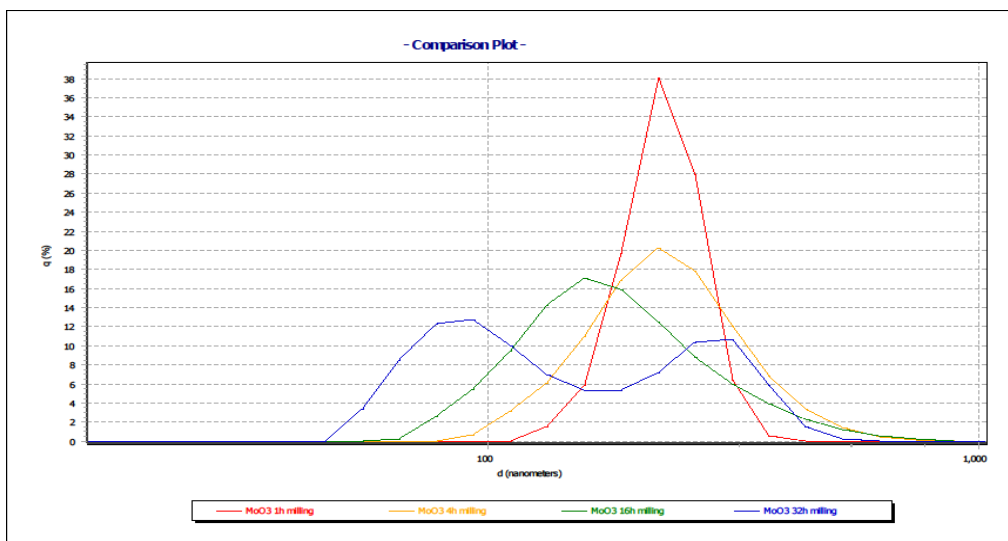
Figure 6.4: Comparative plots of particle size distributions of HEM'd MoO₃ samples milled for 1, 4, 16, and 32 hours.
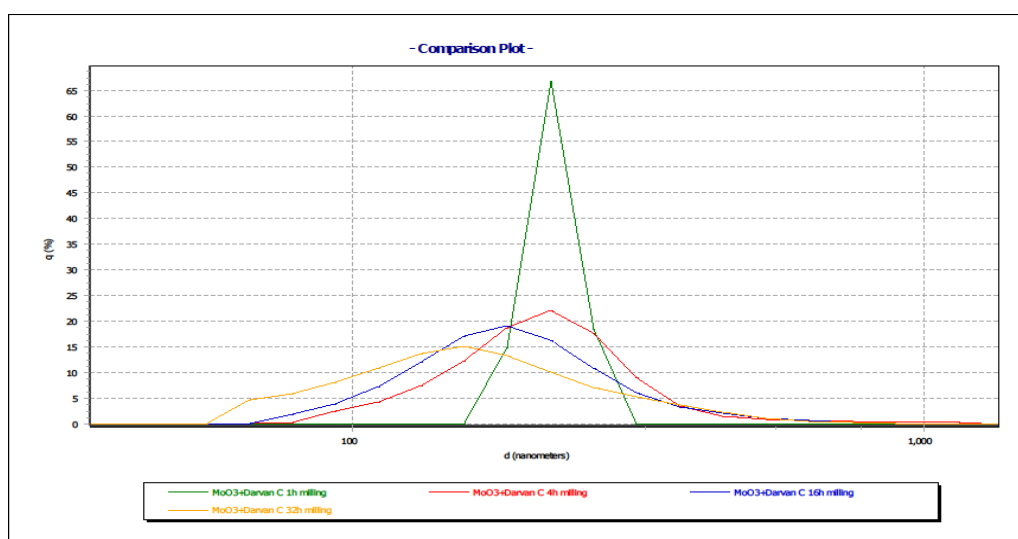
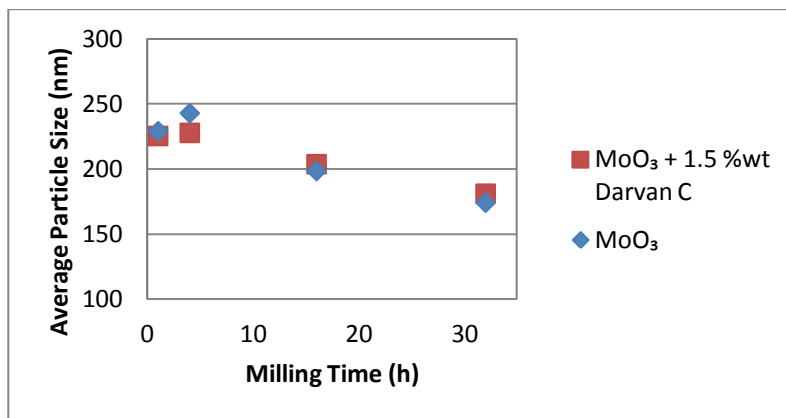**Figure 6.5:** Comparative plots of particle size distributions of HEM'd MoO₃+Darvan C samples milled for 1, 4, 16, and 32 hours.

Figure 6.6 shows the effect of adding dispersant on the average particle size of HEM'd MoO₃ samples.

Figure 6.6: Effect of adding Darvan C on the average particle sizes of HEM'd MoO$_3$ samples.

Figure 6.6 reveals that the average particle sizes of HEM'd MoO$_3$ samples are not changed by the addition of Darvan C as dispersant.

The same experiment was done using WO$_3$ and Cr$_2$O$_3$ powders. Figure 6.7 shows the particle size distributions of Cr$_2$O$_3$ samples at different milling times.

(a)

(b)

(c)

(d)
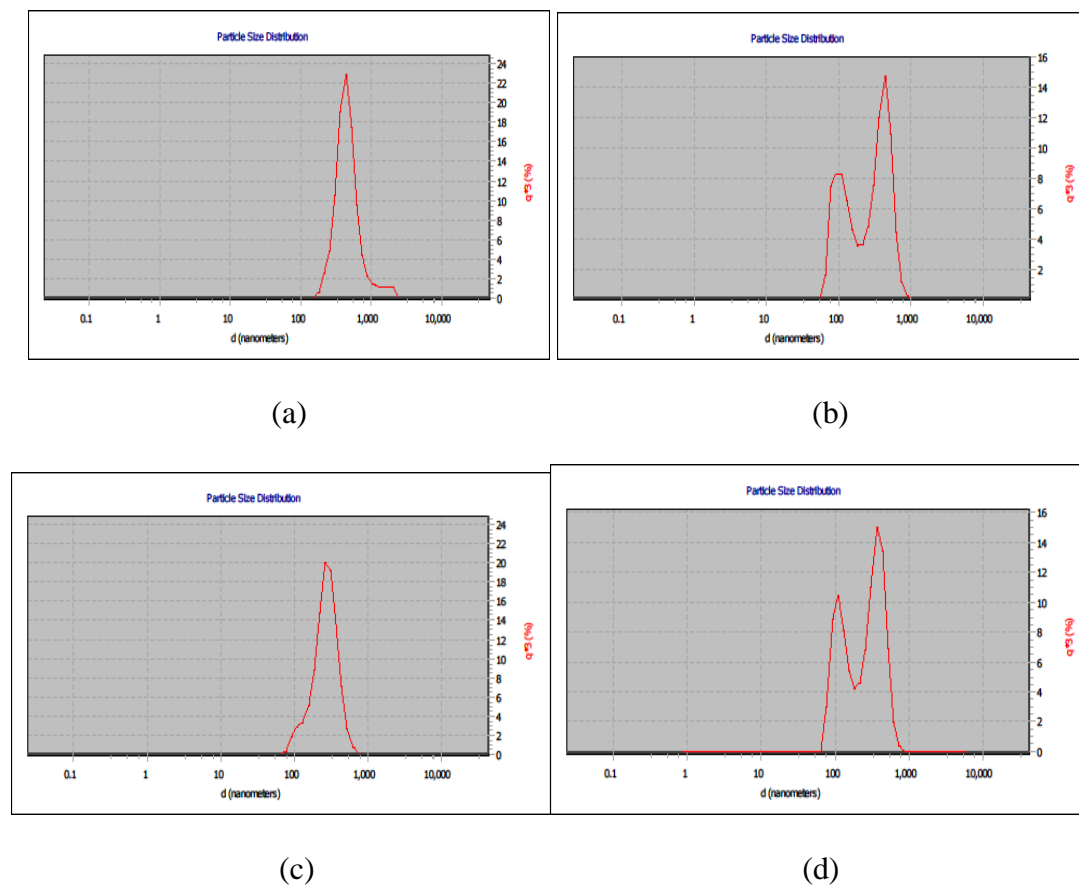
Figure 6.7: Particle size distributions of HEM'd Cr$_2$O$_3$ samples milled for different times of: a) 1 hour, b) 4 hours, c) 16 hours, and d) 32 hours.

Figure 6.7 and Table 6.4 show the variation in the particle size distributions of Cr_2O_3 powders with high-energy milling. As seen in the Table 6.4, the average particle size decreased after 32 hours milling from 4.2 μm to 279.3 nm.

Table 6.4: Particle size data of HEM'd Cr_2O_3.

	1 hour	4 hours	16 hours	32 hours
D_{10} (nm)	303.0	87.4	155.6	99.1
D_{50} (nm)	449.0	298.6	273.1	280.6
D_{90} (nm)	754.0	536.0	413.0	480.0
Average (nm)	524.0	299.1	281.2	279.3

Figure 6.8 and Table 6.5 show the particle size distributions of Cr_2O_3+Darvan C samples at different milling times.

(a)   (b)

(c)   (d)

Figure 6.8: Particle size distributions of HEM'd Cr_2O_3+Darvan C samples milled for different times of: a) 1 hour, b) 4 hours, c) 16 hours, and d) 32 hours.
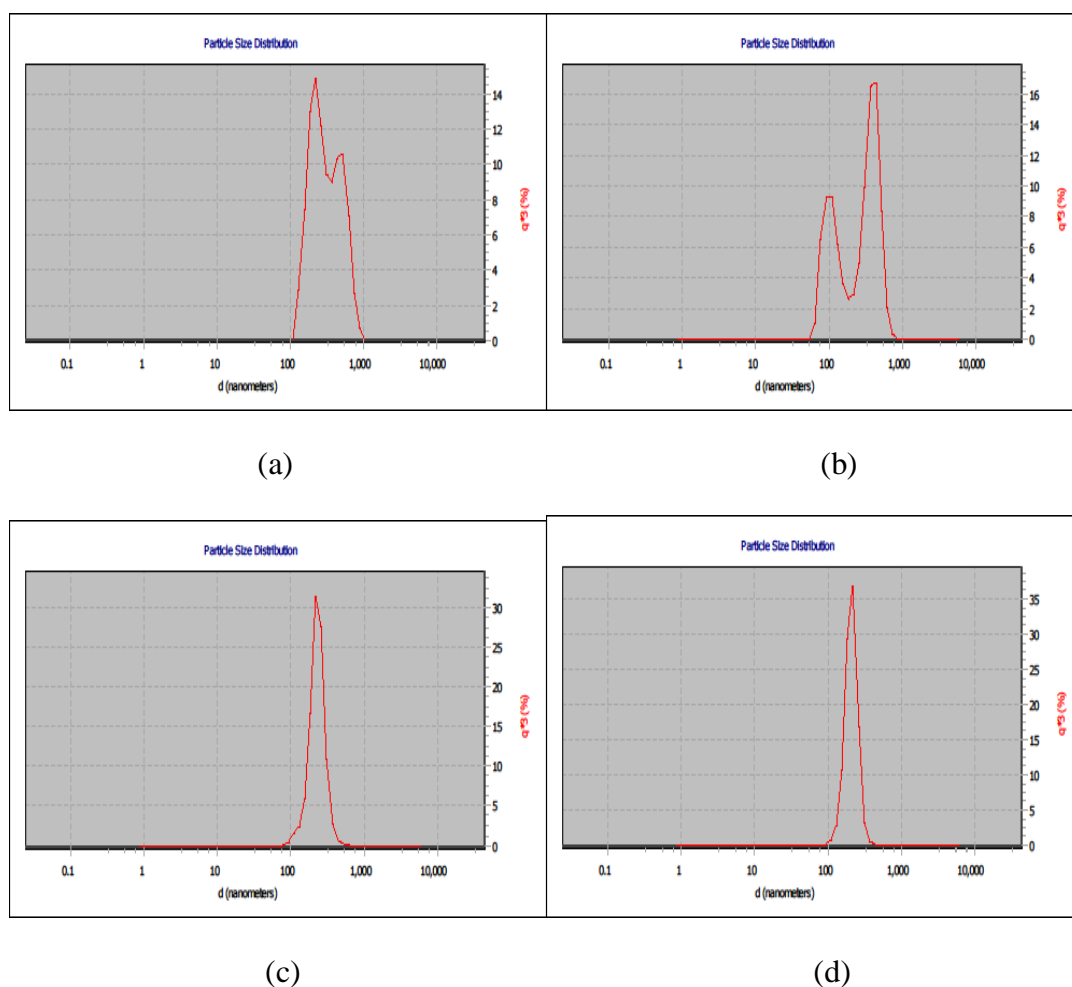
Table 6.5: Particle size data of HEM'd Cr_2O_3+Darvan C.

	1 hour	*4 hours*	*16 hours*	*32 hours*
D_{10} (nm)	171.1	90.3	171.0	165.1
D_{50} (nm)	287.8	313.0	232.8	210.9
D_{90} (nm)	584.0	491.0	302.0	263.9
Average (nm)	341.0	289.4	235.8	212.9

As Figure 6.8 shows, with the addition of 1.5 %wt Darvan C, the particle size distribution became narrower for 16 and 32 hours. The average particle size of Cr_2O_3+Darvan C samples decreased from 341 nm to 212.9 nm.

Figure 6.9 and Figure 6.10 show the comparative plots of particle size distributions of the HEM'd Cr_2O_3 samples milled for different times.
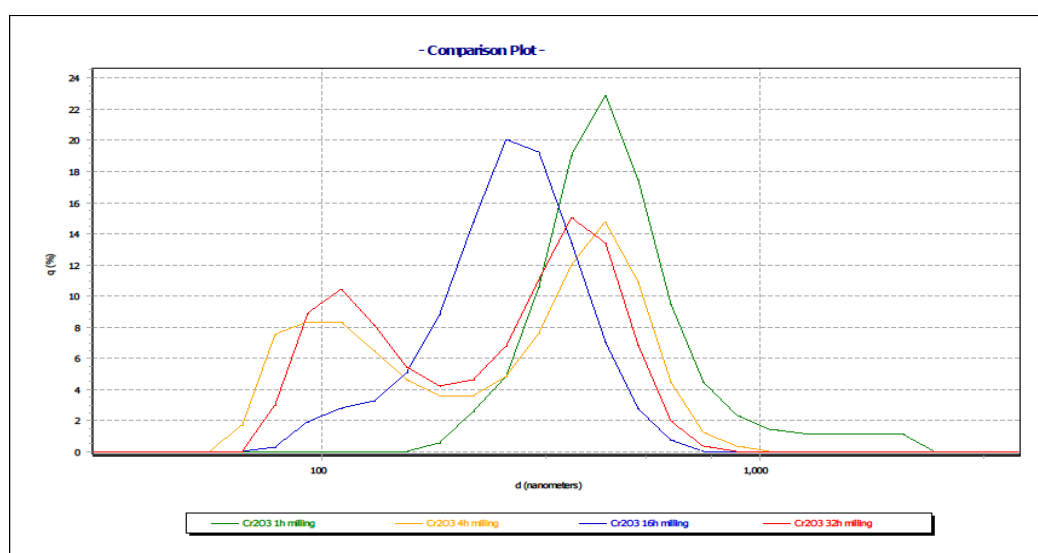
Figure 6.9: Comparative plots of particle size distributions of the HEM'd Cr_2O_3 samples milled for 1, 4, 16, and 32 hours.
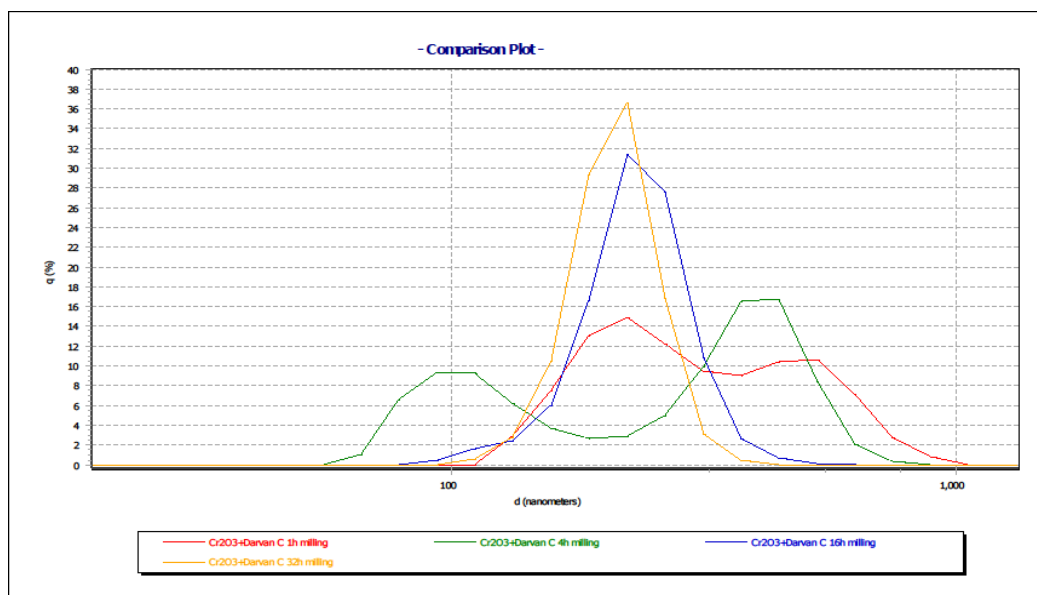
Figure 6.10: Comparative plots of particle size distributions of the HEM'd Cr$_2$O$_3$+Darvan C samples milled for 1, 4, 16, and 32 hours.

Figure 6.11 shows the effect of adding Darvan C on the average particle size of HEM'd Cr$_2$O$_3$ samples.
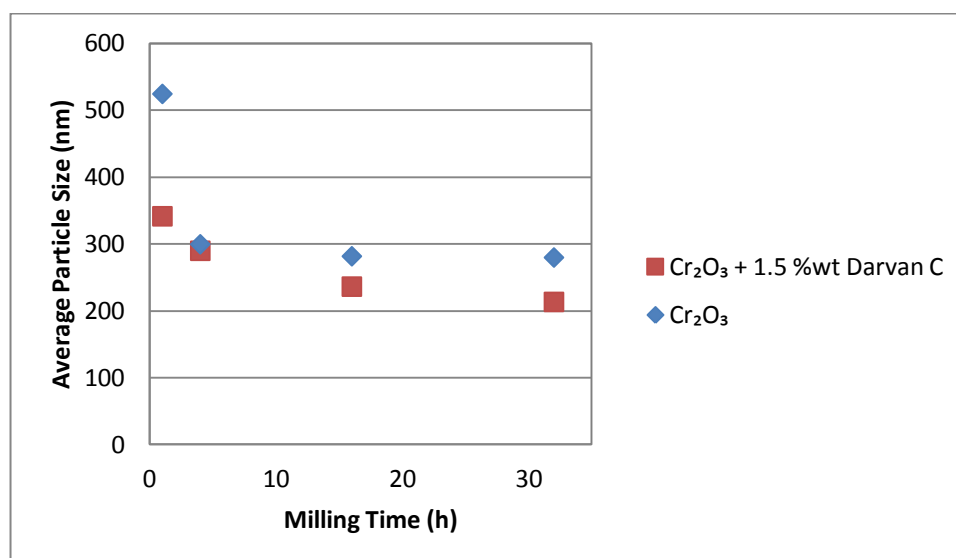
Figure 6.11: Effect of adding Darvan C on the average particle sizes of the HEM'd Cr$_2$O$_3$ samples.

It can be illustrated from the particle size analysis of Cr$_2$O$_3$ samples that, adding Darvan C helps to inhibit agglomeration during milling.
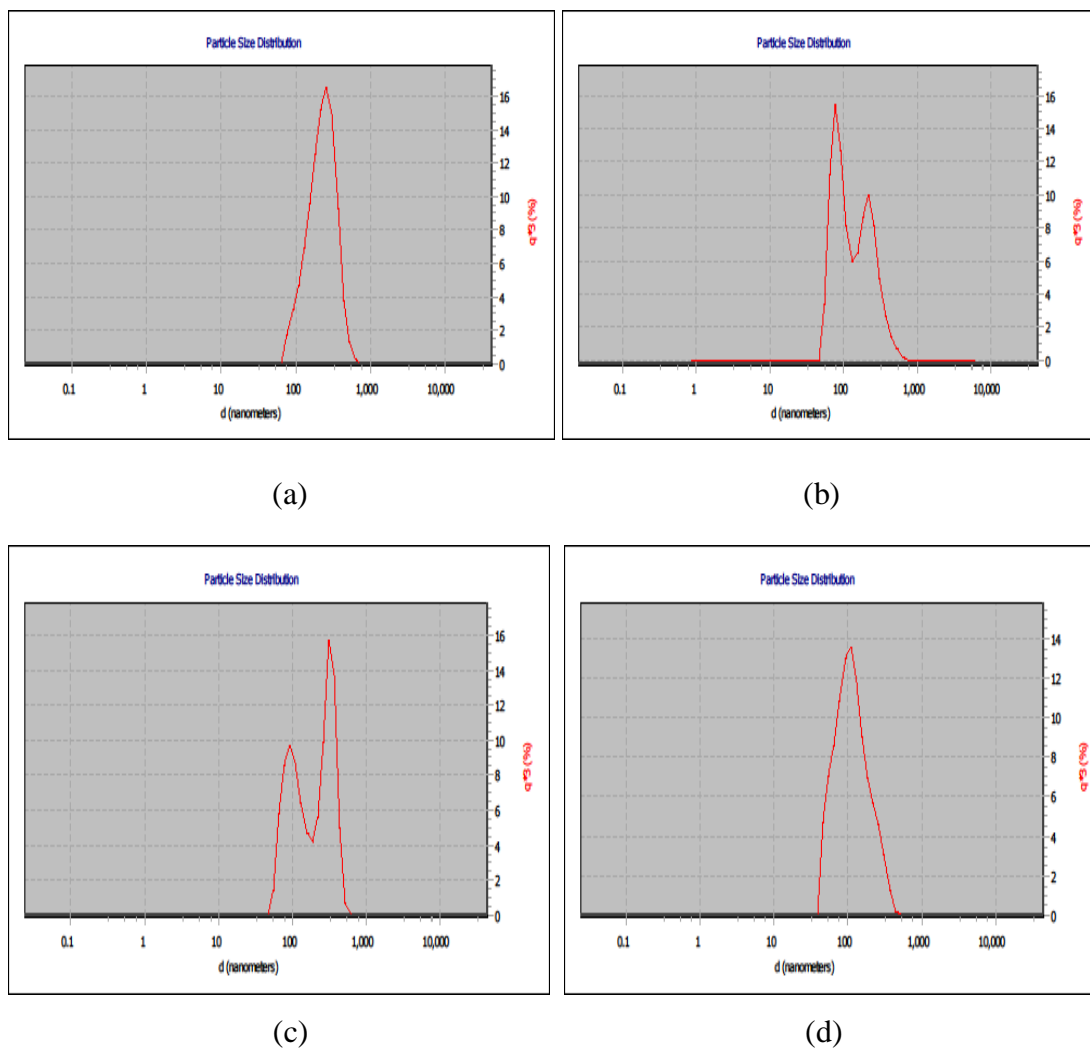
Figure 6.12 and Table 6.6 show the particle size distributions of WO_3 samples milled for 1, 4, 16, and 32 hours. It can be illustrated that, there is a decreasing in average particle size with increasing milling time up to 32 hours. The average particle sizes after 32 hours milling reduced from 71.5 µm to 130.1 nm. Figure 6.12 b and c show agglomeration behavior in the WO_3 powders.

(a)   (b)

(c)   (d)

Figure 6.12: Particle size distributions of HEM'd WO_3 samples milled at different times of: a) 1 hour, b) 4 hours, c) 16 hours, and d) 32 hours.

Figure 6.13 and Table 6.7 show the particle size distributions of WO_3+Darvan C samples milled at different times.

Table 6.6: Particle size data of HEM'd WO_3.

	1 hour	*4 hours*	*16 hours*	*32 hours*
D_{10} **(nm)**	122.5	68.1	76.9	58.5
D_{50} **(nm)**	232.8	118.9	209.6	110.2
D_{90} **(nm)**	370.0	288.2	384.0	236.3
Average (nm)	242.0	157.2	219.4	130.1

(a)   (b)
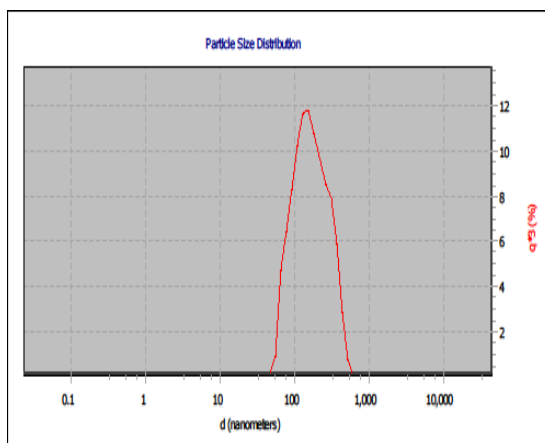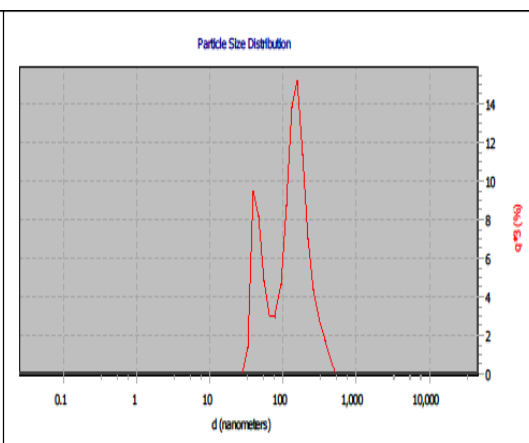
(c)   (d)
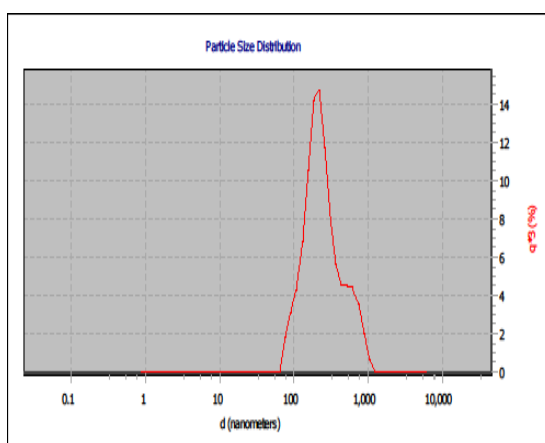
Figure 6.13: Particle size distributions of HEM'd WO_3+Darvan C samples milled for: a) 1 hour, b) 4 hours, c) 16 hours, and d) 32 hours.

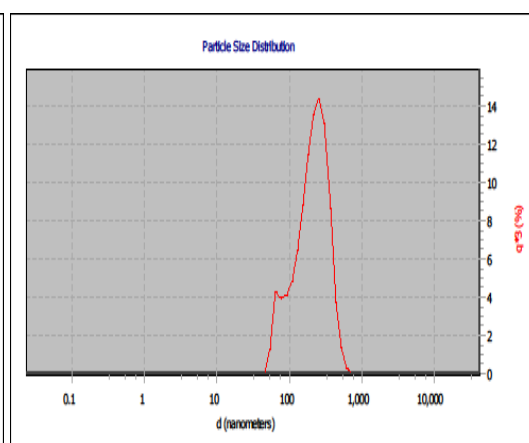**Table 6.7:** Particle size data of HEM'd WO_3+Darvan C.

	1 hour	*4 hours*	*16 hours*	*32 hours*
D_{10} **(nm)**	125.0	87.8	81.9	42.4
D_{50} **(nm)**	228.1	218.3	162.2	133.4
D_{90} **(nm)**	589.0	368.0	339.0	241.0
Average (nm)	292.7	226.8	188.9	138.3

With the addition of dispersant to the samples, the average particle size decreased from 292.7 nm to 138.3 nm.

Figure 6.14 and Figure 6.15 show the comparative plots of particle size distributions of the HEM'd WO_3 samples milled for different times.
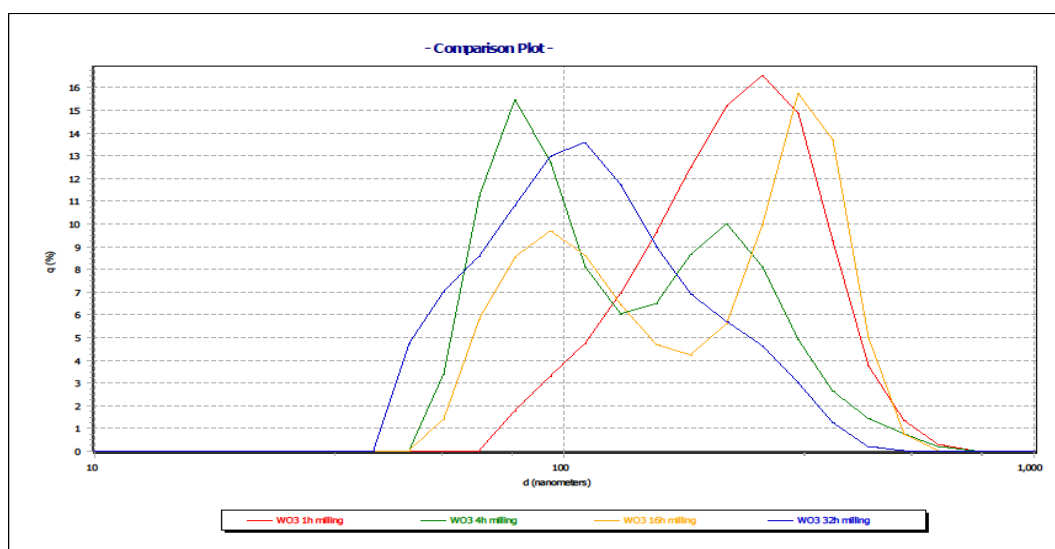
Figure 6.14: Comparative plots of particle size distributions of HEM'd WO_3 samples milled for 1, 4, 16, and 32 hours.
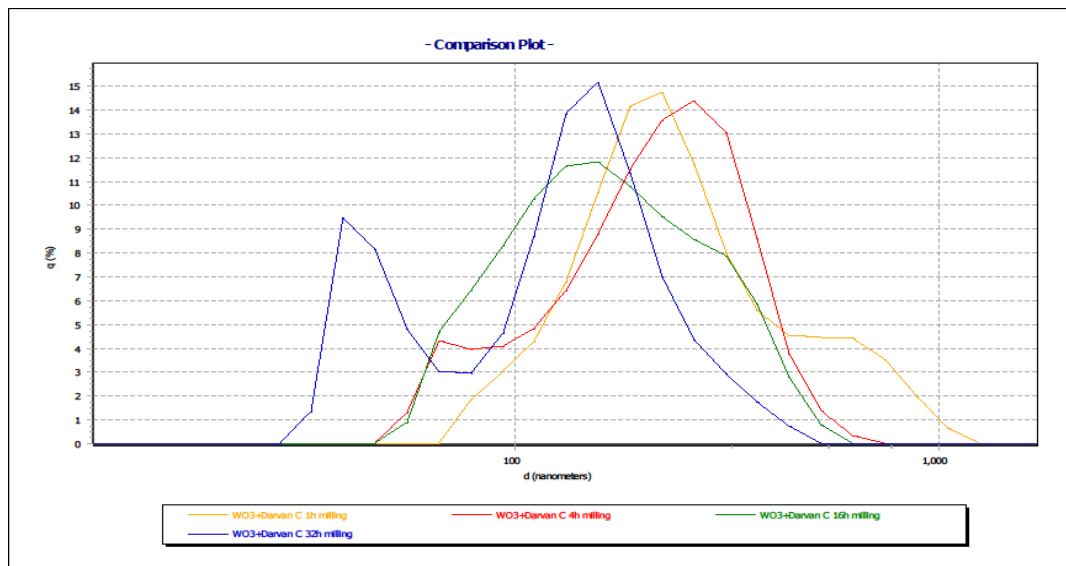
Figure 6.15: Comparative plots of particle size distributions of HEM'd WO$_3$+Darvan C samples milled for 1, 4, 16, and 32 hours.

The effect of the addition of Darvan C on the average particle sizes of WO$_3$ samples is given in figure 6.16.
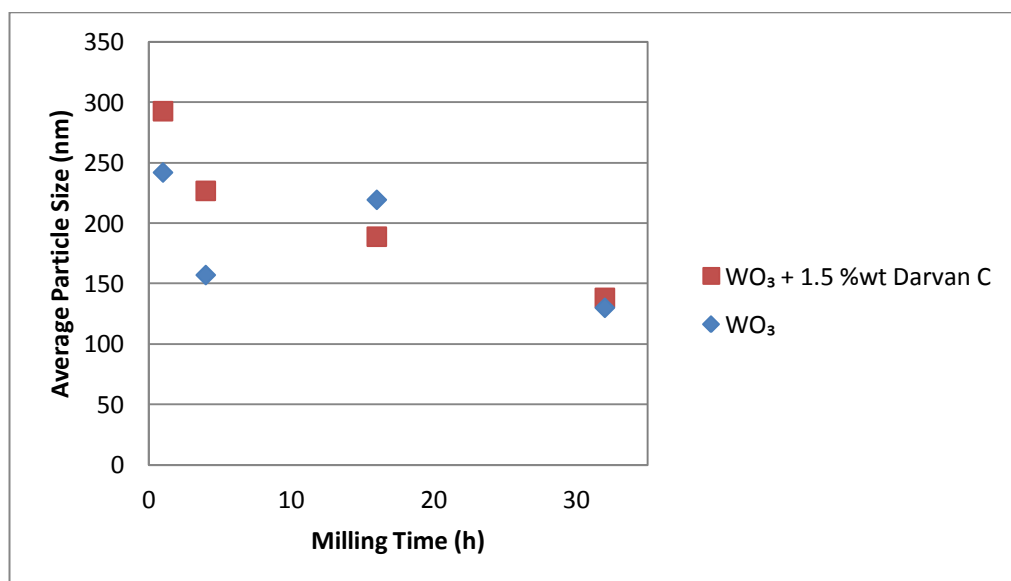
Figure 6.16: Effect of adding Darvan C on the average particle sizes of HEM'd WO$_3$ samples.

6.1.2 Density measurements

Density measurements for HEM'd MoO_3 samples at different milling times are given in table 6.8.

Table 6.8: Density measurements of MoO_3 samples HEM'd for different times.

Milling Time (hour)	Darvan C (%)	Apparent Density (g/cm^3)	True Density (g/cm^3)
0	_	1.309±0.137	4.670±0.007
1	_	1.189±0.076	4.719±0.008
4	_	1.108±0.031	4.758±0.003
16	_	1.223±0.111	4.618±0.002
32	_	1.143±0.012	4.742±0.001
1	1.5	1.201±0.019	4.724±0.006
4	1.5	1.138±0.015	4.785±0.003
16	1.5	1.052±0.018	4.711±0.003
32	1.5	0.992±0.013	4.826±0.013

The apparent density values of HEM'd MoO_3 powders are given in Figure 6.17. These values indicate the compaction behavior of the powders. As seen in the Figure 6.17 increasing the milling time causes a decrease in apparent density values. This means with further milling MoO_3 powders exhibit less packing behavior.
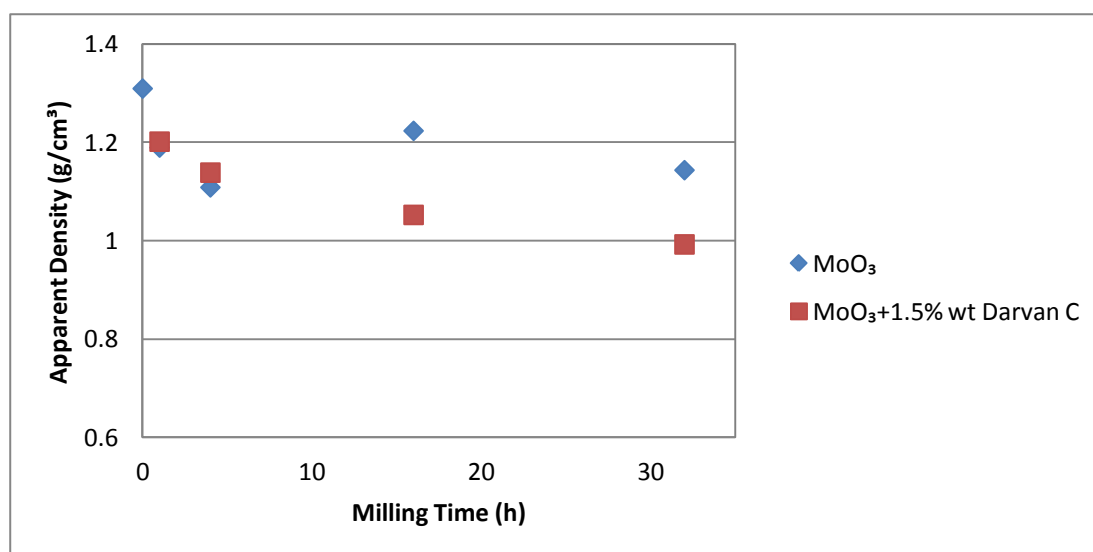
Figure 6.17: Apparent density values of MoO_3 samples at different milling times.

Figure 6.18 shows the true density values of MoO_3 samples at different milling times.

Figure 6.18: True density values of MoO_3 samples at different milling times.

Density measurements for WO_3 samples at different milling times are listed in Table 6.9.

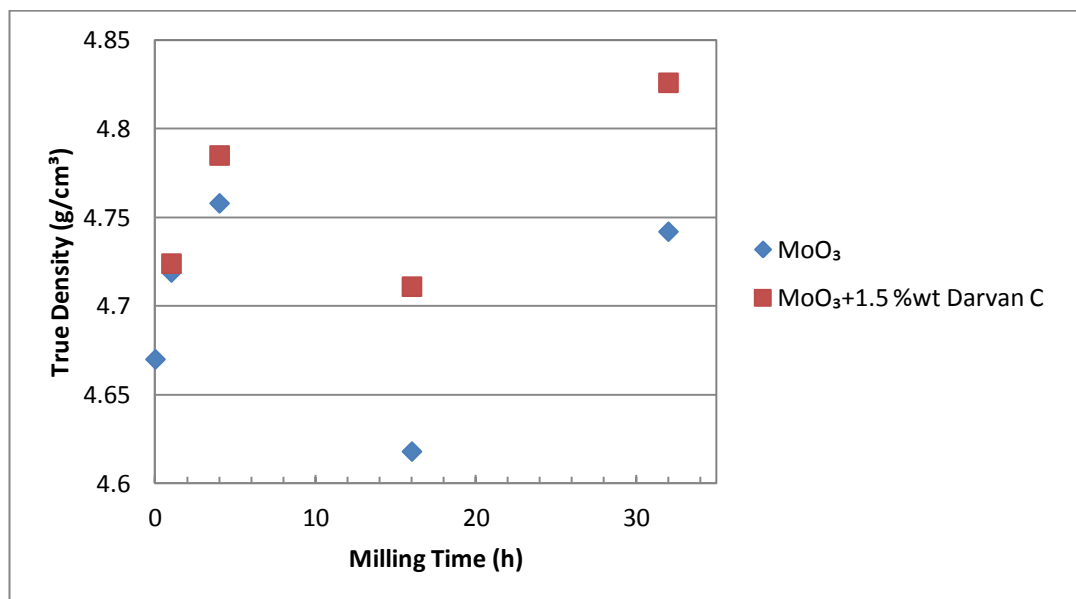**Table 6.9:** Density measurements of WO_3 samples HEM'd for different times.

Milling Time (h)	Darvan C (%)	Apparent Density (g/cm^3)	True Density (g/cm^3)
0	_	3.182±0.027	7.307±0.007
1	_	1.984±0.019	7.362±0.003
4	_	1.807±0.039	7.221±0.002
16	_	1.709±0.030	6.997±0.002
32	_	1.844±0.056	6.870±0.006
1	**1.5**	2.169±0.024	7.188±0.005
4	**1.5**	2.113±0.026	7.045±0.002
16	**1.5**	2.109±0.026	7.013±0.073
32	**1.5**	2.067±0.019	6.767±0.048

Figure 6.19 shows the apparent density values of WO_3 samples at different milling times.

Figure 6.19: Apparent density values of WO$_3$ samples at different milling times.

As shown in Figure 6.19, the apparent density of HEM'd WO$_3$ shows a sharp decrease after passing 1 hour.

True density values of HEM'd WO$_3$ samples as a function of milling times are given in Figure 6.20.
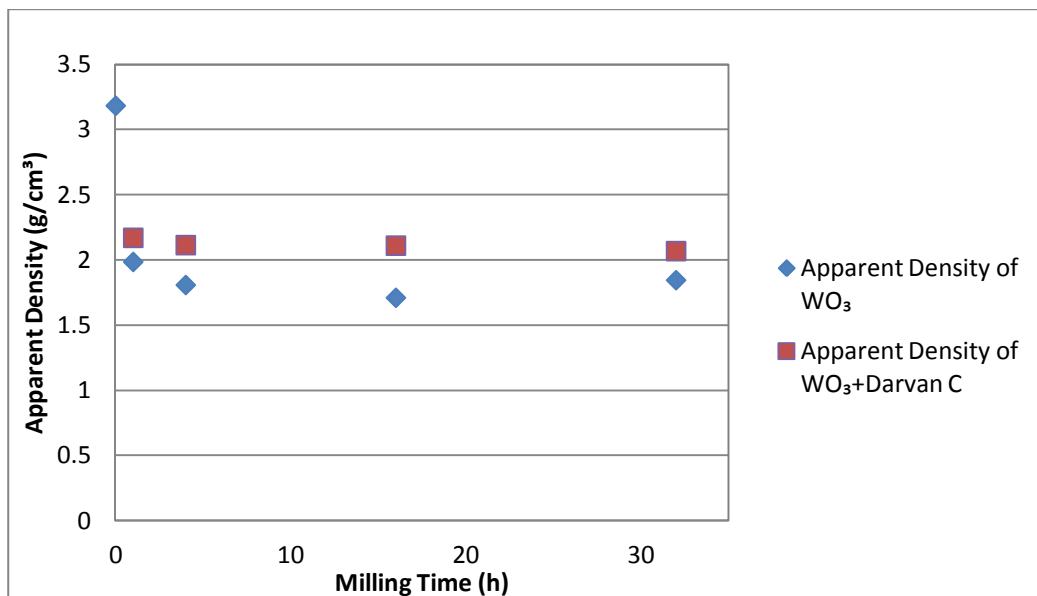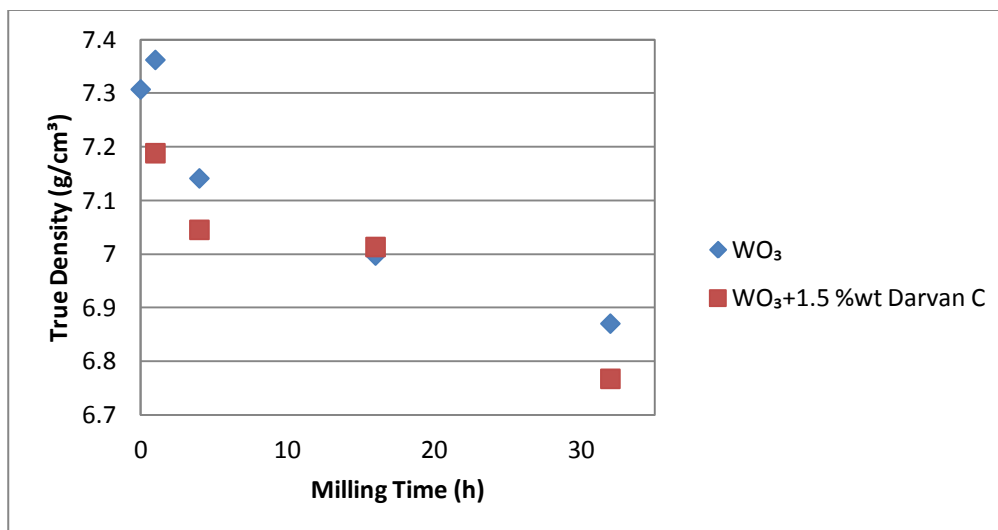

Figure 6.20: True density values of WO$_3$ samples at different milling times.

Density measurements for Cr$_2$O$_3$ samples at different milling times are given in table 6.10.

Table 6.10: Density measurements of Cr_2O_3 samples HEM'd for different times.

Milling Time (h)	Darvan C (%)	Apparent Density (g/cm^3)	True Density (g/cm^3)
0	–	0.576±0.063	5.167±0.004
1	–	0.952±0.020	5.214±0.009
4	–	1.057±0.040	5.151±0.009
16	–	1.025±0.024	5.009±0.004
32	–	1.006±0.005	5.249±0.009
1	1.5	1.014±0.015	5.202±0.005
4	1.5	1.243±0.024	5.184±0.004
16	1.5	1.203±0.014	5.215±0.004
32	1.5	1.165±0.014	5.295±0.006

Figure 6.21 shows the changes in apparent density against milling time for Cr_2O_3 samples. Apparent density values of HEM'd Cr_2O_3 powders increases after milling for 1 hour. There is a slight reduction in apparent density with further milling up to 32 hours.
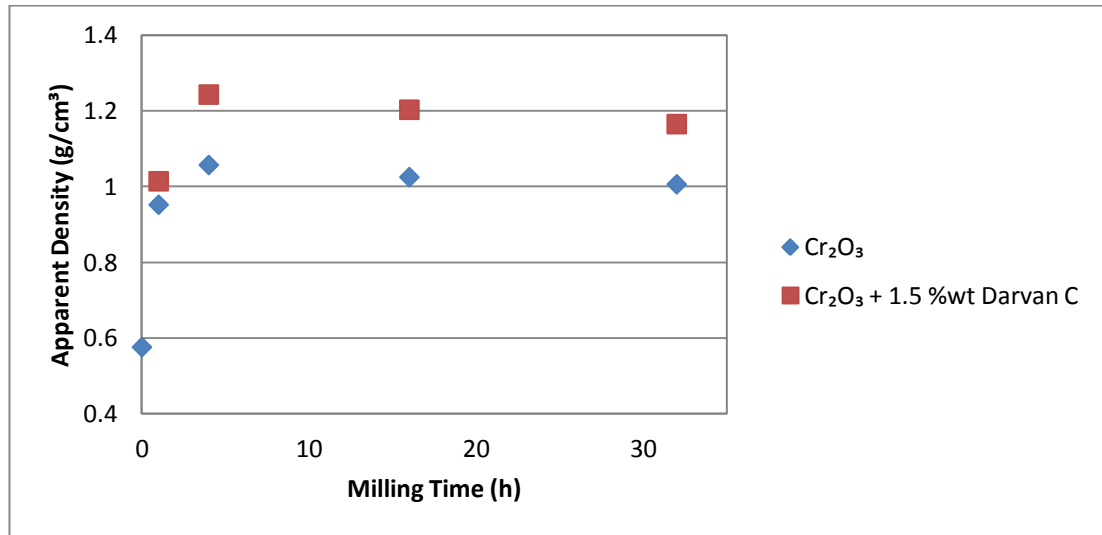
Figure 6.21: Apparent density values of Cr_2O_3 samples milled for different times.

Figure 6.22 shows the true density values of Cr_2O_3 samples milled for different times
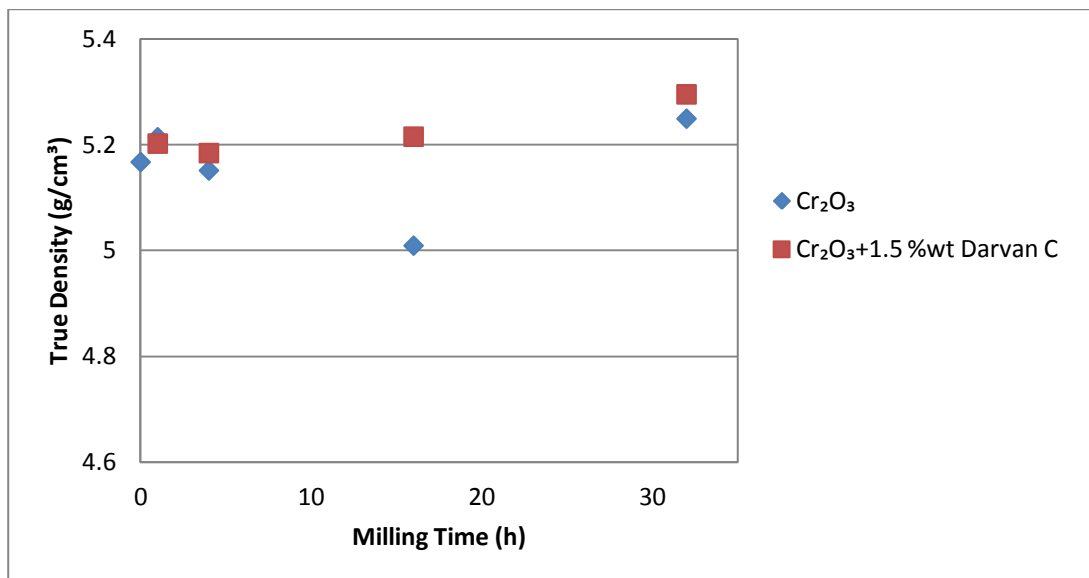
Figure 6.22: True density values of Cr_2O_3 samples milled for different times.

6.1.3 Phase analysis and microstructural characterizations

Figure 6.23 shows the XRD patterns of MoO_3 samples with different HEM'd duration. As seen in all patterns of Figure 6.23, only the peaks of MoO_3 which has an orthorhombic Bravais lattice with the lattice parameters of a=3.963 nm, b=13.855 nm, and c=3.696 nm (PDF No: 01-076-1003) can be identified, Indicating the fact that any phases, other than the orthorhombic MoO_3, did not form during HEM up to 32h.
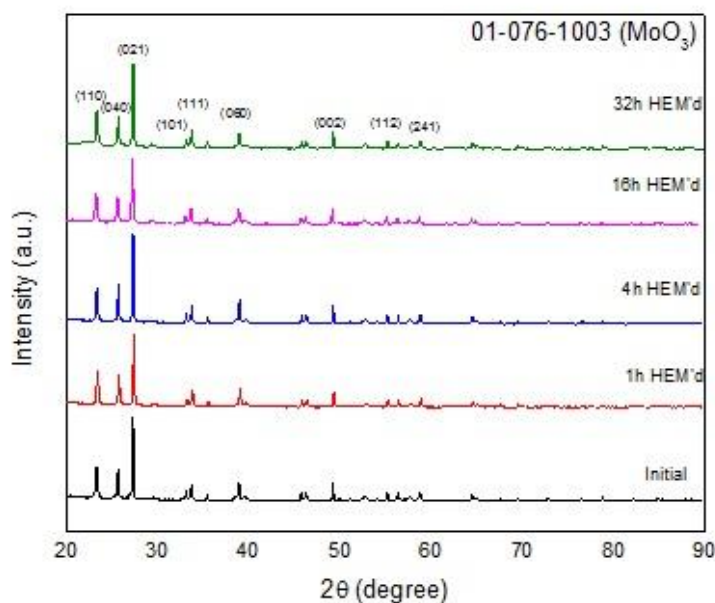
Figure 6.23: XRD patterns of the initial and HEM'd MoO_3 samples.

The XRD patterns of WO_3 samples with different HEM durations are shown in Figure 6.24. As seen in all patterns of Figure 6.24, only the peaks of WO_3 which has a monoclinic Bravais lattice with the lattice parameters of a=7.301 nm, b=5.389 nm, and c=7.689 nm (PDF No: 01-083-0950) can be identified. Again, similar to Figure 6.23, only the monoclinic WO_3 phase existed during HEM with no presence of a new phase in the microstructure.
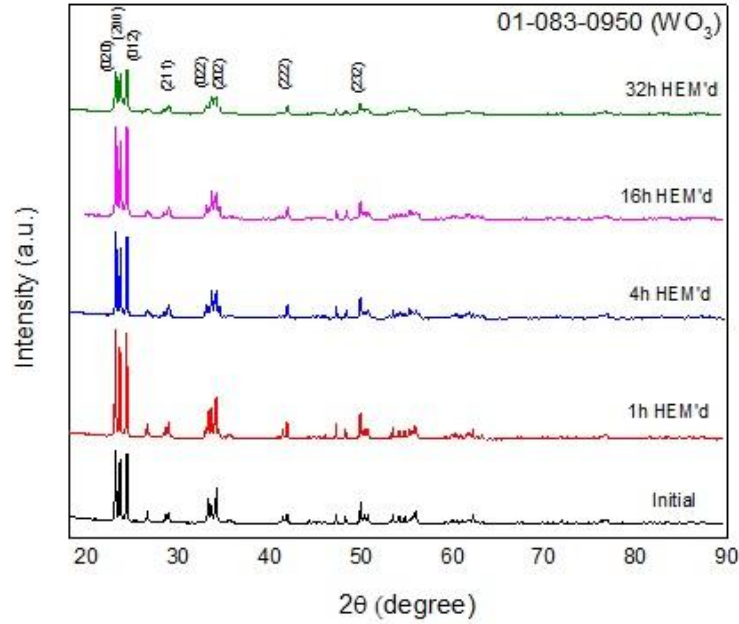
Figure 6.24: XRD patterns of the initial and HEM'd WO_3 samples.

XRD patterns of the initial and HEM'd Cr_2O_3 samples are shown in Figure 6.25. The peaks of Cr_2O_3, which has a rhombohedral Bravais lattice with the lattice parameters of a=4.953 nm and c=13.578 nm (PDF No: 01-072-3533) can be identified in all samples, which means no new phase formation took place during HEM of the rhombohedral Cr_2O_3.

Figure 6.26 shows the SEM micrographs of the initial WO_3 powder and those HEM'd for 4, 16, and 32 hours. As can be seen from this figure, initial particle sizes of WO_3 were continuously decreased with increasing HEM. Figure 6.26 b-d shows particles varying in size between 100 nm and 200 nm. Local agglomerations, which are clearly seen in Figure 6.26 b and c, occur due to small particle size distribution of the HEM'd WO_3 samples.
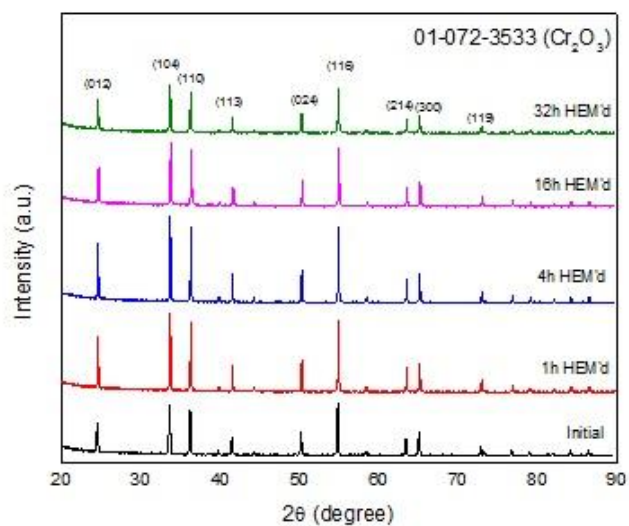
Figure 6.25: XRD pattern of the initial and HEM'd Cr_2O_3 samples.

(a)

(b)

(c)

(d)
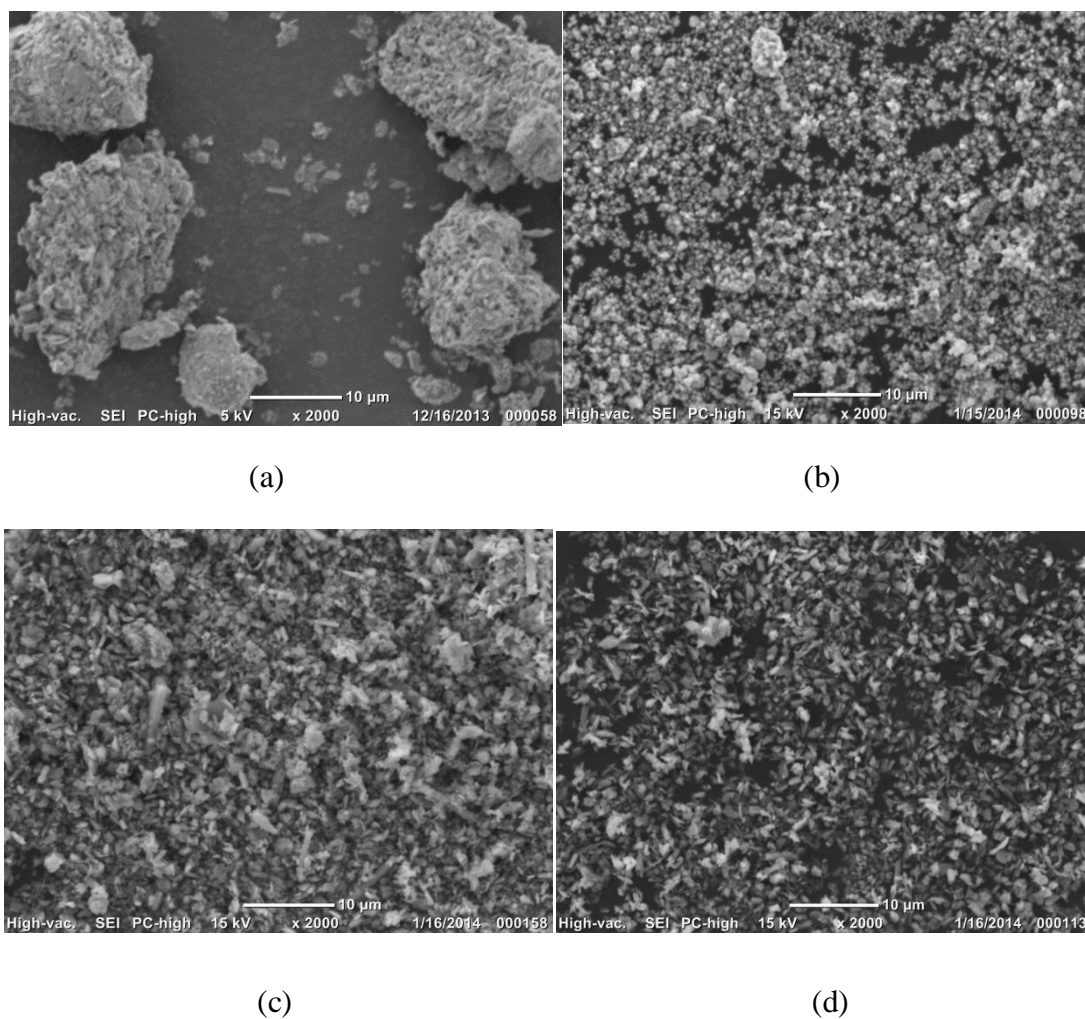
Figure 6.26: SEM images of: a) initial, b) 4h HEM'd, c) 16h HEM'd, and d) 32h HEM'd WO_3 samples.

Figure 6.27 shows the SEM micrographs of the initial MoO_3 powder and those HEM'd for 4, 16, and 32 hours. As can be seen in this figure, microscale initial MoO_3 powders have diameters in nanoscale after HEM. Initial MoO_3 particles are about 70 µm in size. Figure 6.27 b-d shows particles varying in size between 100 nm and 200 nm. Local agglomerations, which are clearly seen in Figure 6.26 b-d, occurred due to small particle size distribution of the HEM'd MoO_3 samples.

(a)   (b)

(c)   (d)
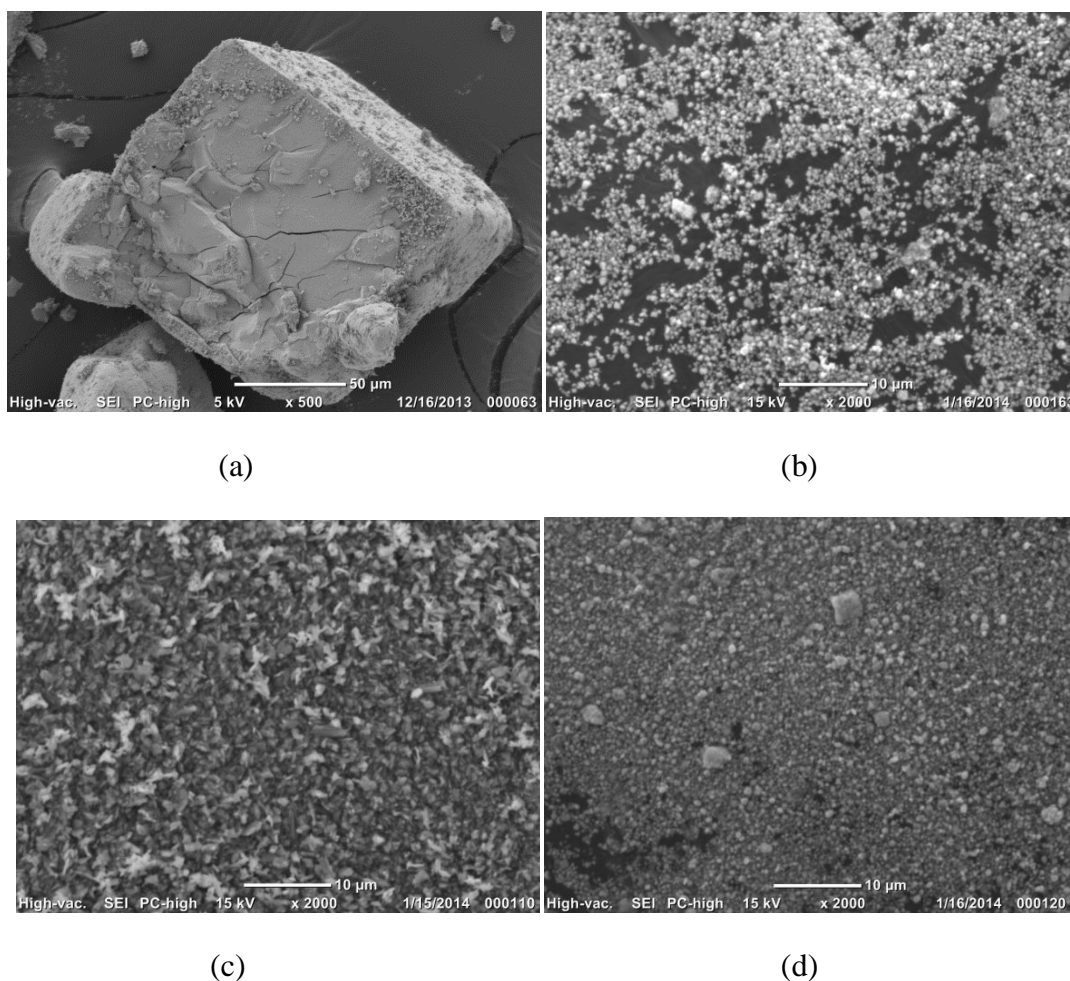
Figure 6.27: SEM images of: a) initial, b) 4h HEM'd, c) 16h HEM'd, and d) 32h HEM'd MoO_3 samples.

SEM micrographs of the initial Cr_2O_3 powder and effect of high energy milling up to 32 hours on this powder are given in Figure 6.28. Initial Cr_2O_3 particles are about 4 µm in size. Figure 6.28 b-d shows particles varying in size between 200 nm and 300 nm. In all Cr_2O_3 samples, local agglomerations occurred due to small particle size distribution.

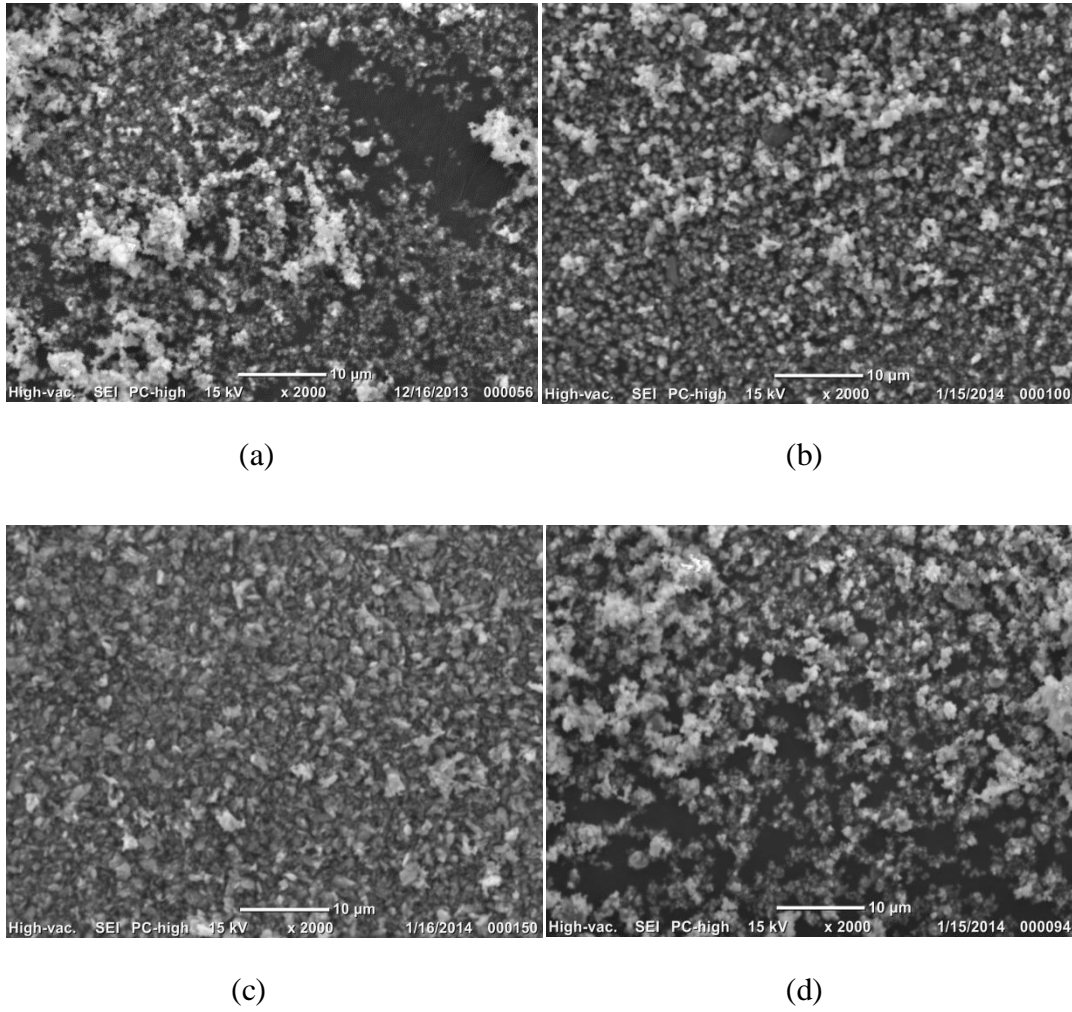(a)   (b)

(c)   (d)

Figure 6.28: SEM images of: a) initial, b) 4h HEM'd, c) 16h HEM'd, and d) 32h HEM'd Cr_2O_3 samples.

6.2 Characterization of SD'd Samples

6.2.1 Density measurements

Density measurements of SD'd MoO_3 samples are given in the Table 6.11.

Table 6.11: Density measurements of SD'd MoO_3 samples.

HEM Duration (h)	Apparent Density (g/cm^3)	True Density (g/cm^3)
Initial	0.832±0.021	4.616±0.004
4h HEM'd	0.644±0.012	5.394±0.132
32h HEM'd	0.512±0.016	4.570±0.021
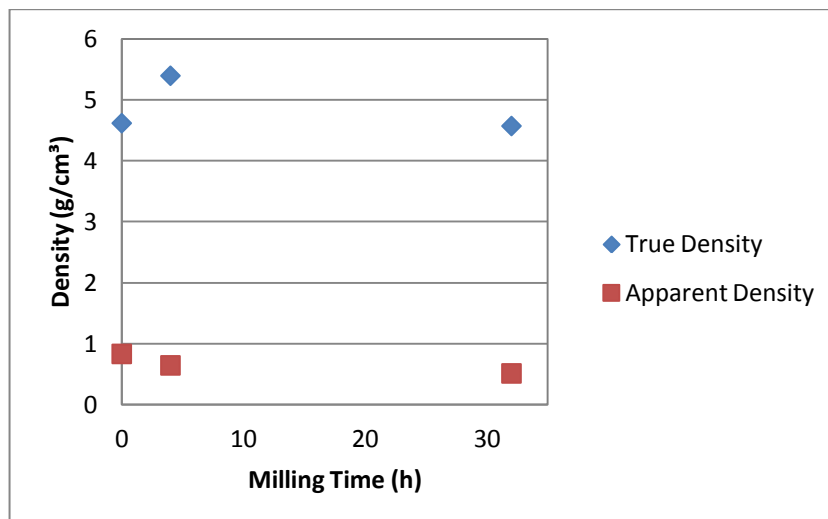
Figure 6.29: True density vs. Apparent density values of SD'd MoO_3 samples at different milling times.

Figure 6.29 shows the true density and apparent density values of SD'd MoO_3 samples. With increasing milling time, apparent density values of SD'd MoO_3 reduced slightly. On the other hand, the maximum true density value belongs to the 4h HEM'd MoO_3 powders.

Apparent density and true density values of SD'd WO_3 samples are given in Table 6.12 and Figure 6.30. The minimum value of apparent density and the maximum value of true density belong to the 4h HEM'd WO_3 powders.

Table 6.12: Density measurements of SD'd WO_3 samples.

HEM Duration (h)	Apparent Density (g/cm^3)	True Density (g/cm^3)
Initial	1.443 ± 0.013	6.719 ± 0.015
4h HEM'd	1.062 ± 0.022	7.081 ± 0.009
32h HEM'd	1.162 ± 0.025	6.573 ± 0.002
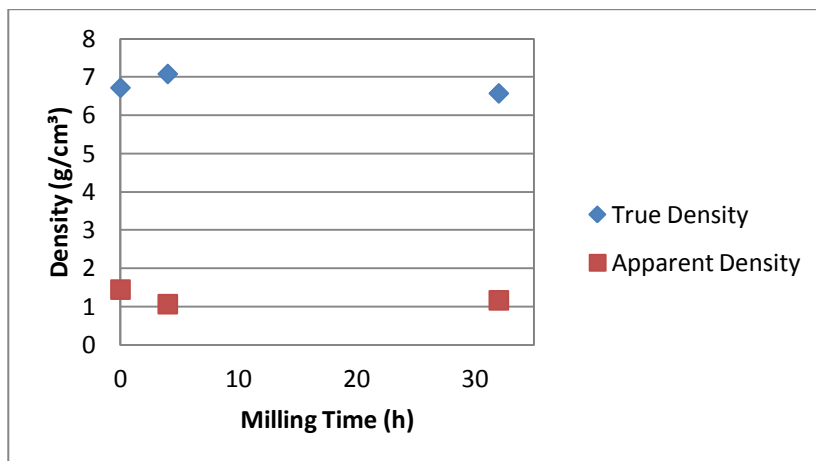
Figure 6.30: True density vs. Apparent density values of SD'd WO_3 samples at different milling times.

Figure 6.31 and Table 6.13 show the apparent density and true density measurements of SD'd Cr_2O_3 samples. Both true density and apparent density values of SD'd Cr_2O_3 samples declined steadily with increasing milling time.

Table 6.13: Density measurements of SD'd Cr_2O_3 samples.

HEM Duration (h)	Apparent Density (g/cm³)	True Density (g/cm³)
Initial	0.592±0.017	5.110±0.007
4h HEM'd	0.557±0.022	5.036±0.006
32h HEM'd	0.472±0.010	4.847±0.007
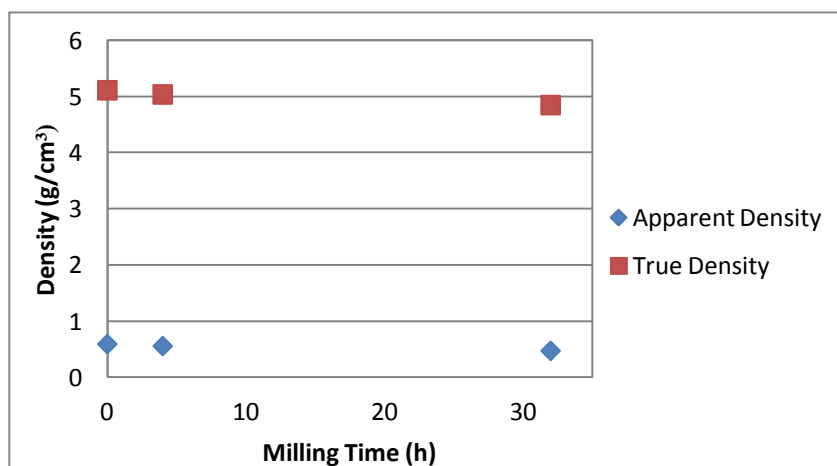
Figure 6.31: True density vs. Apparent density values of SD'd Cr_2O_3 samples at different milling times.

6.2.2 Microstructural characterizations

SEM micrographs of the SD'd initial WO_3 powders and those HEM'd for 4 and 32h are given in Figure 6.32. Spherical shaped particles can be seen in all SD'd WO_3 samples.

Figure 6.33 shows the 4 and 32h HEM'd Cr_2O_3 samples after spray drying. Spherical granules can be seen in both 4 and 32 h HEM'd Cr_2O_3. Local agglomerations of Cr_2O_3 particles can be seen in Figure 6.33 a.

SEM micrographs of SD'd MoO_3 samples which HEM'd for 4 and 32h are given in Figure 6.34. The hollow and doughnut shaped particles are clearly seen in SD'd MoO_3 samples.
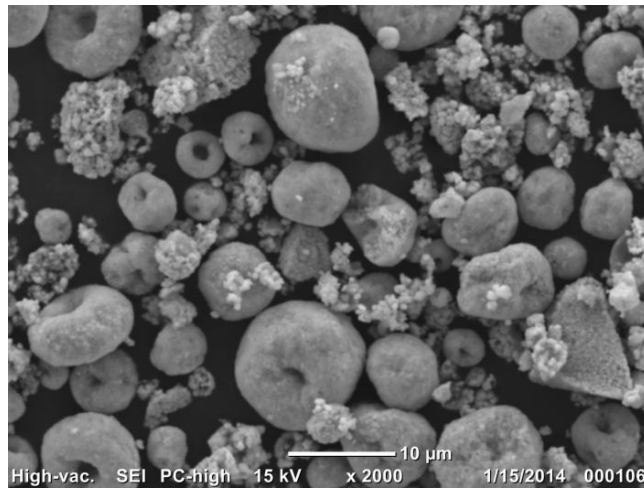
(a)
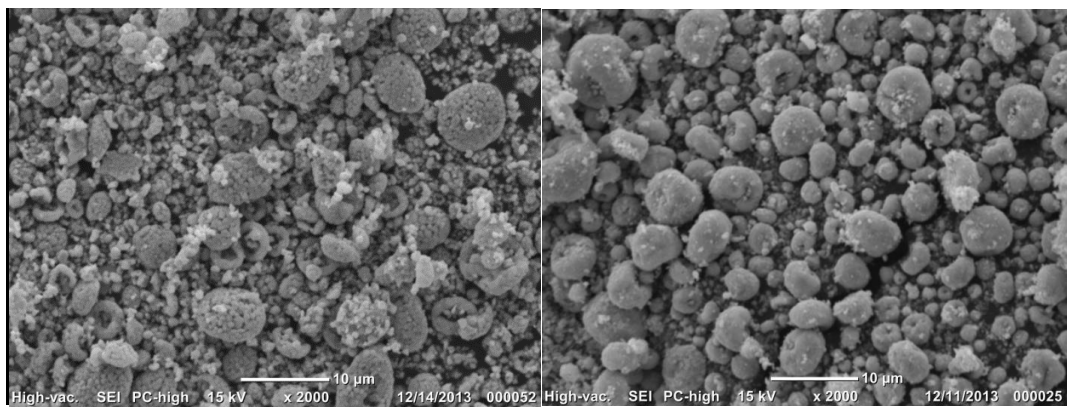
(b)   (c)

Figure 6.32: SEM micrographs of SD'd: a) initial, b) 4h HEM'd, and c) 32h HEM'd WO_3 samples.

(a)   (b)
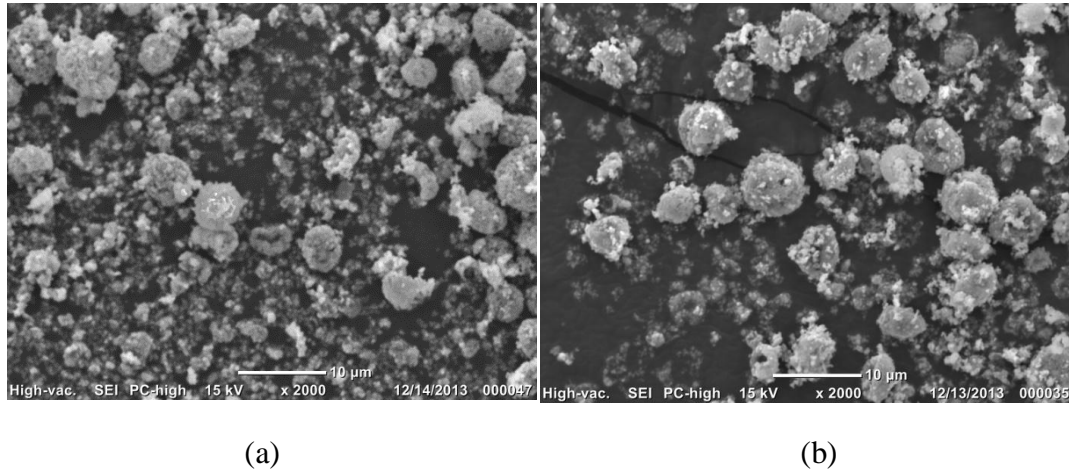
Figure 6.33: SEM micrographs of SD'd: a) 4h HEM'd and b) 32h HEM'd Cr_2O_3 samples.

(a)   (b)
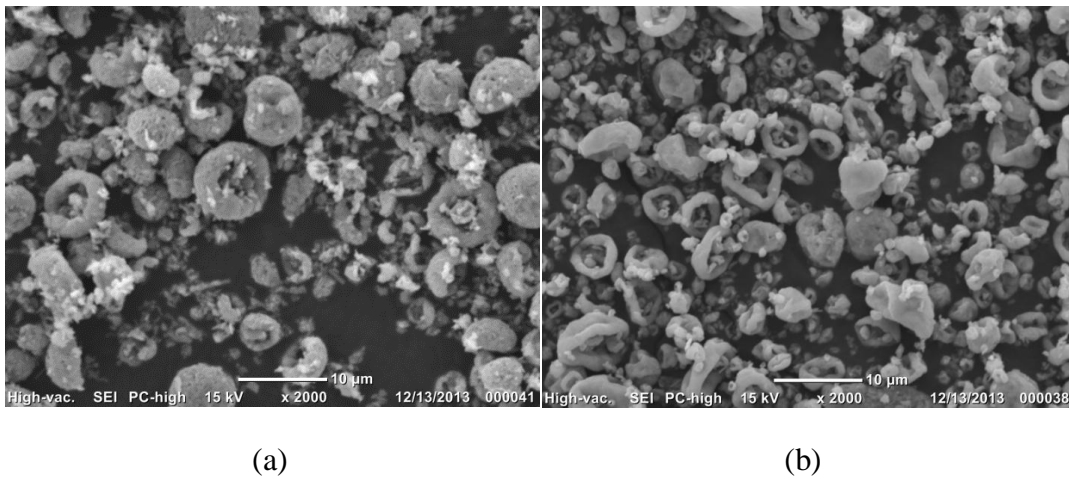
Figure 6.34: SEM micrographs of SD'd: a) 4h HEM'd and b) 32h HEM'd MoO_3 samples.

6.3 Characterization of Sintered Samples

6.3.1 Macrostructural characterizations

Sintered WO_3 samples are shown in Figure 6.35. Several cracks occurred during sintering in the samples which have been just HEM'd. With increasing milling time, the cracks and roughness seem to be reduced. The sample number 2, which was HEM'd for 1 hour, disintegrated completely. SD'd samples showed better compactability. The macrostructure of the WO_3 samples were analyzed by stereomicroscope and are shown in Figure 6.36. The description of the experimental codes of sintered WO_3 samples are given in Table 6.14.

62
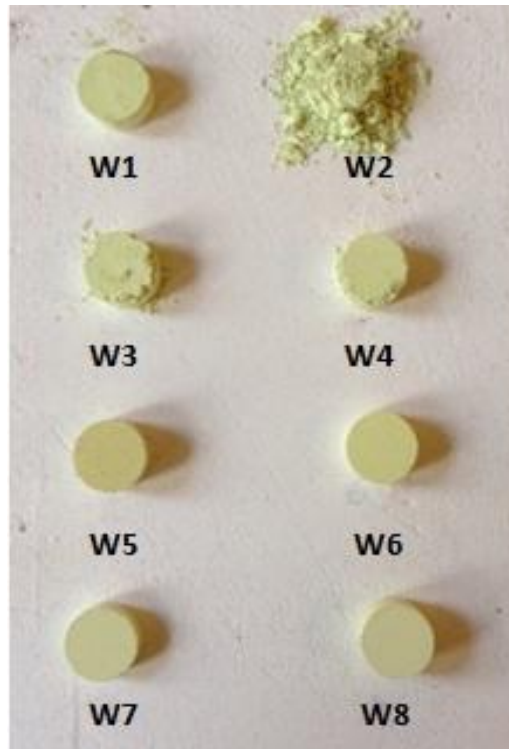
Figure 6.35: WO$_3$ samples sintered at 750 °C.

Table 6.14: Description of the experimental codes of sintered WO$_3$ samples.

Sample Number	Sample Name
W1	Initial
W2	1h HEM'd
W3	4h HEM'd
W4	16h HEM'd
W5	32h HEM'd
W6	SD'd- initial
W7	SD'd-4h HEM'd
W8	SD'd-32h HEM'd

Figure 6.37 reveals the differences between sintered initial and SD'd initial WO$_3$. The WO$_3$ sample, which just pressed and sintered at 750 °C, has several cracks and it is almost impossible to hold the sample. On the other hand the SD'd WO$_3$ sample has much better surface characteristics without any crack. Figure 6.38 also shows the same result as Figure 6.37 samples. In the Figure 6.39a and b, 32h HEM'd WO$_3$ with

and without SD were given. It is apparent from the figures that both samples have some cracks on their outer surfaces.

(a)

(b)

(c)

(d)

(e)

(f)

(g)

(h)

Figure 6.36: Macrostructures of sintered WO_3 samples: a) W1, b) W2, c) W3, d) W4, e) W5, f) W6, g) W7, and h) W8.

(a)   (b)

Figure 6.37: Sintered pellets of: a) W1 and b) W6 samples.
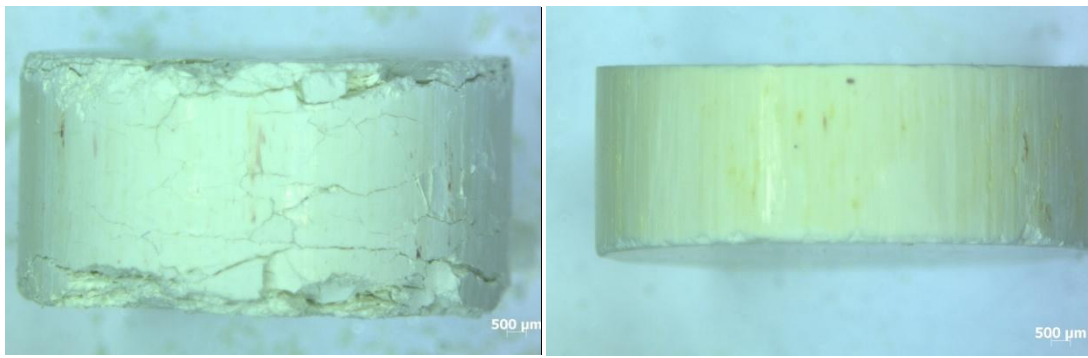
(a)   (b)

Figure 6.38: Sintered pellets of: a) W3 and b) W7 samples.

(a)   (b)

Figure 6.39: Sintered pellets of: a) W5 and b) W8 samples.

Figure 6.40 shows the MoO$_3$ samples sintered at 400 °C. The description of the experimental codes of sintered MoO$_3$ samples are given in Table 6.15.
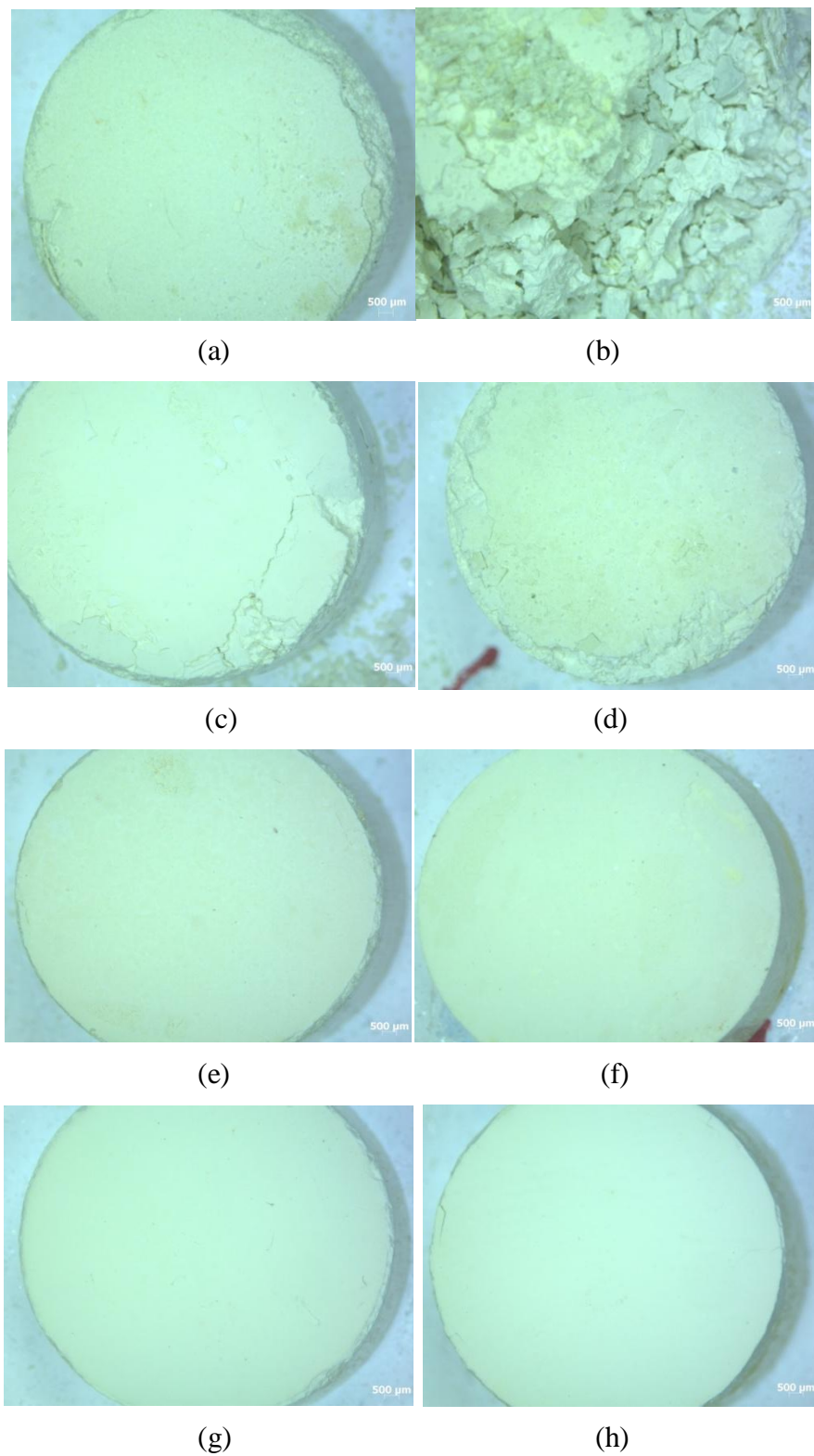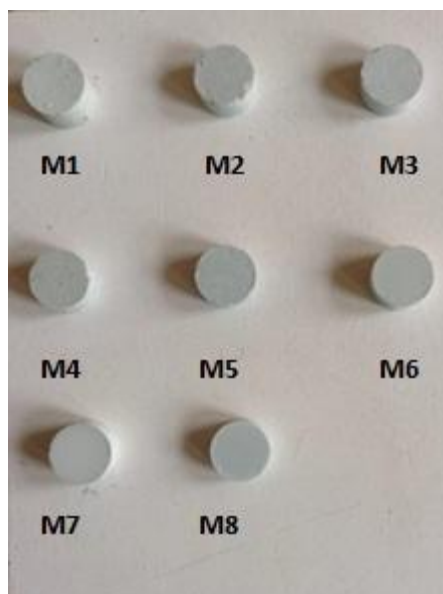

Figure 6.40: MoO$_3$ samples sintered at 400 °C.

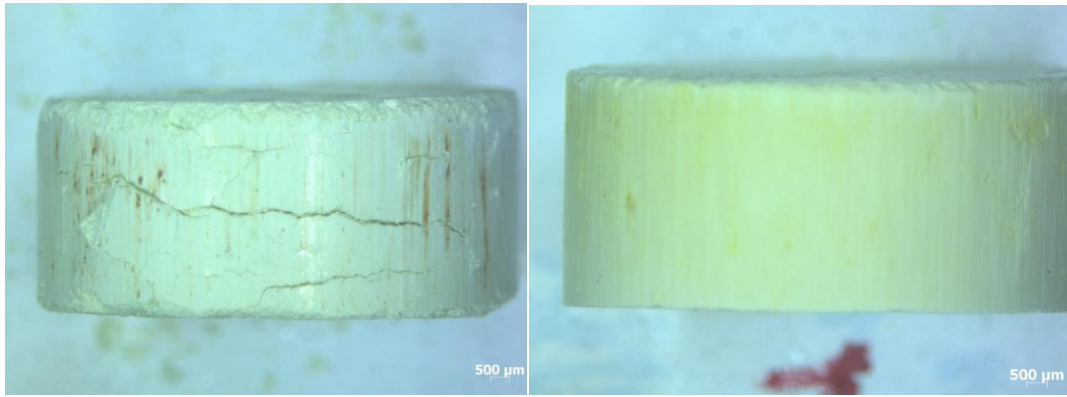**Table 6.15:** Description of the experimental codes of sintered MoO$_3$ samples.

Sample Number	Sample Name
M1	Initial
M2	1h HEM'd
M3	4h HEM'd
M4	16h HEM'd
M5	32h HEM'd
M6	SD'd-initial
M7	SD'd-4h HEM'd
M8	SD'd-32h HEM'd

The macrostructure of the MoO$_3$ samples are shown in Figure 6.41. As shown in the Figure 6.41, with increasing the HEM time, the roughness on the surface of samples decreases. In the Figure 6.42a, the sintered initial MoO$_3$ has many cracks and it almost disintegrates. However, the SD'd one (6.42b) shows better surface properties and smoother than the un-spray dried one. 6.43a and b, reveals the differences between sintered 4h HEM'd MoO$_3$ sample and SD'd 4h HEM'd MoO$_3$ sample. It seems with spray drying, the flow ability of granules made the compacted sample's surface with less cracks.
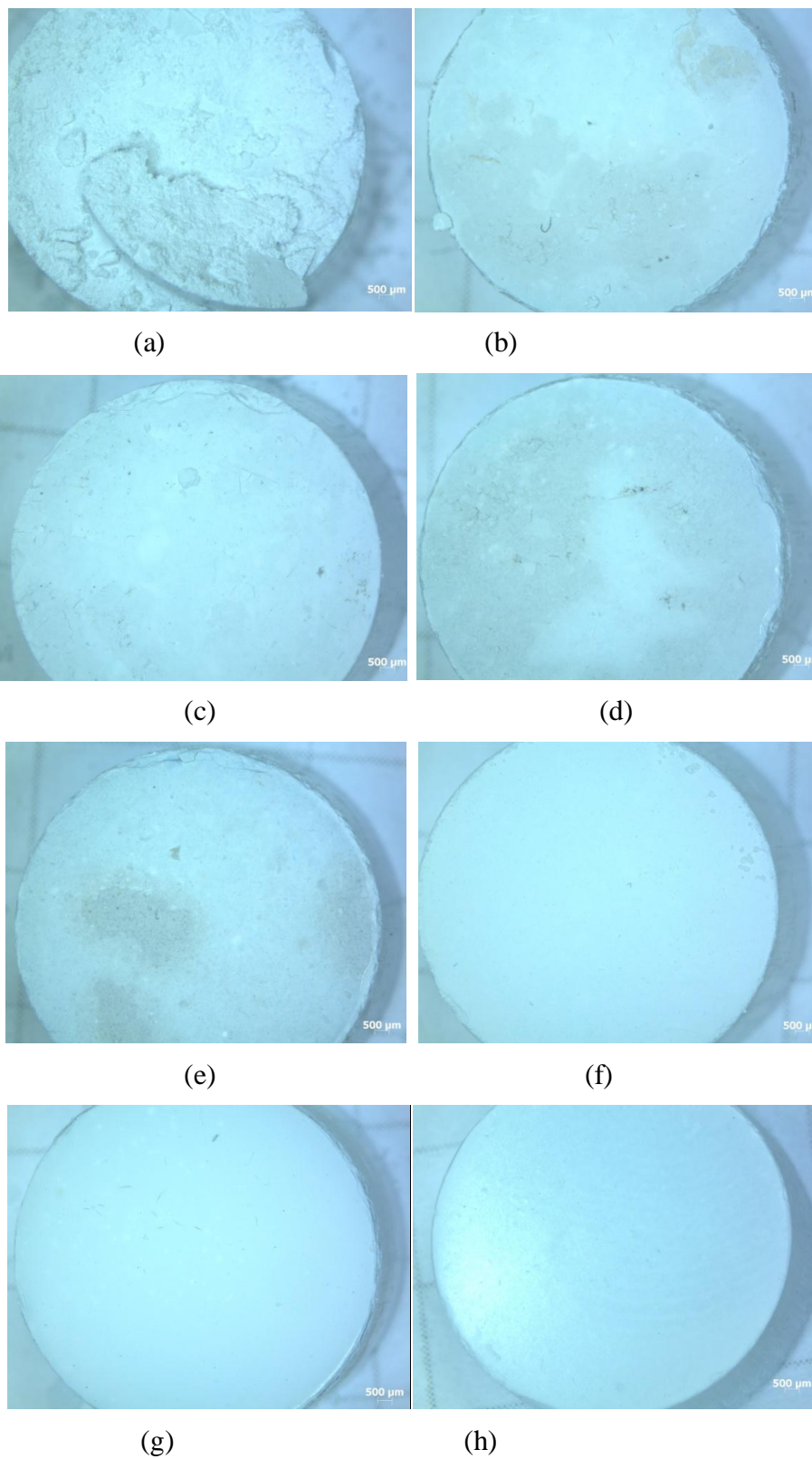
Figure 6.41: Macrostructures of sintered MoO_3 samples: a) M1, b) M2, c) M3, d) M4, e) M5, f) M6, g) M7, and h) M8.
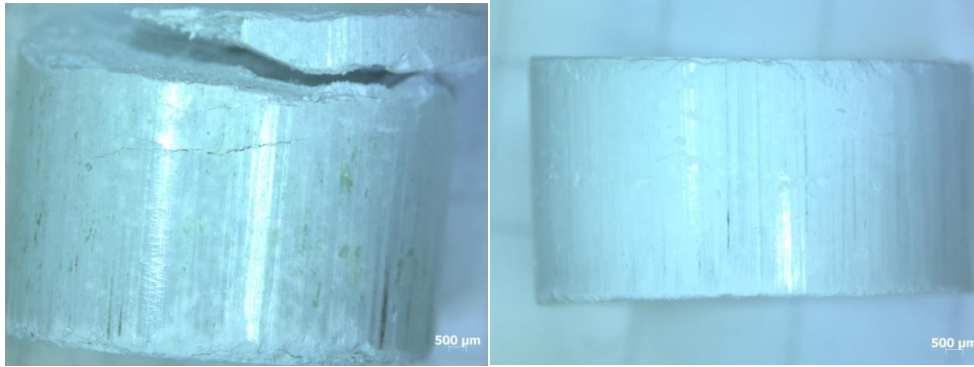
(a)   (b)

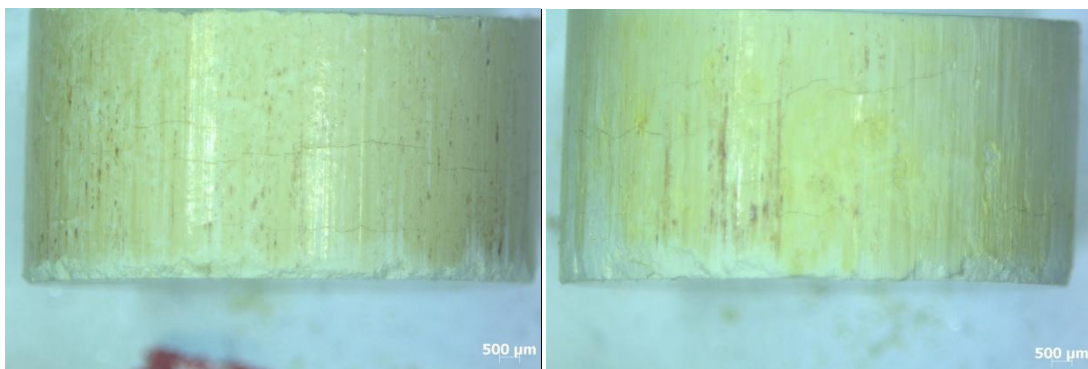**Figure 6.42:** Sintered pellets of: a) M1 and b) M6 samples.
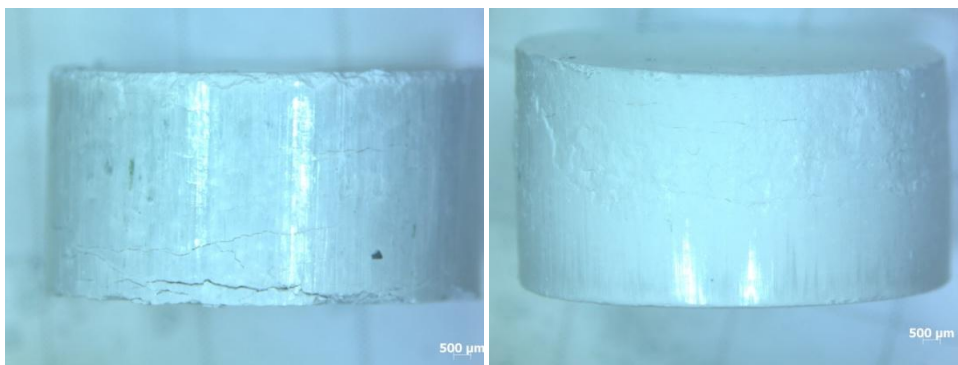
(a)   (b)

Figure 6.43: Sintered pellets of: a) M3 and b) M7 samples.
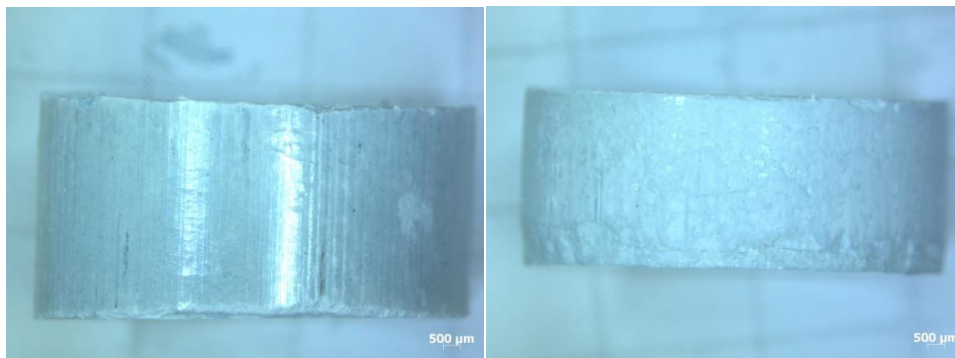
(a)   (b)

Figure 6.44: Sintered pellets of: a) M5 and b) M8 samples.

Figure 6.45 shows the Cr_2O_3 samples sintered at 1200 °C. The description of the experimental codes of sintered Cr_2O_3 samples are given in Table 6.16.
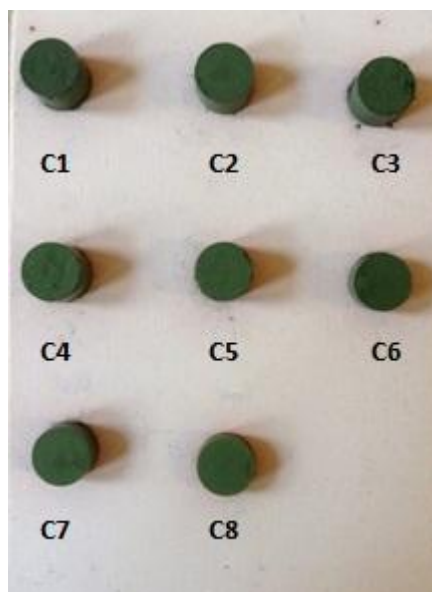
Figure 6.45: Cr_2O_3 samples sintered at 1200 °C.

Table 6.16: Description of the experimental codes of sintered Cr_2O_3 samples.

Sample Number	Sample Name
C1	Initial
C2	1h HEM'd
C3	4h HEM'd
C4	16h HEM'd
C5	32h HEM'd
C6	SD'd -initial
C7	SD'd- 4h HEM'd
C8	SD'd- 32h HEM'd

Figure 6.46 shows the macrostructures of Cr_2O_3 samples. It can be illustrated from Figure 6.46 a-e that increasing milling time, helps to produce a pressed sample with better surface characteristics and less cracks.
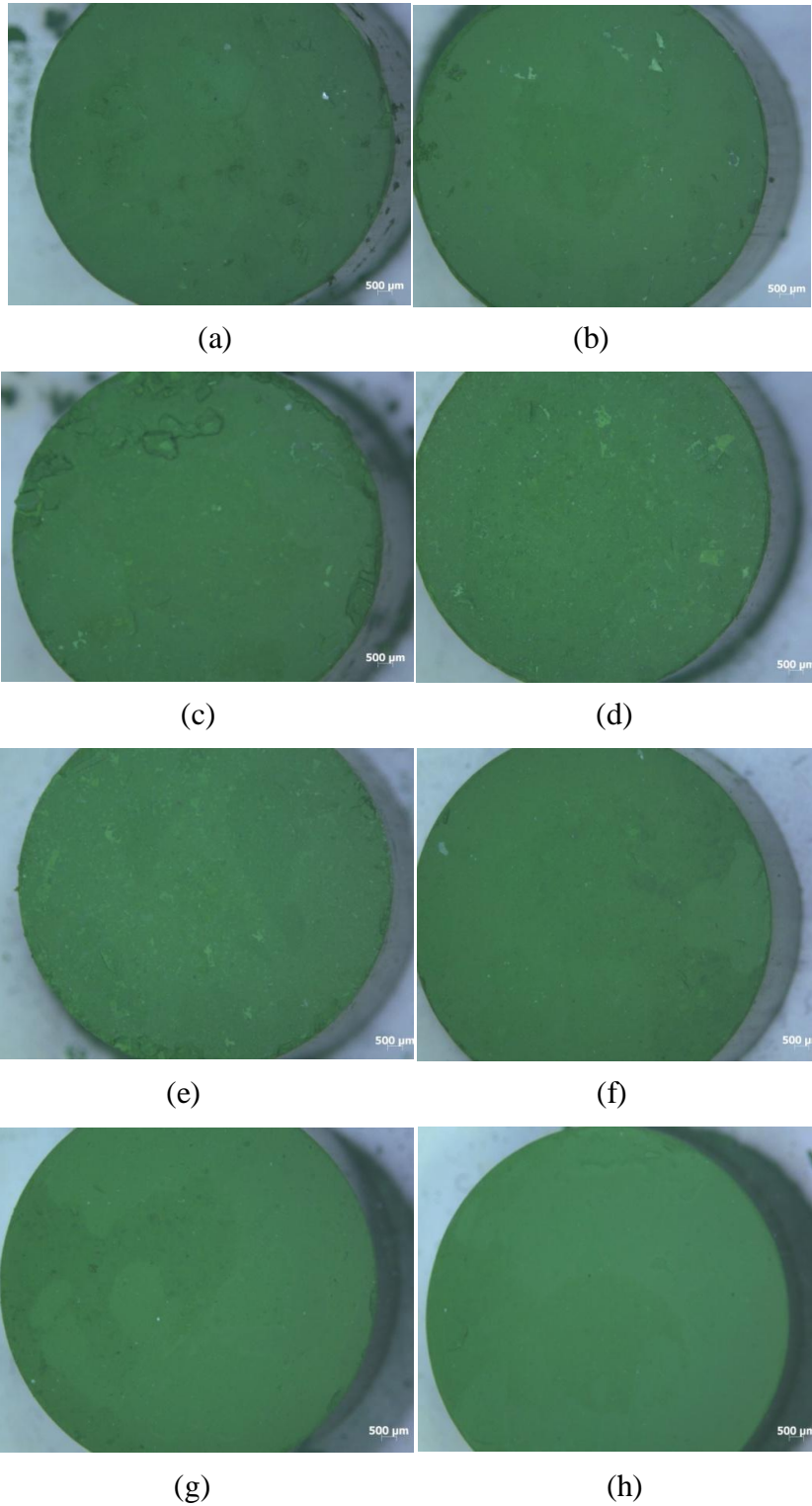
Figure 6.46: Macrostructures of sintered Cr_2O_3 samples: a) C1, b) C2, c) C3, d) C4, e) C5, f) C6, g) C7, and h) C8.

Figure 6.47, 6.48 and 6.49 show the difference between samples with and without spray drying process. It can be seen from the figures that samples, which are processed with spray drying, have better surface characteristics than HEM'd ones.
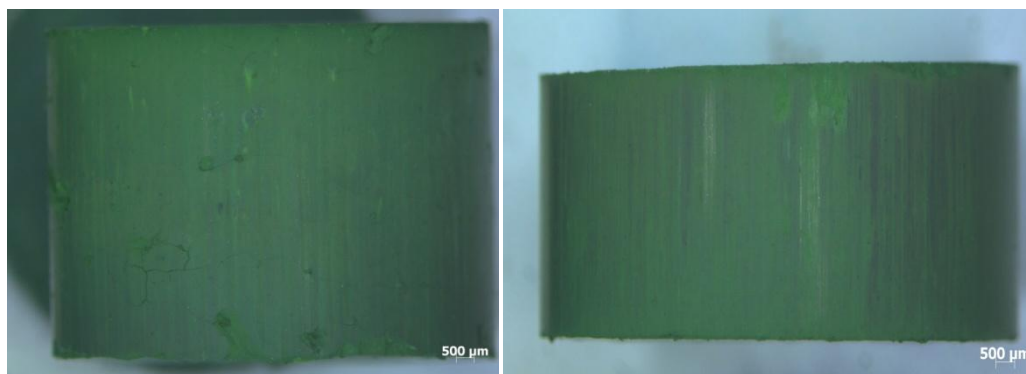
(a)	(b)

Figure 6.47: Sintered pellets of: a) C1 and b) C6 samples.
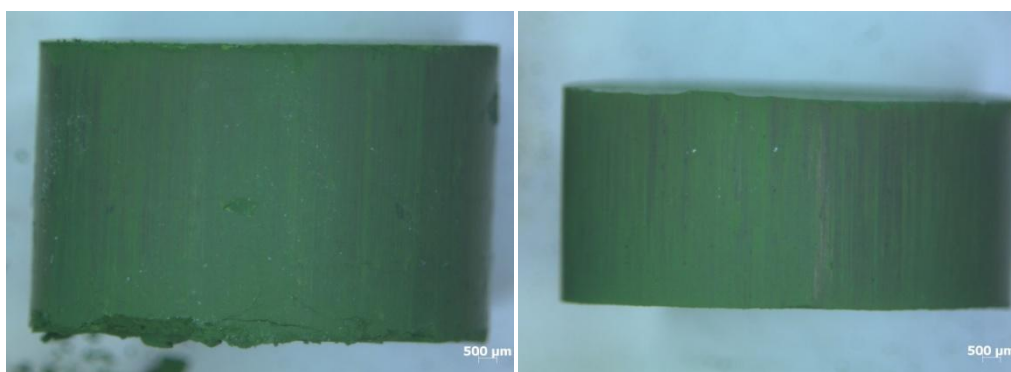
(a)	(b)

Figure 6.48: Sintered pellets of: a) C3 and b) C7 samples.
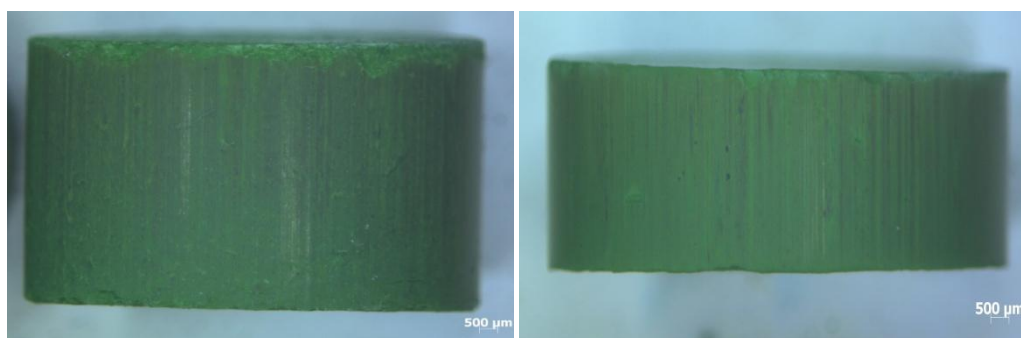
(a)	(b)

Figure 6.49: Sintered pellets of: a) C5 and b) C8 samples.

6.3.2 Phase analysis

XRD pattern of sintered 32h HEM'd WO_3 sample is given in Figure 6.50. As seen in this figure, only the peaks of WO_3, which has a monoclinic Bravais lattice with the lattice parameters of a=7.301 nm, b=5.389 nm, and c=7.689 nm (PDF No:01-083-0950) can be identified, i.e. no new phase formation took place during sintering of the monoclinic WO_3.
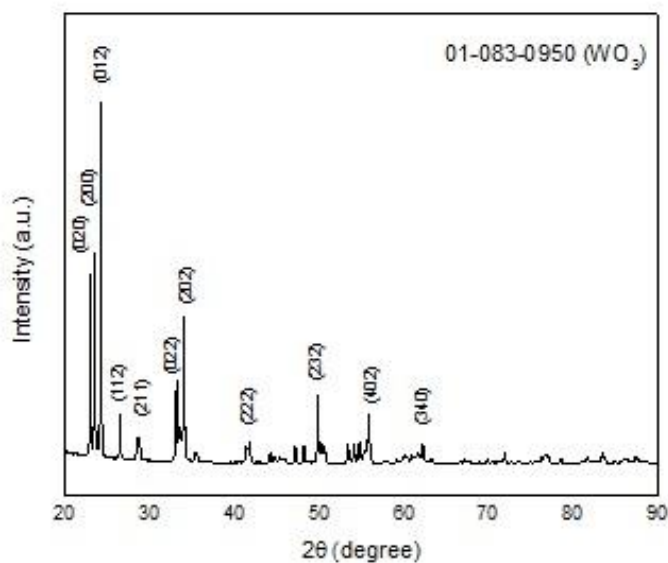
Figure 6.50: XRD pattern of the sintered WO_3 sample HEM'd for 32h.

XRD pattern of the sintered Cr_2O_3 sample that was HEM'd for 32h is shown in Figure 6.51. The peaks of Cr_2O_3, which has a rhombohedral Bravais lattice with the lattice parameters of a=4.953 nm and c=13.578 nm (PDF No: 01-072-3533) can be identified. Additionally, the presence of the ZrO_2 phase which has a tetragonal Bravais lattice with the lattice parameters of a=3.598 nm and c=5.185 nm (PDF No: 01-072-7115) detected due to contamination during HEM.
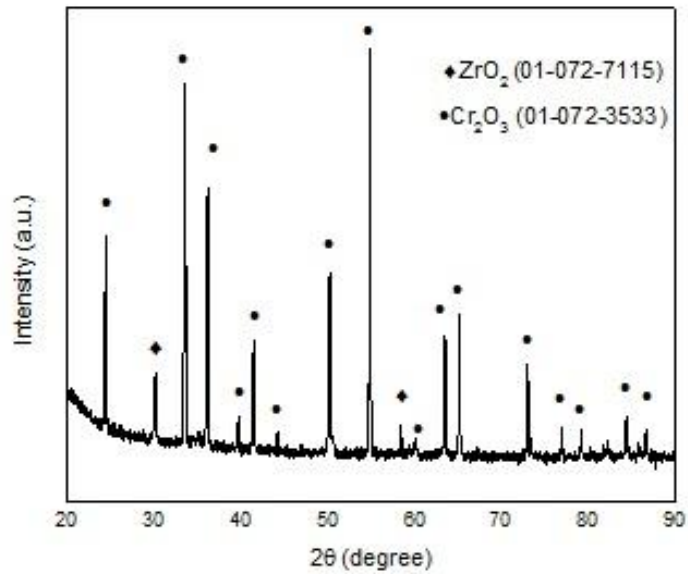
Figure 6.51: XRD pattern of the sintered Cr_2O_3 sample HEM'd for 32h.

Figure 6.52 shows the XRD pattern of the MoO_3 sample that was HEM'd for 32h. As seen in the figure, the peaks of MoO_3 which has an orthorhombic Bravais lattice with the lattice parameters of a=3.963 nm, b=13.855 nm, and c=3.696 nm (PDF No: 01-076-1003) can be identified, indicating that any phases other than orthorhombic MoO_3 did not occur during sintering.
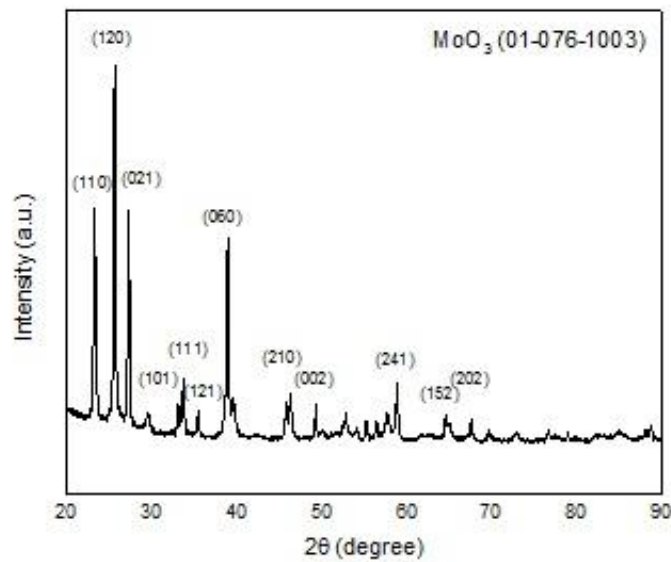
Figure 6.52: XRD pattern of the sintered MoO_3 sample HEM'd for 32h.

6.3.3 Density measurements

The green density and sintered density values of sintered WO_3 samples are given in Table 6.17. The sintered density of initial, 1h and 4h HEM'd WO_3 samples could not be measured because of the cracks and disintegrations. A decreasing tendency in the green density of both SD'd and un-SD'd samples were observed with increasing milling times. Sintered density values of SD'd samples are more than HEM'd ones and varies between 91.5 and 96.7 % based on HEM duration.

Table 6.17: Relative green and sintered density values of the WO_3 sintered samples.

Sample Name	% Green Density (g/cm^3)	% Sintered Density (g/cm^3)
Initial	77.6	_
1h HEM'd	75.5	_
4h HEM'd	71.5	_
16h HEM'd	70.3	95.2
32h HEM'd	67.8	95.7
SD'd-initial	77.2	91.5
SD'd-4h HEM'd	73.2	93.5
SD'd-32h HEM'd	66.6	96.7

Figure 6.53 shows the green density and sintered density comparative plots between SD'd and un-SD'd WO_3 samples. It can be illustrated that SD'd samples have more sintered density than HEM'd ones.

The green density and sintered density values of the sintered Cr_2O_3 samples are given in Table 6.18. Green density values of Cr_2O_3 samples vary between 53.4 and 66.1 %. However, there is no correlation between the green density values. The minimum value corresponds to the SD'd initial Cr_2O_3 and the maximum one to the SD'd 32h HEM'd Cr_2O_3. Sintered density of SD'd Cr_2O_3 values vary between 91 and 92.7 %. It remains approximately constant inferring that the sintered density of SD'd samples was independent from HEM duration. Maximum value of sintered density occurred in un-SD'd 32h HEM'd Cr_2O_3 with a value of 98.6 %. Figure 6.54 shows the comparative plots between relative densities of SD'd and un-SD'd Cr_2O_3 samples.
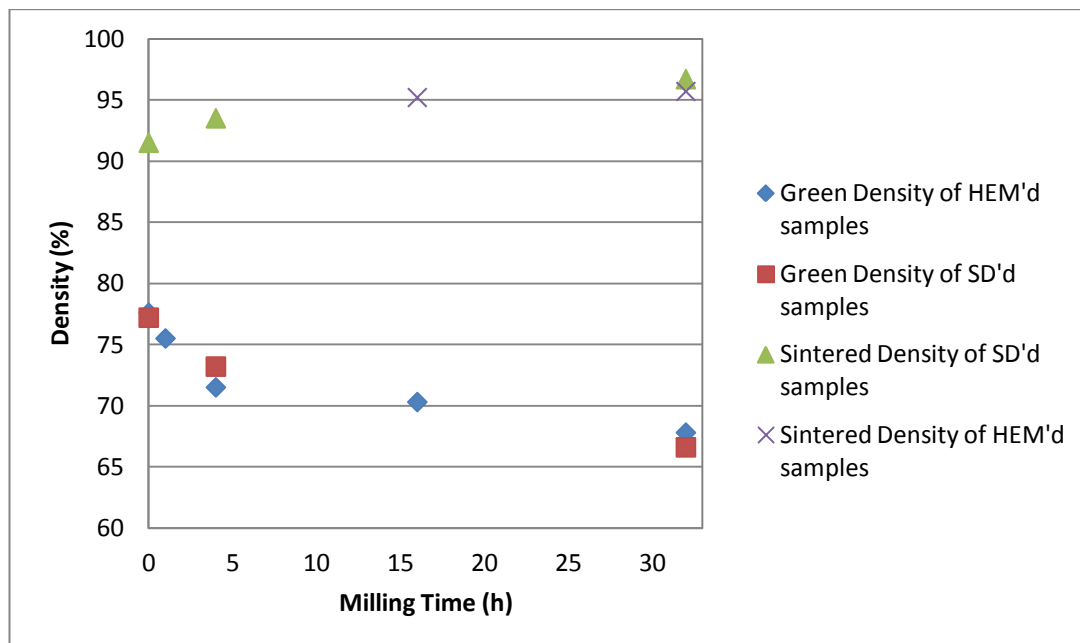
Figure 6.53: Green density and sintered density values of HEM'd and SD'd WO$_3$ samples at different milling times.

Table 6.18: Relative green and sintered density values of the Cr$_2$O$_3$ sintered samples.

Sample Name	% Green Density (g/cm^3)	% Sintered Density (g/cm^3)
Initial	63.6	95.1
1h HEM'd	62.7	93.9
4h HEM'd	62.3	96.8
16h HEM'd	64.7	94.5
32h HEM'd	64.4	98.6
SD'd-initial	53.4	92.7
SD'd-4h HEM'd	64.4	91.4
SD'd-32h HEM'd	66.1	91.0

Green density values of MoO$_3$ samples are given in Table 6.19. The green density values of MoO$_3$ samples vary between 62.7 and 69.1 %. As seen in the Figure 6.55, green density values of SD'd samples remains approximately constant, indicating that the HEM duration did not cause sharp changes in green density of SD'd MoO$_3$ samples. Sintered density of initial MoO$_3$ could not be measured due to disintegration of the sample. Sintered density values vary between 72.1 and 91.5 %.

SD'd samples have low sintered density values compared to HIM'd ones. There is a decreasing tendency in the sintered densities as HIM duration increases.

Figure 6.54: Green density and sintered density values of HEM'd and SD'd Cr_2O_3 samples with different milling times.

Table 6.19: Relative green and sintered density values of the MoO_3 sintered samples.

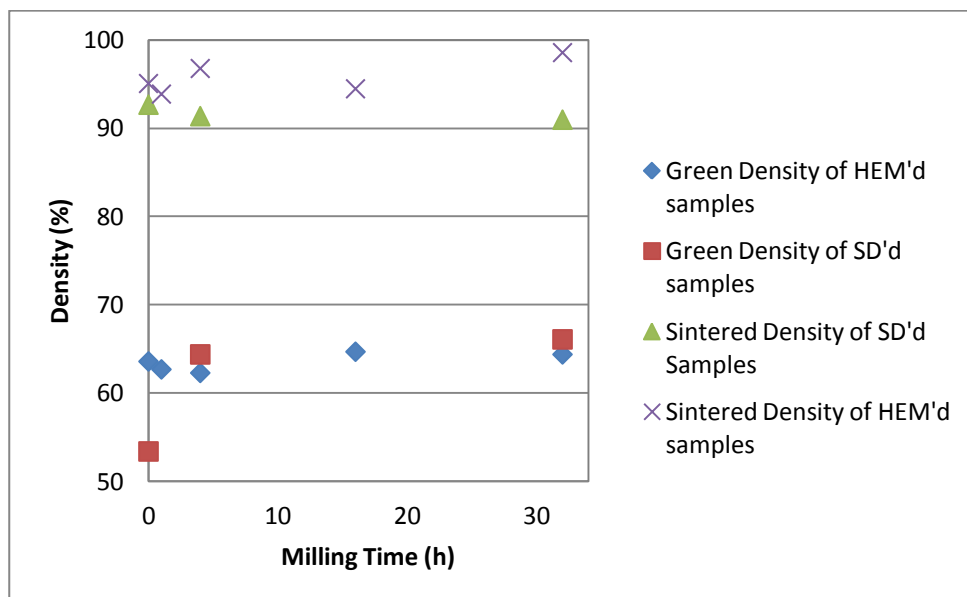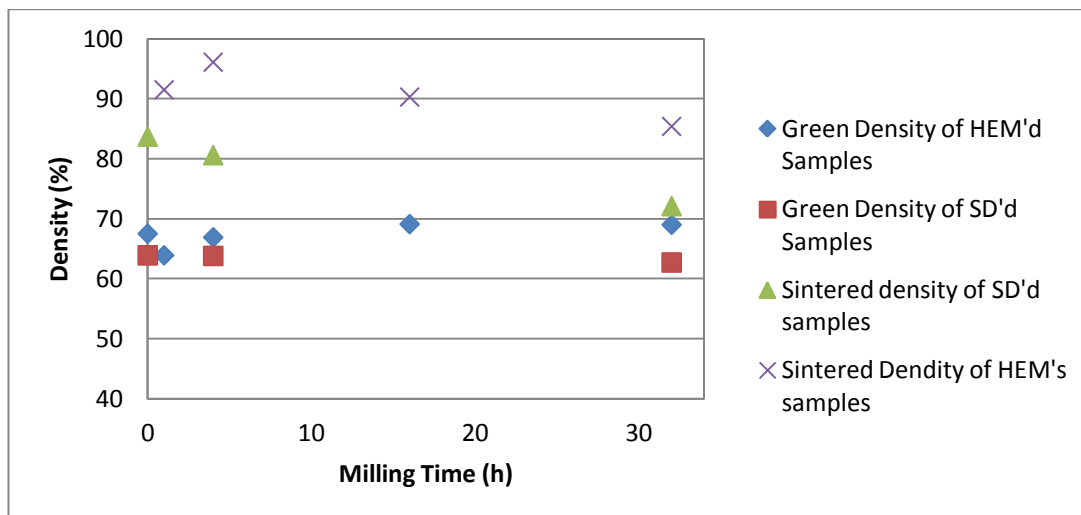| Sample Name	% Green Density (g/cm^3)	% Sintered Density (g/cm^3)
Initial	67.5	–
1h HEM'd	63.9	91.5
4h HEM'd	66.9	96.1
16h HEM'd	69.1	90.3
32h HEM'd	69.0	85.4
SD'd-initial	63.9	83.7
SD'd-4h HEM'd	63.8	80.6
SD'd-32h HEM'd	62.7	72.1

Figure 6.55: Green density and sintered density values of HEM'd and SD'd MoO$_3$ samples at different milling times.

CONCLUSIONS

On the basis of the results of the present investigations, the following conclusions can be drawn:

1. During HEM, certain decrease for the mean particle sizes of initial MoO_3, WO_3 and Cr_2O_3 powders were observed. Although over micron-sized initial powders were selected as starting materials, particle size distributions varying between 100 and 200 nm were measured for each system after 32h milling. With addition of Darvan C to the Cr_2O_3 during HEM, the mean particle sizes of samples were decreased compared to the samples which were without Darvan C. For the rest of two systems, any sharp changes in the particle size distributions were not observed. It should be noted that in the Cr_2O_3 system, with increasing milling time up to 32 hours, the contamination of milling media (ZrO_2) was observed.

2. Although the experimental parameters for all three systems were chosen as same during spray drying process, each system led to different morphology compared to the others. After SD of WO_3, dense spherical granules were formed in the size ranges of 1 and 10 µm based on HEM duration. While hollow shapes varying in size between 1 and 5 µm observed for SD'd MoO_3 particles, doughnut-shaped granules were formed for the Cr_2O_3 system.

3. With increasing milling time, apparent density values were increased for both WO_3 and MoO_3 powders. This indicates that the packing behavior of these powders reduces with further HEM. On the other hand, observed lower apparent densities of SD'd samples compared to HEM'd ones was a related with use of additional PVA used during SD process.

4. In all systems after sintering, the HEM'd samples had several cracks whereas SD'd ones had much better surface characteristics and less cracks. In the case of WO_3 cracks led to total disintegration of initial compact shape therefore their sintered density could not be measured.

5. Sintered density values of SD'd WO_3 samples were increased with increasing the HEM duration. It could be interpreted that with increasing HEM duration, small particle sizes act as a driving force in the sintering process. Sintered density of SD'd MoO_3 had lower values than HEM'd one due to the formation of hollow granules and porous structure. The sintered density behavior of Cr_2O_3 systems couldn't be interpreted due to the contamination in the samples.

6. This study has shown that all SD'd powders, regardless of their morphology, have shown better compactability during die pressing compared to their counterparts of HEM'd powders. On the other hand each system has to be studied in details to achieve desired particle shapes and granulation morphology after SD.

REFERENCES

Asthana, R., Kumar, A., Dahotre, N.B. (2006). Composite Materials in Materials Processing and Manufacturing Science: 397-484.

Asthana, R., Kumar, A., Dahotre, N.B. (2006). Powder Metallurgy and Ceramic Forming in Materials Processing and Manufacturing Science: 167-245.

Balaz, P. (2008). Mechanochemistry in Nanoscience and Mineral Engineering, Springer Berlin, Heidelberg, Germany.

Balaz, P., Godocikova, E., Krilova, L., Lobotka, P., Gock, E. (2004). Preparation of nanocrystalline materials by high-energy milling, *Materials Science and Engineering A 386 (2004) 442–446.*

Baraton, M.I. (2003). Synthesis, Functionalization and Surface Treatment of Nanoparticles, American Scientific Publishers, CA, USA.

Binner, J.G.P. (1990). Advanced Ceramic Processing and Technology, William Andrew Publishing, NY, USA.

Cellard, A., Zenati, R., Garnier, V., Fantozzi, G., Baret, G. (2007). Optimization of chromium oxide nanopowders dispersion for spray-drying, Journal of the European Ceramic Society **27**: 1017–1021.

Cellard, A., Zenati, R., Garnier, V., Fantozzi, G., Baret, G. (2006). Nanopowder dispersion and spray-drying process: the case of Cr_2O_3, International Journal of Materials Research, Volume 97, **5:** 632-638.

Cox, P.A. (1992). Transition Metal Oxides: An Introduction to their Electronic Structure and Properties, Oxford Science Publications, UK.

El-Eskandarany, M.S. (2001). Mechanical Alloying for Fabrication of Advanced Engineering Materials. Noyes Publications / William Andrew Publishing, Norwich, New York, USA.

Fang, Z.Z. (2010). Sintering of Advanced Materials - Fundamentals and Processes, Woodhead Publishing, Oxford, UK.

Fecht, H.J. (2002). Nanostructured materials and composite prepared by solid state processing, in *Nanostructured Materials: Processing, Properties and Potential Applications*, Ed. Koch, C.C., Noyes Publications, New York, USA.

Gilman, P.S., Benjamin, J.S. (1983). Mechanical Alloying, *Annual Review of Materials Science*, **13:** 279-300.

Goff, A. (2003). Modeling and synthesis of a piezoelectric ceramic-reinforced metal matrix composites. *MS Thesis,* Virginia Polytechnic Institue and State University, Blacksburg, VA, USA.

Ivanova, T., Gesheva, K.A., Kozlov, M., Abrashev, M. (2011). Electrochromic and optical study of atmospheric pressure chemical vapour deposition MoO_3-Cr_2O_3 films, *J Nanosci Nanotechnol, 11(9):8017-23.*

Kang, S.J.L., (2005). Sintering: Densification, Grain Growth and Microstructure, Elsevier, Oxford, UK.

Kim, D.J., Jung, J.Y. (2007). Granule performance of zirconia/alumina composite powders spray-dried using polyvinyl pyrrolidone binder. Journal of the European Ceramic Society **27**: 3177–3182.

Lassner, E. and Schubert, W.D. (1999). Tungsten: Properties, Chemistry, Technology of the Element, Alloys and Chemical Compounds, Klower Academic, New York, USA.

Lindroos, V.K., Hellman, J.T., Lou, D., Nowak, R., Pagounis, E., Liu, X.W., and Penttinen, I.M. (2004). Designing with Metal-Matrix Composites, in Handbook of Mechanical Alloy Design, Eds. Totten, G. E., Xie, L., Funatani, K., Marcel Dekker, Inc., New York, USA.

Liu, J., Huang, T., Zhang, H., Wang, R. (2012). Prepare uniformity superfine WO_3 by Spray drying, *Advanced Materials Research, Vols. 399-401, pp 731-735.*

Liu, Y.B., Lim, S.C., Lu, L. and Lai, M.O. (1994). Recent development in the fabrication of metal matrix particulate composites using powder metallurgy techniques. *Journal of Materials Science*, **29:** 1999-2007.

Liu, Z., Bando, Y., Tang, C. (2003). Synthesis of tungsten oxide nanowires. *Chemical physics letters. Volume 372, Issues 1–2, Pages 179–182.*

Lukasiewicz, S.J. (1991) Granulation and spray drying, in Engineered Material Handbook, *vol. 4, Ceramics and glasses (ed. S.J. Schneider), ASM International, Pages 100–108, USA.*

Lyo, I.W., Ahn, H.S., Lim, D.S. (2003). Microstructure and tribological properties of plasma-sprayed chromium oxide-molybdenum oxide composite coatings, Surface and Coatings Technology, 163–164, 413–421.

Maldonado, F., Novillo, C., Stashans, A. (2012). *Ab initio* calculation of chromium oxide containing Ti dopant, Volume 393, Issue 1, Pages 148–152.

Masters, K. (1994). Applying spray drying to ceramics, Am. Ceram. Soc. Bull., **73** (1), 63–72.

Masters, K. (1999). Spray Drying Handbook, Longman Scientific Technical, UK.

Mestl, G., Herzog, B., Schlogl, R., Knozinger, H. (1995). Mechanically Activated MoO_3. 1. Particle Size, Crystallinity, and Morphology, *Langmuir*, **11:** 3027-3034.

Mestl, G., Verbruggen, N.F.D., Bosch, E., Knozinger, H. (1996). Mechanically Activated MoO_3. 5. Redox Behavior, *Langmuir,* **12:** 2961-2968.

Mestl, G., Verbruggen, N.F.D., Knozinger, H. (1995). Mechanically Activated MoO_3. 2. Characterization of Defect Structures, *Langmuir,* **11:** 3035-3041.

Newkirk. J. W., and Kohser, R. A. (2004). Designing With Powder Metallurgy Alloys, in Handbook of Mechanical Alloy Design, Eds. Totten, G. E., Xie, L, Funatani K., Marcel Dekker, Inc., New York, USA.

Okuyama, K., Lenggoro, I.W. (2003). Preparation of nanoparticles via spray route, *Chemical Engineering Science*, **58:** 537-547.

Ortiz, M., Herrera, T. (2012). Molybdenum: Characteristics, Production and Applications, Nova Science Publishers, Inc., New York, USA.

Öveçoglu, M.L. (1987). Development of a dispersion-strengthened Al-Fe-Ce alloy by mechanical alloying and related theoretical modeling of dislocations in composite materials. *PhD Thesis*, Stanford University, Stanford, CA, USA.

Pang, X., Gao, K., Volinsky, A.A. (2007). Microstructure and mechanical properties of chromium oxide coatings. *Materials Research Society. J. Mater. Res., Vol. 22, No. 12.*

Peighambardoust, S.H., Tafti, A.G., Hesari, J. (2011). Application of spray drying for preservation of lactic acid starter cultures: a review. *Trends in Food Science & Technology,* **22:** 215-224.

Raab, Ch., Simko, M., Fiedeler, U., Nentwich, M., Gazso, A. (2011). Production of nanoparticles and nanomaterials. *Institute of Technology Assessment of the Austrian Academy of Sciences. Nano trust dossiers. No. 006en, Australia.*

Rak, Z. S. (2000). Advanced Forming Techniques in Ceramics, ECN-RX-00-003, pp. 2-18.

Ramana, C.V., Atuchin, V.V., Kesler, V.G., Kochubey, V.A., Pokrovsky, L.D., Shuthannandan, V., Becker, U., Ewing, R.C. (2007). Growth and surface characterization of sputter-deposited molybdenum oxide thin films. *Applied surface science. Volume 253, Issue 12, Pages 5368–5374.*

Rao, C.N.R and Raveau, B. (1998). Transition Metal Oxides: Structure, Properties, and Synthesis of Ceramic Oxides, WILEY-VCH, Canada.

Rao, M.C., Ravindranadh, K., Kasturi, A., Shekhawat, M.S. (2013). Structural Stoichiometry and Phase Transitions of MoO_3 Thin Films for Solid State Microbatteries, *Research Journal of Recent Sciences, Vol. 2(4), 67-73.*

Reeds, J.S. (1997). Spray drying and implications for compactibility of product granules. *Ceramic Engineering and Science Proceedings*, **18**: 343-358.

Reeds, J.S., Walker Jr, W.J., Verma, S.K. (1999). Influence of Slurry Parameters on the Characteristics of Spray-Dried Granules. *J. Am. Ceram. Soc.,* **82** [7] 1711–19.

Riedel, R., and Chen, I. (2012). Ceramics Science and Technology: Volume3: Synthesis and Processing, Wiley-VCH Verlag GmbH & Co. KGaA, Germany.

Rundgren, K., Lyckfeldt, O. and Sjostedt, M. (2003). Improving Powders with Freeze Granulation, *Ceramic Industry, pp 40-44.*

Ryu, H.J., Hong, S.H. and Baek, W.H. (2000). Microstructure and mechanical properties of mechanically alloyed and solid-state sintered tungsten heavy alloys, *Materials Science and Engineering* A, **291**: 91-96.

Suryanarayana, C. (2001). Mechanical alloying and milling, *Progress in Materials Science,* **46,** 1-184.

Suryanarayana, C., Ivanov, E. and Boldyrev, V.V. (2001). The science and technology of mechanical alloying, *Materials Science and Engineering* A**, 304-306:** 151-158.

Udy, M.J. (1956). Chromium. Reinhold. New York, USA.

Upadhyaya, G. S. (2001). Some issues in sintering science and technology. Materials Chemistry and Physics, **67:** 1-5.

Url-1 *<http://www.news-medical.net/health/Properties-of-Nanoparticles.aspx>*, Date retrieved 07.09.2013.

Url-2 *<http://www.news-medical.net/health/Synthesis-of-Nanoparticles.aspx>,* Date retrieved 01.09.2013.

Vincenzini, P. (1991). Fundamentals of Ceramic Engineering, Elsevier Science Publishing Co., Inc. New York, USA.

Vogt, T., Woodward, P.M., Hunter, B.A. (1999). The high-temperature phases of WO_3. J Solid State Chem, **144**:209–15.

Walia, S., Balendhran, S., Nili, H., Zhuiykov, S., Rosengarten, G., Wang, Q.H., Bhaskaran, M., Sriram, S., Strano, M.S., Kalantarzadeh, K. (2013). Transition metal oxides - Thermoelectric properties, Progress in Materials Science **58**:1443–1489.

Walker, J., and Reed, J.S. (1999). Influence of slurry parameters on the characteristics of spray dried granules. J. Am.Ceram. Soc., **82**: 1711–1719.

Zheng, H., Zhen O. J., Strano, S. M., Kaner, R. B., Mitchell, A., Kalantarzadeh, K. (2011). Nanostructured Tungsten Oxide – Properties, Synthesis, and Applications, *Adv. Funct. Mater., 21:*2175–2196.

Zhou, J., Ding, Y., Deng, S.Z., Gong, L., Xu, N.S., Wang, Z.L. (2005). Three-dimensional tungsten oxide nanowire networks. Adv. Mater. **17:** 2107-2110.

CURRICULUM VITAE

Name Surname: Leila Haghighi Poudeh

Place and Date of Birth: Tehran, 02.01.1988

Address: Istanbul, Turkey

E-Mail: leilahaghighi@itu.edu.tr

B.Sc.: University of Tabriz, Ceramics Engineering